

EASI-STRESS

EUROPEAN ACTIVITY FOR STANDARDIZATION OF INDUSTRIAL RESIDUAL STRESS CHARACTERIZATION

H2020 NMBP-35-2020

Grant Agreement Number: 953219



Deliverable Report:

D2.3 Round-robin results

Project Deliverable Information Sheet

EASI-STRESS Project	Project Ref. No. 953219	
	Project Title: EASI-STRESS - European Activity for Standardization of Industrial residual STRESS characterization	
	Project Website: www.easi-stress.eu	
	Deliverable No.: D2.3	
	Deliverable Type: Report	
	Dissemination Level: Public	Contractual Delivery Date: 31/12/2022
		Actual Delivery Date:
	EC Project Officer: Yanaris Ortega Garcia	

Document Control Sheet

Document	Title: Round-robin results	
	Version: 1.0	
	Available at:	
	Files:	
Authorship	Written by	Matthew Roy
	Contributors	David Canelo Yubero Sandra Cabeza Thilo Pirling Arnold Paecklar Peter Staron Romain Badyka Simon Robbe Hanna Leemreize Wen Cui Philipp Mayr Manuel Sanchez Poncela Romain Badyka Ranggi Sahmura Ramadhan Mohamed Fares Slim
	Reviewed by	Phil Withers
	Approved	

List of Abbreviations

AM – Additive manufactured
CM – Contour Method
CMM – Coordinate Measurement Machine
CSC – Conical Slit Cell
ESPI – Electronic speckle pattern interferometry
FEA – Finite element analysis
HD – Hole drilling
ICP – Iterative closest point
LRI – Large-scale Research Infrastructure
LXRD – Laboratory X-ray Diffraction
ND – Neutron Diffraction
RS – Residual stress
SGV – Sampled gauge volume
SXRD – Synchrotron high energy X-ray Diffraction
SVD – Single value decomposition
VM – Von Mises



Table of Contents

Project Deliverable Information Sheet	2
Document Control Sheet	2
List of Abbreviations	3
Table of Contents.....	4
Executive Summary.....	5
Report on Implementation Process and Status of Deliverable.....	5
1. Introduction	5
2. Background	6
2.1 Components considered.....	6
2.2 Techniques applied.....	7
2.3 Error estimation for techniques considered.....	8
2.4 Summary.....	10
3. Inter-technique reporting procedure	10
4. Results	12
4.1 Ferritic steel U-forms	12
4.2 Powder-derived stainless steel additively manufactured arches.....	20
4.3 Inconel GTAW three pass welded plates	32
4.4 Cast and quenched aluminium wedges.....	32
5. Summary and conclusions	40
6. References	41
Appendices	43
Appendix 1 – Application of neutron diffraction to ferritic steel U-forms	44
Appendix 2 – Application of synchrotron diffraction to ferritic steel U-shapes.....	46
Appendix 3 – Application of contour method to U-bend ferritic shapes and preparation for LXRD ...	47
Appendix 4 – Application of contour method to U-bend ferritic shapes	49
Appendix 5 – Application of LXRD to cut U-bend ferritic shapes	52
Appendix 6 – Application of neutron diffraction to austenitic steel AM Arches.....	54
Appendix 7 – Application of synchrotron diffraction to the powder-derived stainless steel additively manufactured arches	56
Appendix 7 – Comparison of additional results of LRI diffraction techniques on arches.....	59
Appendix 8 – Application of contour method Arcelor Mittal additively manufactured LPBF 316L components	64
Appendix 9 – Application of contour method to LPB-F 316L Arches samples (CETIM).....	66
Appendix 10 – Application of LXRD measurements on LPB-F 316L Arches samples (CETIM)	68
Appendix 11 – Application of contour method to cast and quenched wedges and subsequent hole drilling	72
Appendix 12 – Application of neutron diffraction to the cast, quenched and T6 tempered aluminium wedge	76
Appendix 13 – Application of hole drilling measurements with strain gauges to cast and quenched wedges, L-PBF 316L Arches samples and ferritic U-bend shapes.....	77

Executive Summary

The progress of a round robin residual stress measurement campaign of benchmark components is reported. A brief description of the samples and conditions that they were supplied in is provided, as well as their unique challenges to residual stress determination. The procedures employed to correlate stresses obtained across the diffraction techniques available across the consortium has been described. This includes techniques available through large research infrastructure (LRI) namely neutron and high energy synchrotron X-ray diffraction (ND, SXRD), as well as the laboratory techniques comprising laboratory X-ray diffraction (LXRD), the contour method (CM) and hole drilling (HD). The results of a total of 36 measurement campaigns are reported on over 14 components. These comprise a wide range of industrially relevant metallic systems and residual stress levels. For almost all components, at least two different techniques have been applied to showcase the relative merits of each technique. It will be shown that for most applications, LRI techniques remain the most tractable when best practice are followed, and are strongly complemented by supporting laboratory techniques. The present findings, approaches and results will be employed to support further standardization of residual stress determination techniques.

Report on Implementation Process and Status of Deliverable

1. Introduction

Often the nature of the residual stress to be assessed and the given material system dictate that the most accurate results can be obtained using a single technique. However, there are a multitude of components and material systems such that it is impossible to determine whether a fair assessment residual stress can be found by pursuing one particular type of technique over another.

Round robin exercises have been employed previously for residual stress measurements on individual components, with individual techniques. The approach taken for the EASI-STRESS benchmarking exercise is that of examining a series of components with industrial relevance with increasingly more complex geometries, material systems and residual stress fields to be interrogated. This report details the work to-date conducted on round-robin measurements of the benchmark components considered within EASI-STRESS: ferritic steel U-forms, additively manufactured stainless steel components, a nickel-based super alloy weld and an aluminium casting. Where possible, the widest range of measurement techniques have been applied and the results comparing the resulting measurements of residual stresses have been tabulated. Specific conclusions have been made regarding the application of the main techniques on each component. Specifically, it will be shown that each of the techniques considered have specific domains of application and specific instances where LRI measurements have particular importance. The challenges of determining residual stresses will be highlighted regardless of technique, and that often complementary techniques are desirable for certainty.

The present report is organised as follows. First, a section has been provided that has the benchmark samples briefly described, along with the relative advantages or challenges to determining residual stresses contained within. This section also describes the techniques employed, along with a description of errors or uncertainties that each considered technique can return. Next, a section detailing how results were communicated within the working group, as well as the manipulations that were necessary for comparison between techniques. The subsequent section describes all measurements carried out and compares the results obtained for each technique. Where applicable, a relevant appendix appears which describes a specific measurement description.



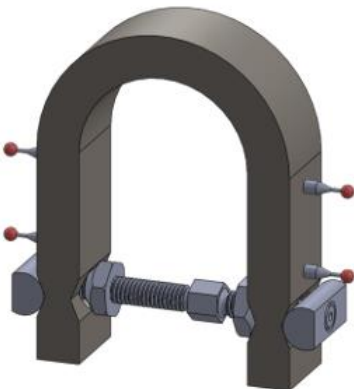
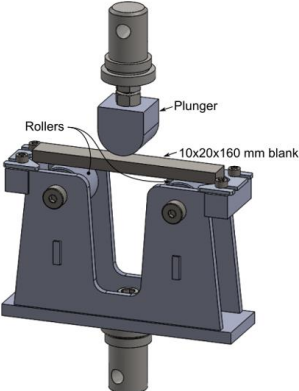
2. Background

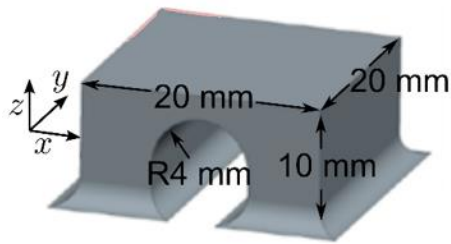
The round robin exercise carried out spans four different types of components and five different techniques. Each component has a different underlying material system and processing history, which poses challenges when determining how a given measurement technique will operate and determine residual stress (RS). This section is aimed at describing the various components considered, their specific challenges, the techniques that have been applied and how their respective errors or uncertainties are tabulated.

2.1 Components considered

A wide cross-section of how residual stresses manifest in modern processing of metals has been considered. They encompass sources of residual stress such as plasticity-induced misfit strains that can occur during forging operations, through to the thermally induced misfit strains and microstructure evolution associated with solidification events. The designs of these benchmark components have been devised to include multiple sources of stress. Further, with the manufacturing details provided, it surmised that these benchmark specimens could be reproduced to evaluate, to help develop, or validate new residual stress measurement techniques. Finally, the configuration of these benchmark samples has been devised on the basis such that all potential measurement techniques can be employed, be they non-destructive such as those available at LRIs, as well as laboratory techniques, which can also be destructive. The samples are briefly described in Table 1. For a full description, see EASI-STRESS D2.1 – Reference Samples.

Table 1 - The four categories of samples: a) U-flexure and U-bend, b) AM arch, c) TG6 weld, and d) cast wedge.

	<p>U-flexure:</p> <p>'U' shape cut from ferritic steel S355J0Z35+N in the as-rolled condition with electro-discharge machining. The loading mechanism allows both tension and compression applied to the legs. After removal of the load, it serves as stress-free reference.</p> <p>Advantage: Simple elastically applied stress state, bulk stresses can be directly calculated.</p>
	<p>U-bend:</p> <p>'U' shape produced by plastic deformation of a flat steel strip. The steel strip is cut by electro discharge machining from the same material as the U-flexures.</p> <p>Advantage: Introduction of similar physical footprint to flexure samples, qualitatively known stress distribution.</p>


AM arch:

Structure produced by laser powder bed fusion (L-PBF) additive manufacturing using stainless steel 316L powder with a powder particle size of 15-80 μm and a layer thickness of 50-60 μm . As-built samples and samples heat treated for stress relief.

Challenges: High levels of residual stress. Variation in solidification history leading to variations in stress-free references.


TG6 weld:

Sample used previously in the Network on Neutron Techniques Standardization (NeT) for structural integrity task group 6 (TG6). It is a Ni-based plate (alloy 600; 150 mm \times 200 mm \times 12 mm) with a 3-pass slot weld (76 mm \times 5 mm \times 5 mm) made using an automated gas tungsten inert gas weld (GTAW/TIG) with a Ni-based alloy 82 filler material.

Challenge: Large grain size in weld and variations in stress-free references.


Cast wedge:

A wedge-shaped sample (alloy AlSi7Cu0.5Mg) with outer dimensions of 107 mm \times 62 mm \times 90 mm. The production includes casting, quenching, and a two-stage precipitation heat treatment.

Challenge: Heterogeneous microstructure, both from texture as well as in composition/phase distribution. Large grain size.

2.2 Techniques applied

There are two LRI-based techniques (ND, SXR) and three lab-based techniques (LXRD, HD, and CM - see Table 2) for assessing residual stress considered in the EASI-STRESS project.

LRIs hosting high-energy SXR and ND techniques enable the measurement of RS within the bulk of metallic parts. RS is averaged within the gauge volume and information is provided about the different phases forming the material at different length scales. The basic physical principles are the same for all diffraction techniques (Hutchings *et al*, 2005), as they rely on the crystal structure of the analysed phase to ascertain relative changes in the distance between parallel atomic planes oriented with their normal parallel to the scattering vector. The interplanar distances are calculated using Bragg's law via the beam wavelength and the diffraction angle.

Amongst the three lab-based techniques, two are local techniques (LXRD and HD) in which a region is subjected to measurement in the overall component. The third is the CM, which is a strain-relief method that provides an entire cross-sectional map of a single stress component, as well as the portions of other components that are relieved by its application.

All methods to rely on capturing residual *strain* or change in shape of a component as an intermediate step, prior to applying elastic constants to obtain stresses from these strains. As strain is the measurement of a change in dimension, a reference starting point needs to be considered. LRI techniques are particularly sensitive to this reference point, and require a stress-free reference to determine this. This is referred to subsequently as a ‘d₀’ sample, which should contain the same metallographic features as the subject material, but stress relieved.

The techniques are briefly described in Table 2. For a full description, see EASI-STRESS D2.2 – “Best practice guidelines”.

Table 2 - Techniques for RS characterization within the EASI-STRESS project.

Technique	Advantages	Disadvantages	References
ND	Large penetration depth; cubic gauge volume	Low intensity	Hutchings et al, 2005
SXRD	High intensity (quickly assess a large number of points)	Medium penetration depth, elongated gauge volume	Withers 2013
LXRD	Good availability compared to LRI	Limited to surfaces; semi-destructive	NPL 2020
HD	Good availability compared to LRI	Limited penetration; Destructive	Schajer and Whitehead 2013
CM	2D results obtained	Destructive; complex data analysis	Prime and DeWald, 2013

2.3 Error estimation for techniques considered

Measuring residual stresses can be very challenging (see references in Table 2), with many opportunities for errors to arise. Below are the main errors associated with the techniques applied here are briefly considered. For more detailed analysis the reader is directed to further reading.

a) Neutron diffraction (ND)

There are two main categories of errors in a neutron diffraction experiment for strain and stress determination. The first is related to the sample alignment error which includes the positional accuracy of the beam as well as errors associated with positioning the sample on the sample stage. The magnitude of the error depends on the alignment and metrology system employed as well as the type of sample stage used. A requirement is to have the reference point coincident with the instrument centre of the ω -rotation axis within an accuracy of 10% of the neutron gauge volume width (Ramadhan *et al*, 2021). As part of the *BrightnESS*² project (Brightness), a Neutron Quality Label (NQL) was introduced to develop a common calibration procedure to quantify the positioning error. The second source of errors is related to measuring the diffraction angle relative to a stress free reference. This stems from fitting the diffraction peaks depending on the peak width and shape as well as on the peak-to-background ratio. Depending on the material, the ability to scatter or absorb neutrons can vary widely. Additionally, the detected signal depends on the microstructure

(e.g. large or non-uniform grain size). The precision of the measured *change* in lattice parameters is usually around $\pm(0.5-1.0)\cdot 10^{-4}$ which translates to a precision in stress, depending on the material, for example $\pm(20-40)$ MPa for a ferritic material (Schajer, 2013). More detailed information about the calculation of uncertainties and errors can be found both in the EASI-STRESS deliverable 4.2, but also in the ISO 21432:2019 standard (ISO).

b) High energy synchrotron X-ray diffraction (SXR)

Sources of errors mainly originate from sample alignment and peak fitting and, if applicable, from the $\sin^2\psi$ method. The synchrotron radiation allows small beam cross-sections well below $20\ \mu\text{m}$; with focussing optics beam cross sections less than this are possible. Errors in positioning is mainly affected by the accuracy of the sample alignment (either with a Cartesian-type stage or an Eulerian cradle). The peak fitting error, calculated by error propagation, determines the final stress error. A white beam usually provides diffraction peaks with higher signal-to-background-ratio when compared to a monochromatic beam coupled with a conical slit cell (CSC), i.e. errors are smaller for the former (Staron et al, 2014). However, when the $\sin^2\psi$ method is applied, final errors are smaller for both techniques, compared to measurements in only two directions. The precision of the measured change in lattice parameters is typically around $\pm(1.0-2.0)\cdot 10^{-5}$.

c) Laboratory X-ray diffraction (LRXD)

Three types of uncertainties are considered for resolving the two main stress components (normal and shear) captured with this technique. The first are statistical uncertainties determined from the error relative to the positions of the diffraction peaks. This can be affected by weak diffraction peaks when gauge areas are too small. This can increase statistical scatter in the obtained signals. The second is the residual of the least square fitting of the peaks themselves, which is a result of heterogeneity of the material to be measured. Positional errors are also possible due to diffractometer misalignment with respect to the sample coordinate system.

Calibration specimens are employed to ensure that the sample positioning system with respect to the diffractometer are captured. These measurements are taken into account to apply correction on the determination of the peak position during the diffraction profiles treatment. Care should be taken in assuring that the intensity of the diffracted peaks compared to the background is sufficient and that the measured 2θ range is sufficient for proper peak fitting.

The validity and reliability of any obtained results are evaluated according to the EN 15305:2008 standard (NF, 2009). The use of this standard and its recommendations allow for the evaluation of whether the material properties can be assumed to be isotropic and homogeneous. This is carried out by determination of the relative intensity ratio of the diffraction peaks, ensuring the absence of multiple peaks and that the $\sin^2\psi$ trend is appropriate for the underlying material system and stress. Non-linearity of the $\sin^2\psi$ curve is usually the main source of error of the measurement and most commercial systems output the fitting error of the $\sin^2\psi$ curve as the error in the measured stress value. Finally, using incorrect x-ray elastic constants in the stress evaluation can give systematic but significant errors in the evaluated stress values.

d) Hole drilling (HD)

Two different means of determining surface strains associated with hole drilling have been applied with different underlying errors associated with each. The first technique, Electronic Speckle Pattern Interferometry (ESPI) is an optical technique, with errors associated with a combination of surface preparation/features, camera alignment, hole irregularities and other factors. The second, which involves the use of a strain gauge rosette, has errors associated with the strain gauge itself as well as hole/drilling irregularities. Errors for these results have been estimated to be a conservative +/-10 MPa, ESPI techniques have reported less than this for shot-peened aluminium [Rickert, 2016], as has strain-gauge based techniques [Stefanescu, 2006].

e) Contour method (CM)

As there are multiple experimental and analysis steps to performing contour method analysis is often difficult to ascribe singular sources of error. Interlaboratory measurements of identical components with this technique which have been reported in the literature, where it was found that reproducibility can range between 0.5 to 55 MPa, with errors tending to be higher near cutting plane boundaries. The same study identified the standard deviation in measurements of the same stress field to be 17.6 MPa within 1.0 mm from plane boundaries [D'Elia, 2022]. Therefore, where contour method results have been reported without any specific artefacts present, error has been reported as a constant, conservative +/- 10 MPa.

2.4 Summary

It can be seen that a cross section of benchmark samples have been considered, with each posing different challenges associated with determining residual stresses. The results of the round robin exercise presented subsequently should highlight the challenges faced, and how errors have been reported. The following section describes the procedures employed to compare results between the varying applications of the residual stress determination techniques.

3. Inter-technique reporting procedure

As reported in EASI-STRESS deliverable 2.2, a standardised template for reporting results was developed for directly comparing results for directly comparable applications of residual stress determination. Further, reporting data in this format provided the ability to aid interpretation of any discrepancies in interpretation. This is shown schematically in Figure 1.

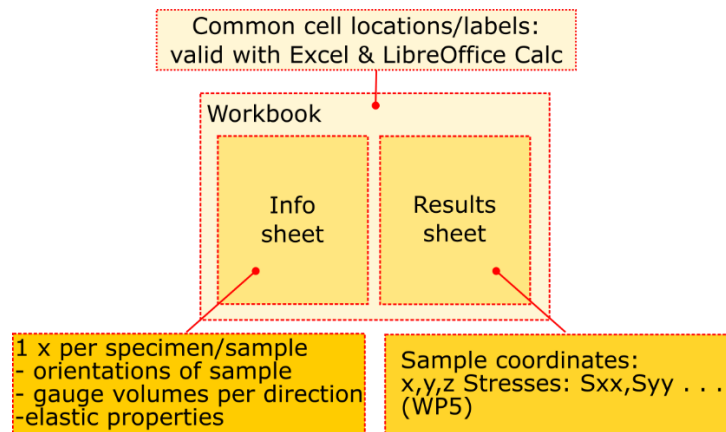


Figure 1 - Workbook-based format suitable for reporting inter- and intra-technique residual stress measurements.

Results were reported in a tabular form with raw results provided along with a short description on how to interpret them. These measurements are typified by lab-based techniques that were employed for superposition techniques, or limitations of the techniques themselves did not lend them to directly compare stress values for a given orientation at directly comparable locations. Wherever possible, the inter-technique comparison approaches described in deliverable 2.2 were employed. These are summarised in Table 3.

Table 3 - Overview of suggested geometric considerations when considering inter-technique and FEA comparisons of residual stress measurements and predictions.

Technique	Geometric boundaries stresses are averaged over	Inter-technique comparison
SXRD, ND	Spherical* volume with radius equal to the largest dimension of the SGV.	Direct comparison between geometric boundaries for HD and LXRD, resampled CM results.
LXRD, HD	Equivalent circular area equal to illumination dimensions for LXRD or starting hole diameter for HD.	Direct comparison between geometric boundaries for SXRD and ND, resampled CM results.
CM	Point-based interpolation from CM FEA calculation.	Averaged stresses at nodes or integration points lying within respective geometric boundaries of subject technique.**

*For cases of extreme differences in SGV dimensions, an ellipsoid can be considered. **The stresses at the centroids of overlapping gauge volumes can also be interpolated.

Acquiring results of stresses at specific locations for the various components required transforming the coordinate system employed by the measurement technique to that of a pre-defined component coordinate system. This required using pre-defined datum features which determined the rigid body transformation needed to bring the measurement coordinate system to the component coordinate system. The method employed for coordinate system transformation was an iterative closest point (ICP) algorithm. This involves a factorization the coordinate matrix of datums or fiducial points to solve for a transformation matrix T that minimizes the Euclidean distances between all points considered. Once this transformation matrix was found, then it could be applied to the stress tensor for reorientation such that:

$$\sigma_c = T \cdot \sigma_m \cdot T^T$$

where σ_c is the component stress tensor, and σ_m is the measurement stress tensor. This was applied where necessary; techniques which did not produce an entire stress tensor or did not have all stress components reported were addressed by ensuring that the main axes of each system were aligned. This allowed for reassigning/substituting normal components of stress without transformation of the entire tensor. A select number of LXRD measurements that required a tensor-based manipulation but did not have shear components reported. In this instance, the shear component τ_{xy} was estimated to be the difference in σ_x and σ_y .

4. Results

4.1 Ferritic steel U-forms

Two variants of these components were considered. The first was that of externally loaded flexures such that an internal stress state could be obtained by a companion finite element model. The degree of loading of each flexure was obtained by measuring the deflection of the component either directly or from inherent datum features. The second variant were made from the same material, but plastically deformed such that they contained a true residual stress that could be assessed via laboratory means. A depiction of the variants and their forms is provided in Figure 2.

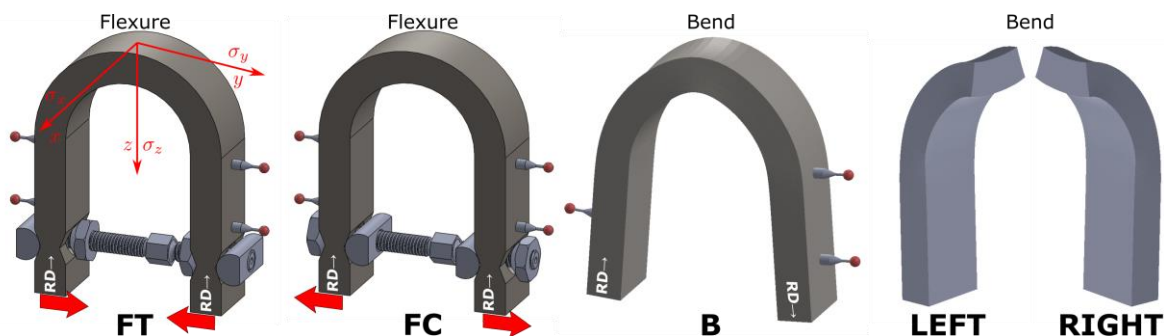


Figure 2 - Ferritic steel U-form configuration and coordinate system. Flexures (FT and FC) were configured to load the extrados of the 'U' in tension and compression, respectively. Bent samples (B) were plastically deformed to create a true residual stress. 'RD' indicates the rolling direction of hot-rolled plate for their manufacture. 'Left' and 'Right' B-type samples were subjected to LXRD measurements after contour cutting.

Kits were supplied formed of 3 flexures (loaded in tension, compression and unloaded for a reference stress-free d_0), the means to capture the level of deformation applied, a single bend, and a 3.5 mm pin to be employed as a d_0 . All flexures were supplied in the as-electrodischarge machined state; the B-type samples were bent from electrodischarge machined blanks. A further 3 bends were considered for laboratory techniques; B1, B2, and B3 were subject to CM measurements, and B1 and B2 (each having a left and right) were further subjected to LXRD. A summary of each of the components considered is given in Table 4.

Table 4 - Techniques applied by participants to the round robin in order to assess residual stresses in the ferritic steel U-forms

Component	Technique/application	Participant
FT	Neutron diffraction line scan at midplane (σ_x , σ_y and σ_z)	ILL
	Synchrotron X-Ray diffraction line scan at midplane (σ_x , σ_y and σ_z)	Hereon
FC	Neutron diffraction line scan at midplane (σ_x , σ_y and σ_z)	ILL
	Synchrotron X-Ray diffraction line scan at midplane (σ_x , σ_y and σ_z)	Hereon
B0	Neutron diffraction line scan at midplane (σ_x , σ_y and σ_z)	ILL
	Synchrotron X-Ray diffraction line scan at midplane (σ_x , σ_y and σ_z)	Hereon
B1	Contour method at midsection (σ_y , partial σ_x and σ_z)	UoM
	Laboratory X-Ray Diffraction line scans on each resulting contour cut face (partial σ_x and σ_z)	UoM/EDF
B2	Contour method at midsection (σ_y , partial σ_x and σ_z)	UoM
	Laboratory X-Ray Diffraction line scan on resulting contour cut face (partial σ_x and σ_z)	UoM/DTI
B3	Contour method at midsection (σ_y , partial σ_x and σ_z)	CETIM

While cross-comparison between the flexure variant (FT and FC) is only possible between ND and SXR, the 3 point bend variant (B0-3) provided more opportunities to compare the full range of techniques that have been considered in EASI-STRESS. After contour cutting B1 and B2, the halves from each side of the cut were measured by UoM and then measured by partners with LXR. The expected result is that both line scans should provide identical results on either side of the cut. Further, there was the potential to combine the results of LXR and CM such that they could be compared to those obtained by ND and SXR via superposition.

a) Measurement overview

As detailed earlier, results from the flexures (FT and FC) could only be compared directly to the results obtained from a model due to slight differences in loading of each component at each facility, and different elastic constants employed in translating captured strains to stresses. A detailed description of ND and SXR experiments can be found in Appendices 1 and 2, respectively. The elastic modulus, Poisson's ratio, and specific deflection values recorded were employed to generate predicted normal stresses at the positions measured with a linear elastic finite element analysis. The difference between predicted values and those measured has been used as a point of comparison. With this approach, the differences in loading of the samples as well as potential differences in elastic properties employed can be corrected. The coordinate systems and datum features employed for these samples were such that a direct spatial comparison of all normal stresses was straightforward.

For the B-type samples, a direct comparison between stress values obtained from LRI diffraction techniques was possible. However, for the lab-based techniques, only the CM could provide a single normal stress to directly compare to the diffraction results: σ_y . This was the stress component that had the highest magnitude. Three of these samples were subjected to CM (see Appendices 3 and 4), with two of the samples having each of their left and right cut faces electropolished to a depth of $\sim 150 \mu\text{m}$ such that LXR could be applied by various participants. In these latter samples, measurement locations were indicated to be taken relative to fiducial points located on the corners of the cut profile. These fiducial points were then employed to reorient them i) with respect to each

other and ii) to the CM data. Reorientation and registration was carried out according to techniques described in Section 2.

It was found that of the 3 CM results, there was one return that was clearly qualitatively better than the others when compared to what the RS profile should look like for a 3 point bend, and there was one LXRD return that was registered the best with the measurement positions employed by the LRIs. Therefore, a combination of this CM result and LXRD result for σ_x and σ_z was used for comparing to those returned by LRIs.

b) Results and cross-comparison of techniques

The following results are presented in the order of flexures first (FC and FT), then CM results of the B-type samples, followed by LXRD results, and finally a comparison of ND, SXRD, CM, and CM + LXRD.

The results for the difference between measured and predicted stress for the FT and FC components are given in Figure 3 and Figure 4. Here, as the measured stresses have been corrected for differences in a) elastic properties and b) differences in loading, such that the model reflects measured conditions. Any difference from 0 MPa for either ND or SXRD shows regions which disagree with the model. Overall, between the two techniques and all components, ND results seems to come closer to being reflecting modelled conditions as compared to SXRD. Notable departures from this trend are at the extremities, very close to the extrados surface (e.g. $z = 0$, and intrados, $z \cong 10$). This could be because of two factors: first, the electrodischarge recast layer could be affecting regions which are lightly loaded, and the second is where the samples were most heavily loaded (e.g. 85% of yield) and small scale plasticity/Type I yielding could have taken place.

SXRD results showed that the flexures were loaded minimally, but do not demonstrate the near-surface effects seen for ND. However, a difference of 25-50 MPa can be seen for between SXRD and ND in the x and y directions. Stresses calculated with the Von Mises (VM) expression (Figure 5) shows marginal evidence that there could be plasticity occurring near-surface, with weak plateaus proximate to the extrados/intrados surfaces.

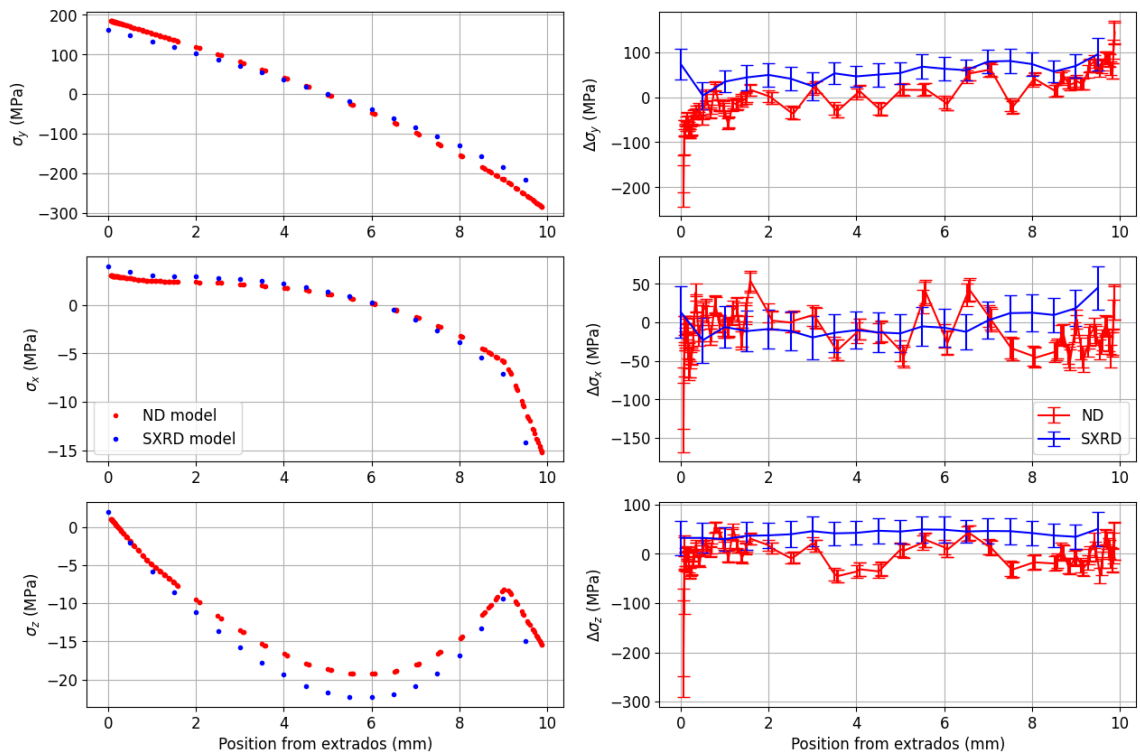


Figure 3 - Results from FT flexures. Modelled stress distribution based on reported elastic properties employed and displacement (left column), difference in determined stress values by diffraction from model (right column).

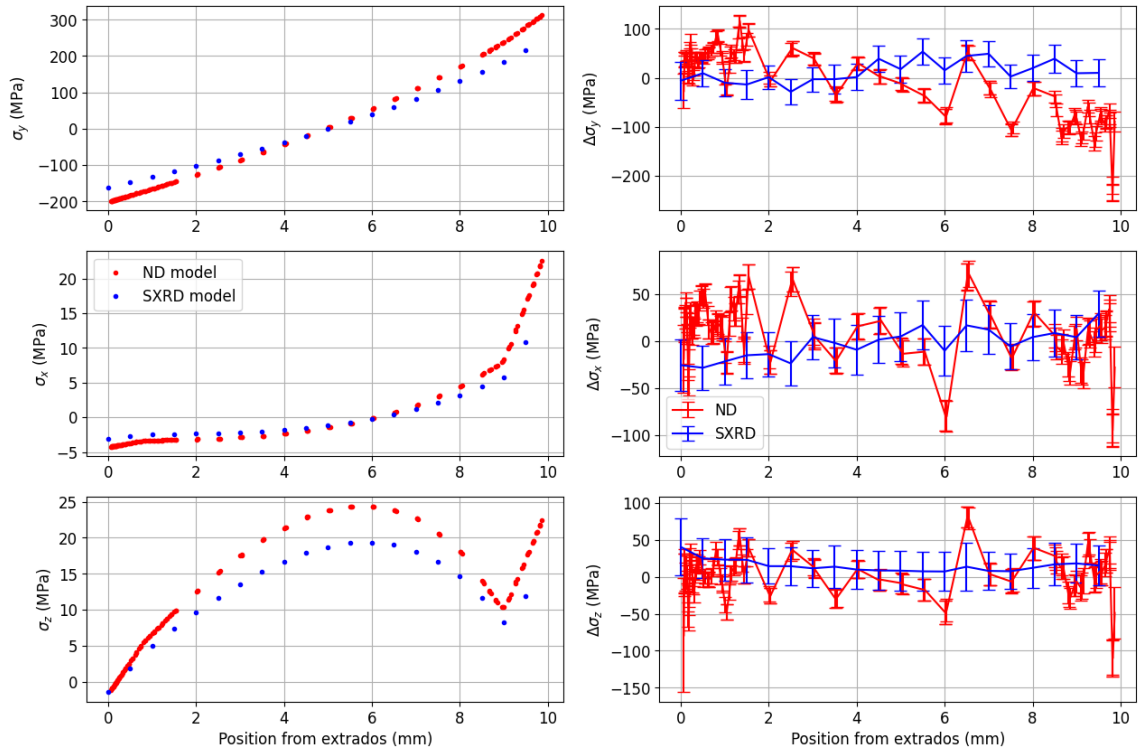


Figure 4 - Results from FC flexures, presented in the same format as those for the FT (Figure 3).

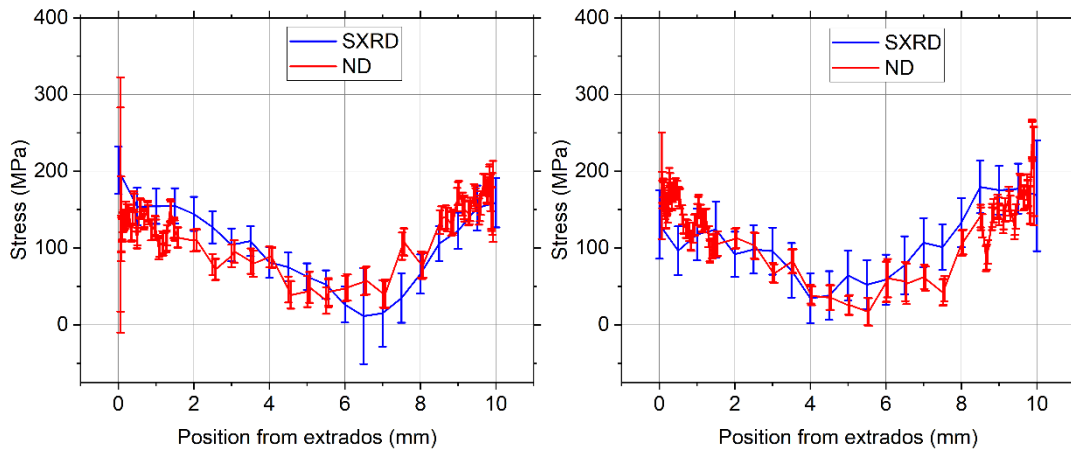


Figure 5 - Results from FT (left) and FC (right) flexures, presented as stresses calculated with the VM formula.

The contour method application to the B-type samples showed very different results between returns (Figure 6). Of the three results obtained, B3 most clearly demonstrated the type of stress profile in this orientation expected: compression at the extrados, a region of elevated tension reflected by compression over the bending moment, and finally tension at the intrados. The lack of symmetry about the x axis of all of the results obtained are attributed to a slight twist in the bends, which resulted in a deformation that was not purely bending, but having some elements of torsional deformation about the y axis.

The results for B1 and B2 clearly show this torsional effect more prominently, however the magnitudes obtained for σ_y do not agree between identical applications of the same technique. Reasons for discrepancies between the B1 and B2, and ultimately B3 can be attributed to two potential causes: rigid body movement of the component during cutting and potential cutting induced plasticity, particularly at the intrados.

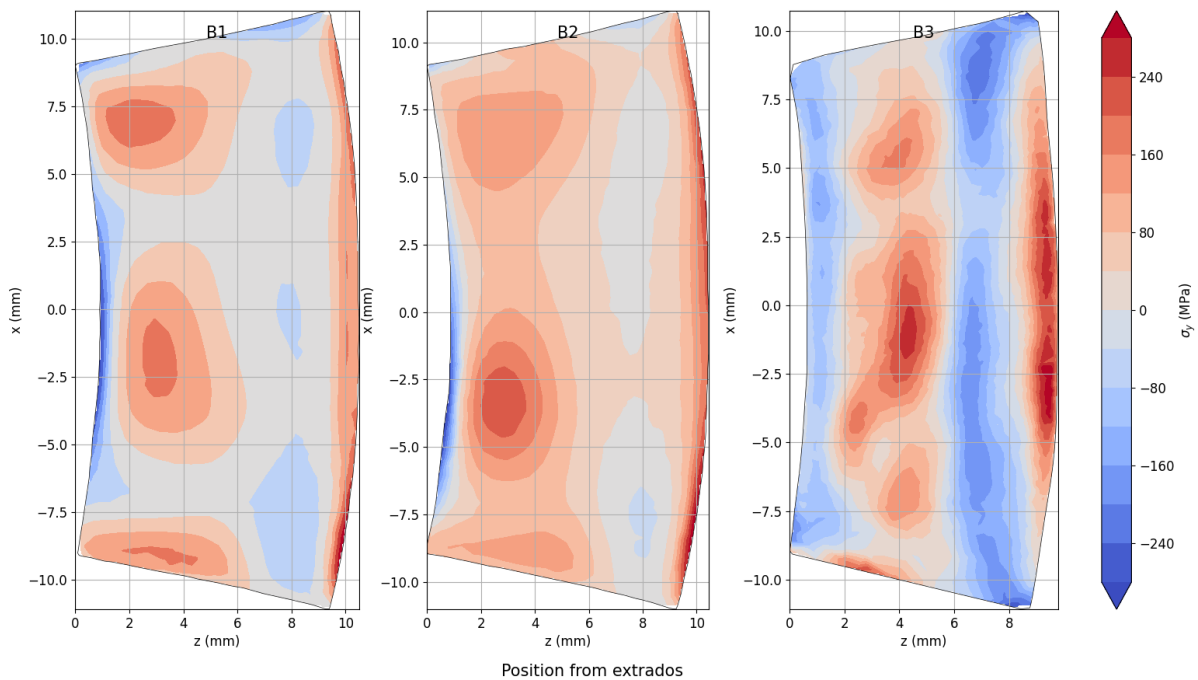


Figure 6 - Contour method results for the σ_y stress component of the B-type samples.

Regardless of the outcome of stresses obtained with CM, the resulting two halves should have the same stresses acting on the cut plane retained (σ_x , σ_z and τ_{xz}). That is, the resulting left and right halves of B1 should have the same planar normal stresses (σ_x and σ_z) in each half, with the same true for B2.

The in-plane stresses remaining after contour cutting were measured by LXRD at two different labs for these B-type halves (Figure 7 to Figure 10) by different participants. Of the two measurements carried out on B1, one set not show agreement between halves (right versus left), while one did. Stress extrema locations in this latter case lined up almost exactly, once considering the variation in measurement location between each half. Both measurement providers had difficulty in capturing fiducial points. This can be observed with discrepancies found between the alignment of fiducial points and the corresponding outline after a least-squares rigid-body alignment took place. This alignment could only be further improved by an affine (out of plane) transformation. Therefore, it is apparent that there was difficulties in fixing the measurement surface such that it was orthogonal to the scanning direction. Both returns provided values of normal stresses (σ_x and σ_z) at the same locations on each half (e.g. the coordinate system of both stress component measurements on each half was identical).

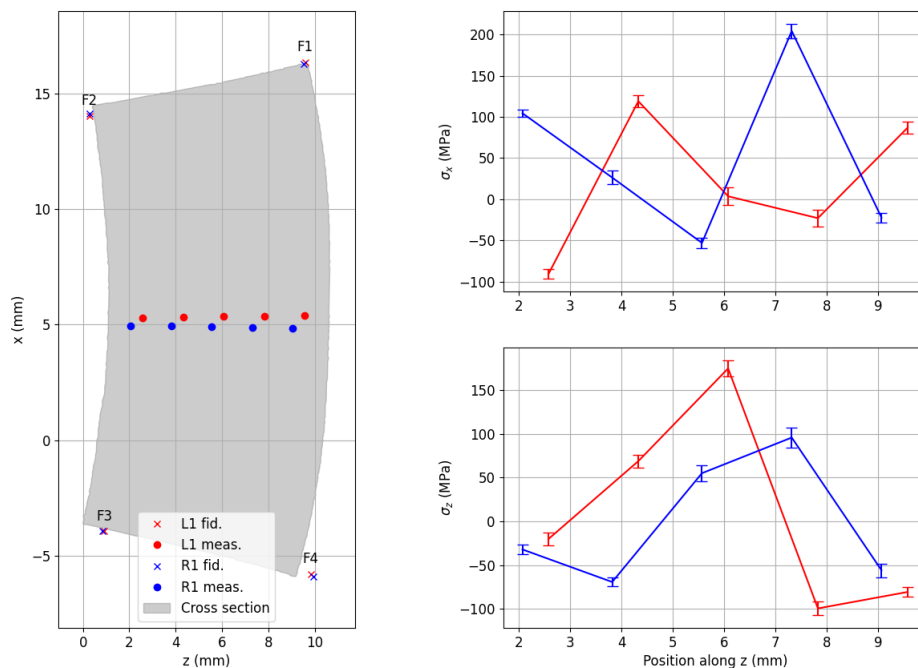


Figure 7 - LXRD results returned by a participant of the left side of B1 (L1) and right side (R1) of the same. Fiducial points F1-4 aligned with a least-squares fit of the sample outline obtained from the contour cut.

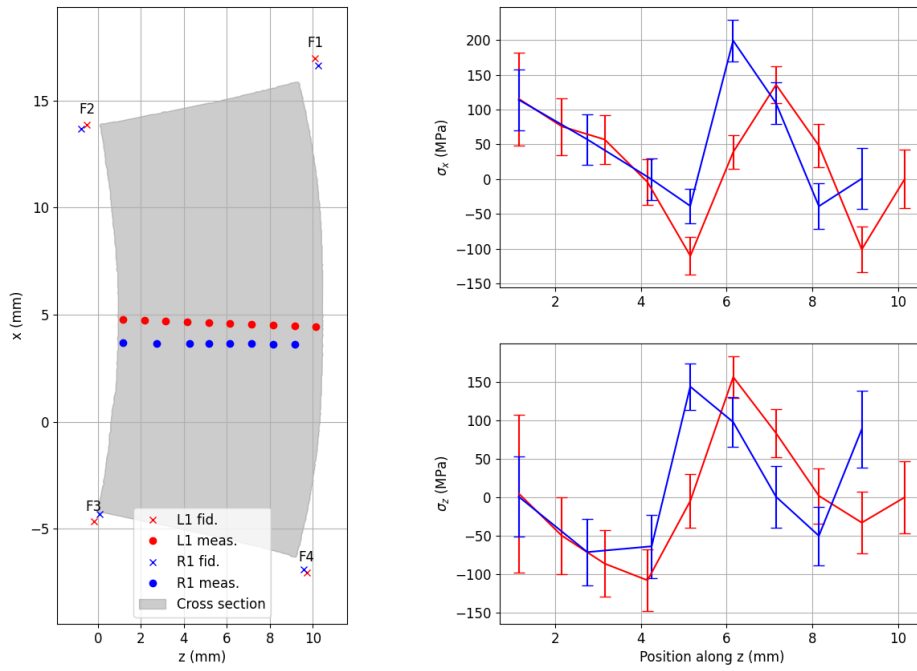


Figure 8 - LXRd result of B1, with data presented in the same manner as Figure 7 for a second participant.

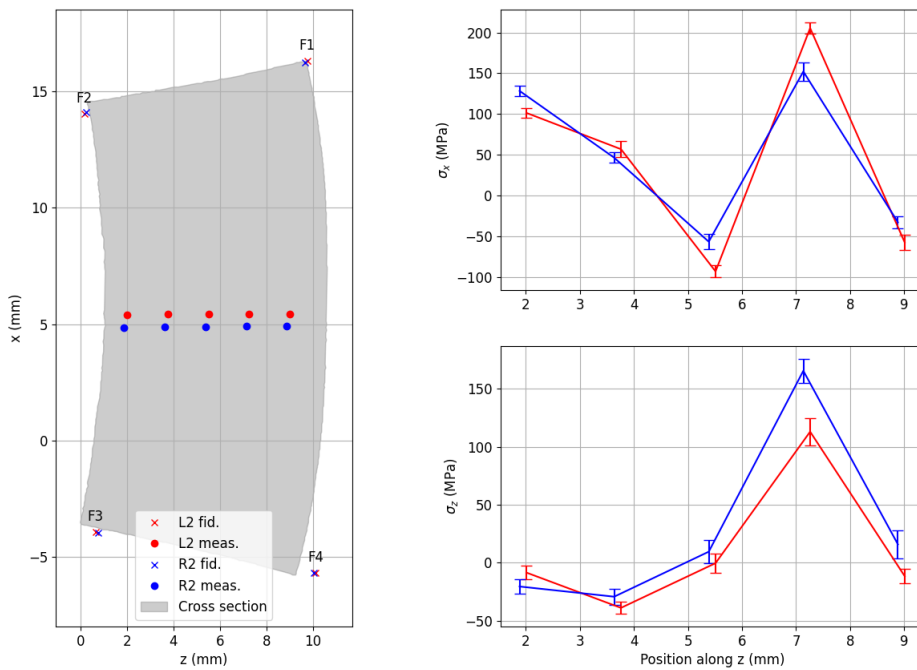


Figure 9 - LXRd results for B2, with data presented in the same manner as Figure 7.

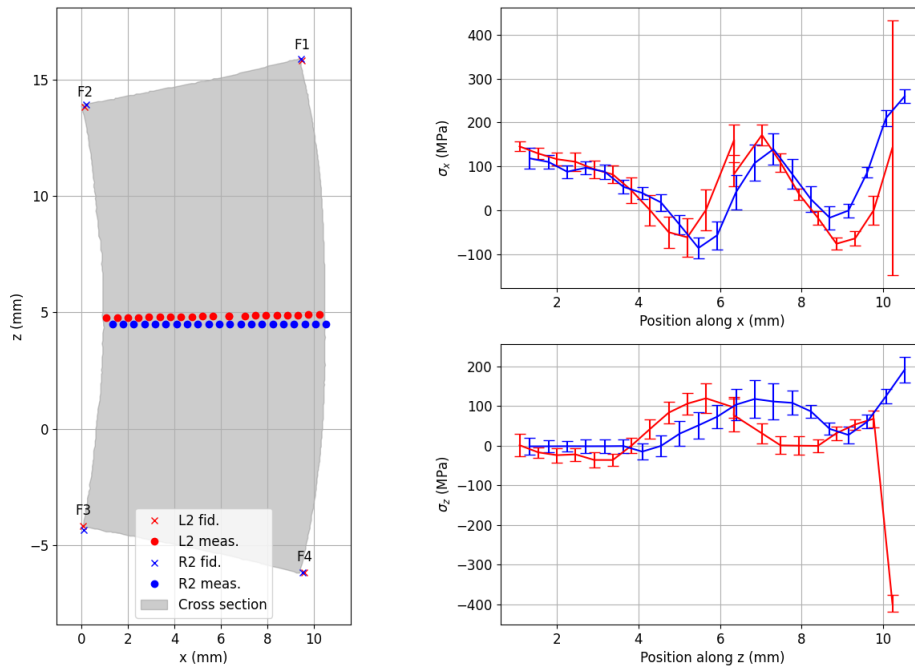


Figure 10 - LXR D result of B2 by a different participant than those shown in Figure 9, with data presented in the same manner as Figure 7.

For LXR D results returned for B2, the stress peak positions were identical for each side for σ_x for both providers. While one provider had an excellent agreement for the two halves between peaks for σ_z , the other provider had less agreement for this stress component. While the first provider employed the same coordinate system for reporting both normal stress components, there was an issue as before with capturing the fiducial points accurately or keeping the measurement surface in-plane. The second provider moved the sample between measuring components and reported an additional set of fiducial points. For the purposes of direct comparison for a single coordinate system, the positions for σ_x and σ_z were averaged. This difference in positioning could explain why all points for R2 (Figure 10) appear in the cross-section at the intrados, while the last point measured at the intrados appears as though it is outside of the component; the opposite is true for L2: it appears as though there is a point outside of the cross-section, but a valid stress has been measured here.

In comparing all the results (Figure 11), there is an excellent agreement between both diffraction techniques for all stress components. Further, there is also a reasonable agreement between CM and LRI diffraction techniques for σ_y in terms of the general trends observed, and in select regions is within the uncertainty limits of both ND and SXRD. The differences in stress peak position can be attributed to data smoothing employed during CM analysis or the potential of cutting induced plasticity; both diffraction techniques agree as to the location of stress peaks and are close in agreement as to their magnitudes (error limits within ~ 40 MPa).

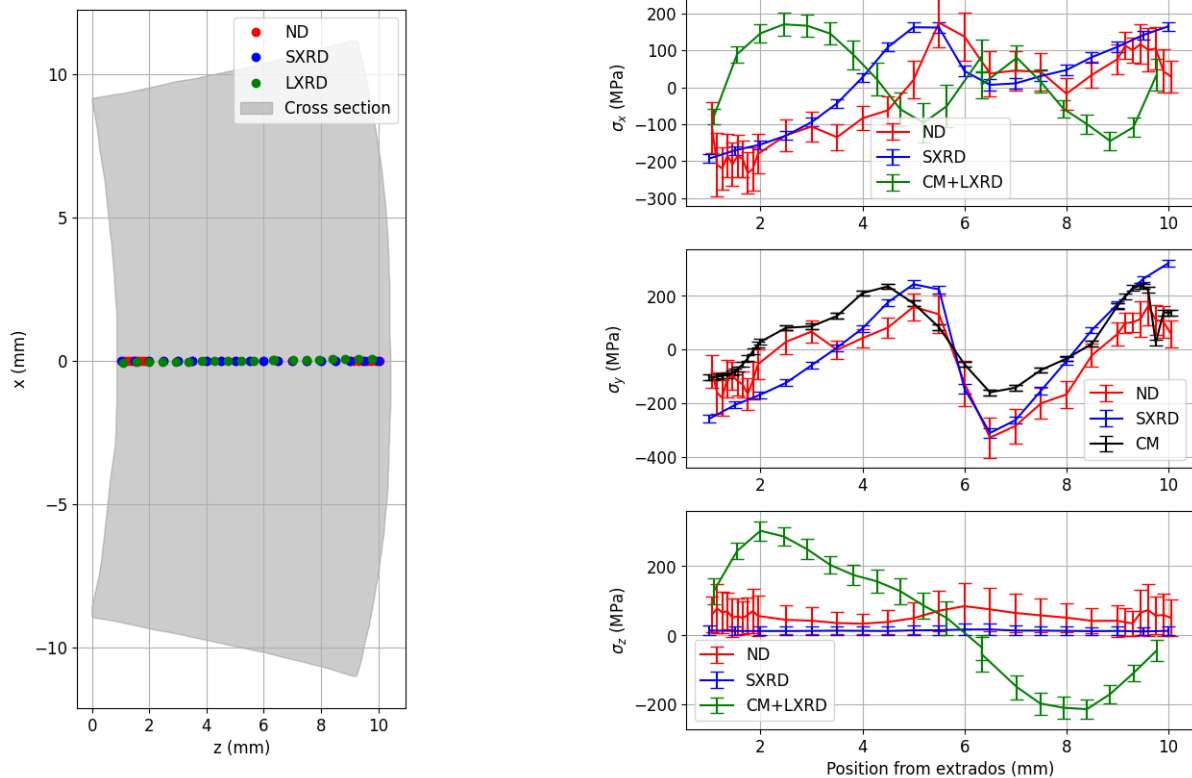


Figure 11 - Comparison of all directly comparable results. Note that the CM+LXR results for σ_x and σ_z have been acquired from B2, while σ_y is from B3.

It is very clear that the in-plane stresses determined by LXR after CM does not agree with either of the other two methods. The main reason for this difference between diffraction and combining CM with LXR is that the latter relies heavily on the CM result being accurate; otherwise even a very accurate application of a second technique will have an invalid foundation.

c) Summary

Two variants of ferritic benchmarks have been measured, one flexure-type externally elastically loaded to provide an analytically derived internal stress both in tension and compression (FT and FC) and another variant containing plastically imposed residual stresses through 3 point bending (B). The latter was also subjected to an interlaboratory measurement campaign using destructive techniques. While the flexures and bend samples were shown to provide accurate results via LRI techniques, only one contour method measurement found to be coherent with expectations and diffraction measurements. The interlaboratory LXR and CM measurements demonstrated a wide range of results which did not correspond to expected underlying trends in stress. This underlines the need for LRI measurements for certainty.

4.2 Powder-derived stainless steel additively manufactured arches

Two different laser-based powder-bed fusion (L-PBF) machines were employed by ArcelorMittal and Volum-e to produce AM samples from 316L stainless steel. These samples were supplied in two variants: one as-built, and the second in the as-built and then subsequently heat treated. The heat treated samples were subjected to 700 °C for 2 hours and cooled inside the furnace under an argon atmosphere to avoid surface oxidation. All components were left on their respective substrates

during processing and measurement. The nominal geometry of the components and coordinate system is shown in Figure 12. Multiple samples of each type were circulated to consortium members for measurement of normal components of stress applicable or accessible via their respective techniques. These were measured predominantly located along the z axis at the centre of the component. Further measurement points were taken at other locations by some LRI participants, but are not directly comparable for all participants as detailed in the subsequent section. The measurements carried out and sample designations are summarised in Table 5.

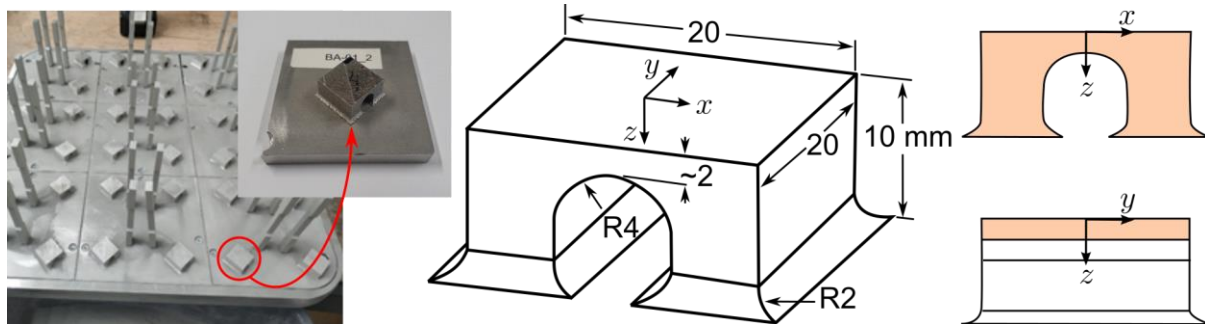


Figure 12 - LPBF sample (left) with nominal dimensions and coordinate system employed (centre). Section planes of the component on primary axes are shown shaded on the right; specifically the y plane (right top) and the x plane (right bottom).

Table 5 - Techniques applied by participants to the round robin in order to assess residual stresses in the additively manufactured stainless steel arches.

Component	Technique/application	Participant
ArcelorMittal as-built (AB)	Neutron diffraction 4 off line scans on y plane: σ_x , σ_y and σ_z	ILL
	Synchrotron X-ray diffraction 4 off line scans on y plane: σ_x , σ_y and σ_z	Hereon (P07 – SXR1, P61A – SXR2) and ESRF (SXR3)
	Synchrotron X-ray diffraction 1 off line scans on y plane: σ_x , σ_y and σ_z	
	Layer-removal LXR: σ_x and σ_y	CETIM
	Contour method: σ_x and σ_y	UoM (CM1)
	Contour method: σ_y	CETIM (CM2)
ArcelorMittal heat-treated (HT)	Neutron diffraction 4 off line scans on y plane: σ_x , σ_y and σ_z	ILL
	Synchrotron X-ray diffraction 4 off line scans on y plane: σ_x , σ_y and σ_z	Hereon (P07 – SXR1, P61A – SXR2)
	Layer-removal LXR: σ_x and σ_y	CETIM
	Contour method: σ_x and σ_y	UoM
Volum-e as-built (AB2)	Neutron diffraction 3 off line scans on y plane (σ_x , σ_y and σ_z).	ILL
	Layer-removal LXR: σ_x and σ_y	CETIM
	Contour method - σ_y	CETIM
Volum-e heat-treated (HT2)	Layer-removal LXR: σ_x and σ_y	CETIM

a) Measurement overview

For the purposes of comparison, the approach taken was to compare those in the as-built (AB) and heat-treated (HT) conditions, wherever possible, regardless of supplier. Therefore, orthogonal residual stress components accessible by each technique have been compared simultaneously to those supplied by ArcelorMittal (AB/HT) and Volum-e (AB2/HT2). Fewer of the Volum-e components were available to the overall consortium, and therefore most of the results that were returned were carried out on the ArcelorMittal components. However, there was sufficient coverage between techniques and providers to provide a comparison between LRI diffraction techniques as well as lab-based ones, both comparing condition of the component and also the differences between supplier types. For laboratory techniques, a depth resolved LXR technique was applied by CETIM to all four variants; as-built for both ArcelorMittal and Volum-e, as well as their heat-treated variants. CETIM was also able to provide a CM measurement of σ_y between the as-built ArcelorMittal and Volum-e.

Beyond differences in specific implementations of the LRI diffraction techniques applied (e.g. differences in underlying physics of beam interactions, gauge volumes, etcetera), the following results have employed different stress-free reference values (d_0). The approach taken to measure d_0 can be critical (Withers et al, 2007). For the present ND measurements, 'raw' powder, or unaltered LPBF feedstock powder has been employed as a stress-free reference. The same reference was employed for the ESRF measurement. Hereon, however, employed a d_0 'comb'. That is, a segment of the component (AB, AB2, HT and HT2) was sectioned by electrical discharge machining to mechanically relieve stress, and this was subject to diffraction measurements to set a baseline. Appendices 5 and 6 provide additional details on the application of ND and SXR techniques performed by the ILL and Hereon, respectively. Gauge volumes and spatial arrangement of measurement regions remain consistent and directly comparable for all measurements. Appendix 7 shows results of additional scanned regions for LRIs.

The application of LXR and CM application to these parts was complicated by high amounts of residual stress, even in the heat-treated condition. While all techniques found that the application of a heat treatment reduced the overall stress, it was still sufficient to cause localised yielding during material removal techniques. As all mechanical or strain-relief measurement techniques rely on elastic release of stress, this significantly compromised aspects of the measurement. For the layer-removal LXR technique, significantly higher stresses were determined as layers were removed. For CM, UoM's cutting strategy caused localised yielding (cutting induced plasticity) after approximately 75% into the cut, even for the stress-relieved components (HT). These early results ultimately discounted the application of HD. A description of how the CM was applied for the two orientations (obtaining σ_x and σ_y) by UoM on AB and HT samples is available in Appendix 8. A description of how the CM and layer-wise LXR results were obtained by CETIM is available in Appendices 9 and 10, respectively.

The following section describes results first for σ_x , σ_y and σ_z in the as-built (AB and AB2) components, and then the same for heat treated (HT and HT2). This is followed by the CM results obtained: the comparison between the distribution of σ_y in AB versus AB2, followed by σ_x and σ_y for AB and HT.

b) Results and cross-comparison of techniques

The residual stresses in LPBF components in the as-built condition are typified by high tensile stresses at the periphery, balanced by compressive stresses at the centre (Ahmad et al. 2018, Phan

et al. 2019). The highest residual stress is typically proximate to the last layer deposited. With the application of a stress-relief heat treatment, regions that have a high initial deviatoric stress state respond the most, with regions having a more balanced hydrostatic stress state responding the least. The deposition strategy and geometry were such that stresses in the x and y direction should be approximately balanced through the top of the arch, and with the ~2 mm thick ligament at the apex of the arch, versus the total 10 mm thick component, the centreline is expected to be in a state of plane stress in the x and y directions.

The general trend found for all measurements carried out on the as-built components reflects that described previously: a tensile stress near the surface ($z = 0$) in the x and y directions, decreasing towards compression at the apex of the arch ($z = 2$). This is shown in Figure 13 and Figure 14. The stresses in the x and y direction are approximately equal in terms of magnitudes and their positions along the ligament when comparing results from similar techniques. That is, the results from the layer-removal LXR technique show approximately the same profile between x and y, as do those from SXR and ND. ND results show that there is little difference between the ArcelorMittal and Volum-e components, except for in the last 200-300 μm of the ligament. This is likely due to a difference in the heat source shape employed by the two different fabricators.

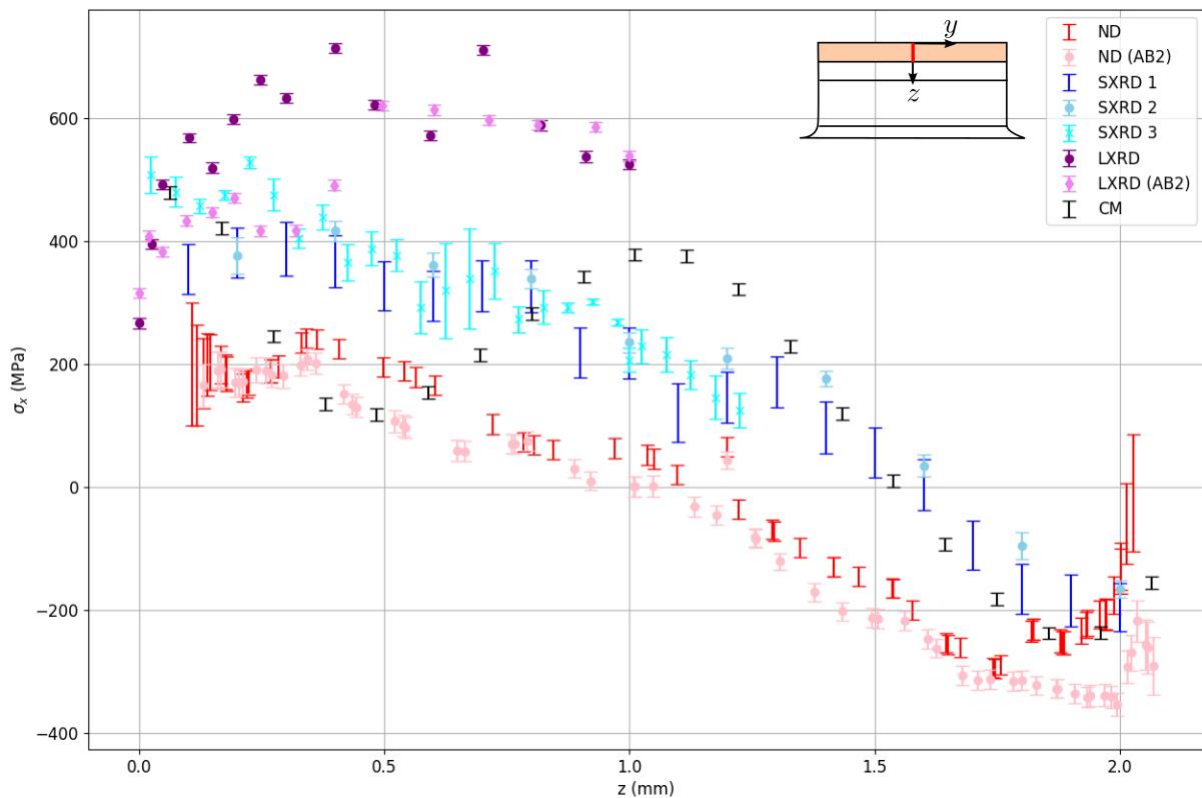


Figure 13 - Results for as-built components across methods showing stresses acting in the x direction for ArcelorMittal's component, with ND and layer-removal LXR applied to that of Volum-e (AB2) along the line shown inset.

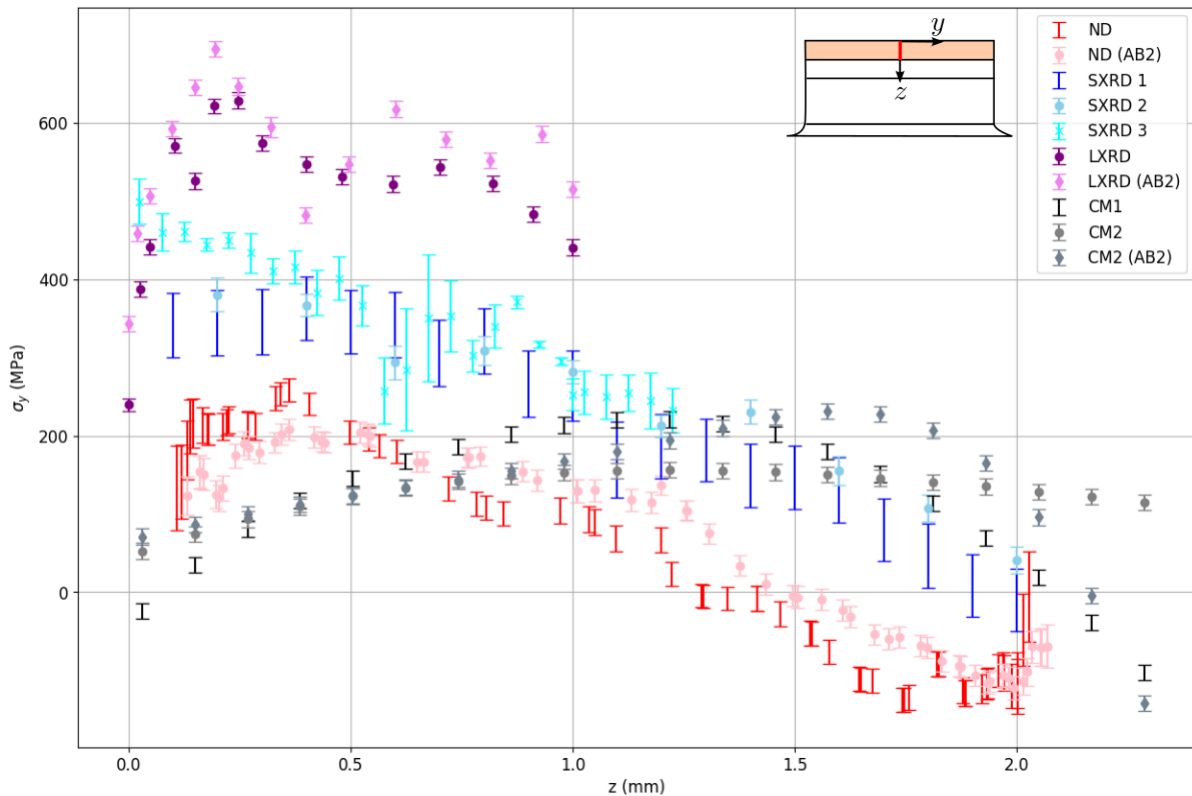


Figure 14 - Results for as-built components across methods showing stresses acting in the y direction for ArcelorMittal's component, with ND and layer-removal LXR and CM applied to that of Volum-e (AB2) along the line shown inset.

Different techniques returned different stress magnitudes in the x and y direction. Starting from the top of the ligament at $z = 0$, there is agreement with LXR and SXR techniques within the first 100-200 μm , followed by extremely high tensile stresses further into the component. This is likely due to plastic deformation occurring as material was removed during the LXR measurement. SXR results overall show agreement with each other, with the exception of SXR3 with SXR1 and SXR2 measurements near the surface from $z = 0$ to approximately $z = 0.5$ mm. This may be due to the powder d_0 reference value employed, as opposed to the comb employed for the other two SXR measurements. This difference in the stress-free reference component employed for measurement is much more appreciable for ND. While stresses in the x and y for ND are approximately 200 MPa lower, they still show the same trend being more tensile at the surface, tending towards compression at the apex of the arch, at similar rates to that shown by the SXR measurements.

The direction with the fewest results available is that for stresses acting in z for the as-built component, shown in Figure 15. Here, it can be seen that SXR techniques demonstrate the plane stress state that is expected (e.g. $\sigma_z \approx 0$), particularly near-surface; the ND results show a net compressive state through the thickness of the ligament. As expected stress state should be close to being plane stress and unprocessed powder should return a lower reference stress than a stress relieved comb, this is clear demonstration of the differences in inferred stresses obtained with different d_0 values.

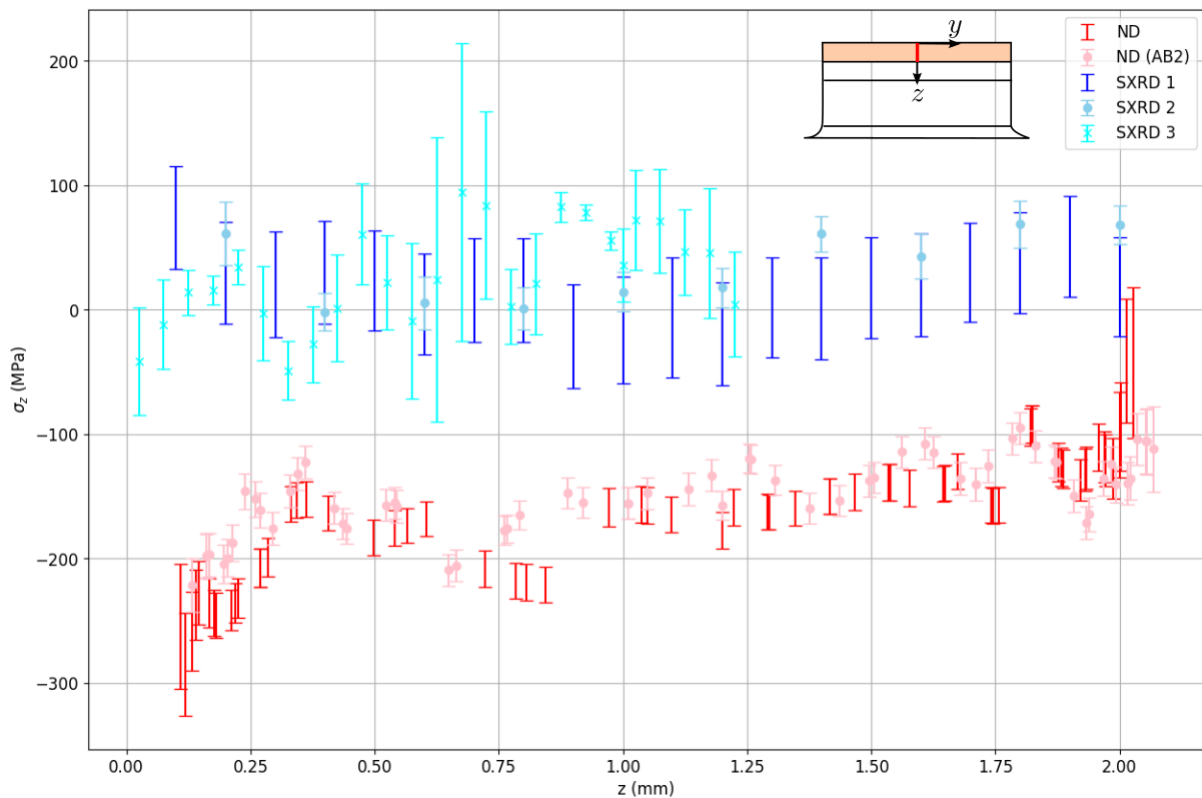


Figure 15 - Results for as-built components across methods showing stresses acting in the z direction for ArcelorMittal's component, with ND available for that of Volum-e (AB2) along the line shown inset.

For the HT samples, the same trends observed as those as-built can be seen between techniques as shown in Figure 16 to Figure 18 for the stresses acting in x, y and z, respectively. All techniques show that the peak tensile stress has been reduced by approximately 200 MPa, which is most apparent at the top surface of the part. The layer removal LXR measurements still show the highest stresses, for the same reasons as described previously. Further observations for the heat-treated results show that the regions with the most strongly reduced stresses are near surface and at the apex of the arch. While stresses acting in the x and y were approximately balanced in the as-built condition, there is a subtle difference of approximately 100 MPa at the apex of the arch between x and y, with the y direction showing higher compression than x. This is surmised to be due to the level of constraint being higher in the y direction, as there is more material in this orientation overall as opposed to x which spans the arch. This discrepancy between x and y directions is balanced by a slightly compressive stress acting through thickness of the ligament along the z.

The VM stress (Figure 19) highlights the d_0 discrepancies. Here, the VM stress has been calculated assuming that there are no shear stresses present, that is there is a balanced biaxial stress state the location considered. There is a remarkably good agreement between the results of different LRI techniques when considered in this manner. This suggests that a good portion of the reasons for differences in absolute results comes from an incorrect determination of the stress-free reference value d_0 . Thus, the present results confirm once more the importance of an appropriate stress-free reference.

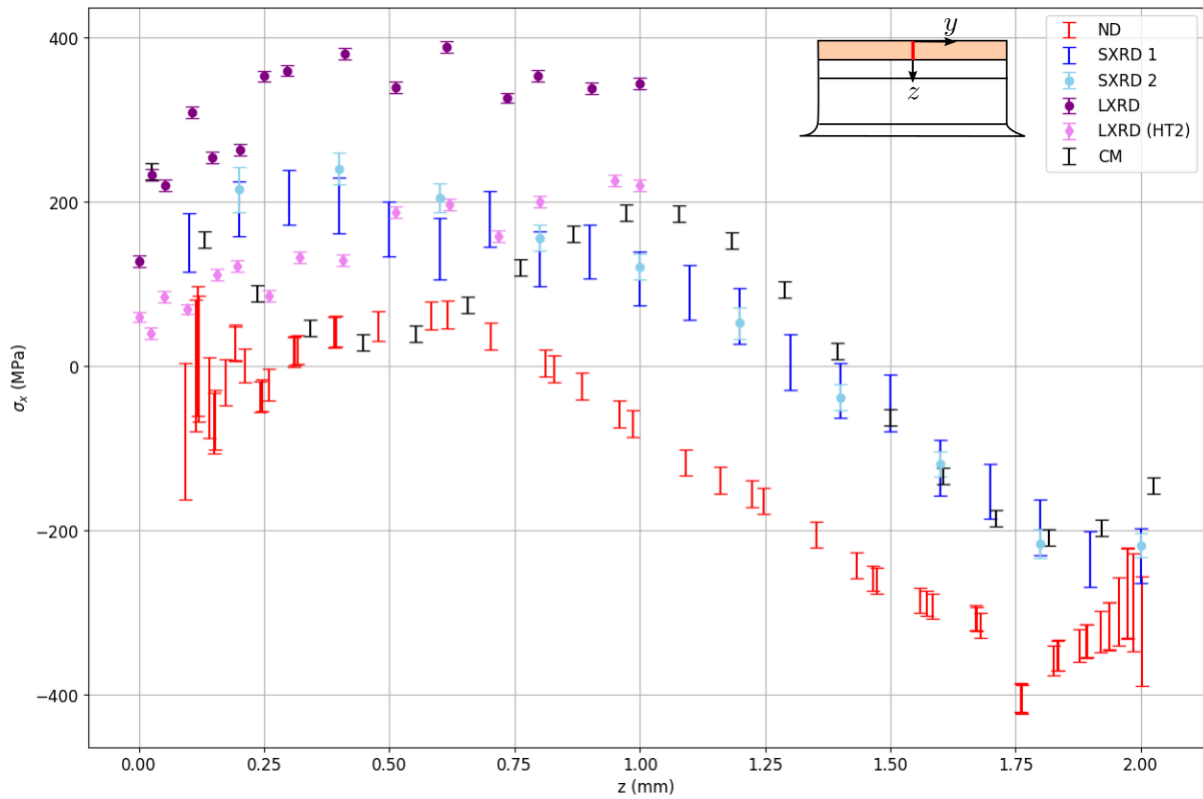


Figure 16 - Heat treated results for ArcelorMittal's component for stresses acting in the x direction. Layer removal LXR results for the component from Volum-e (HT2) in the same condition also shown along the line shown inset.

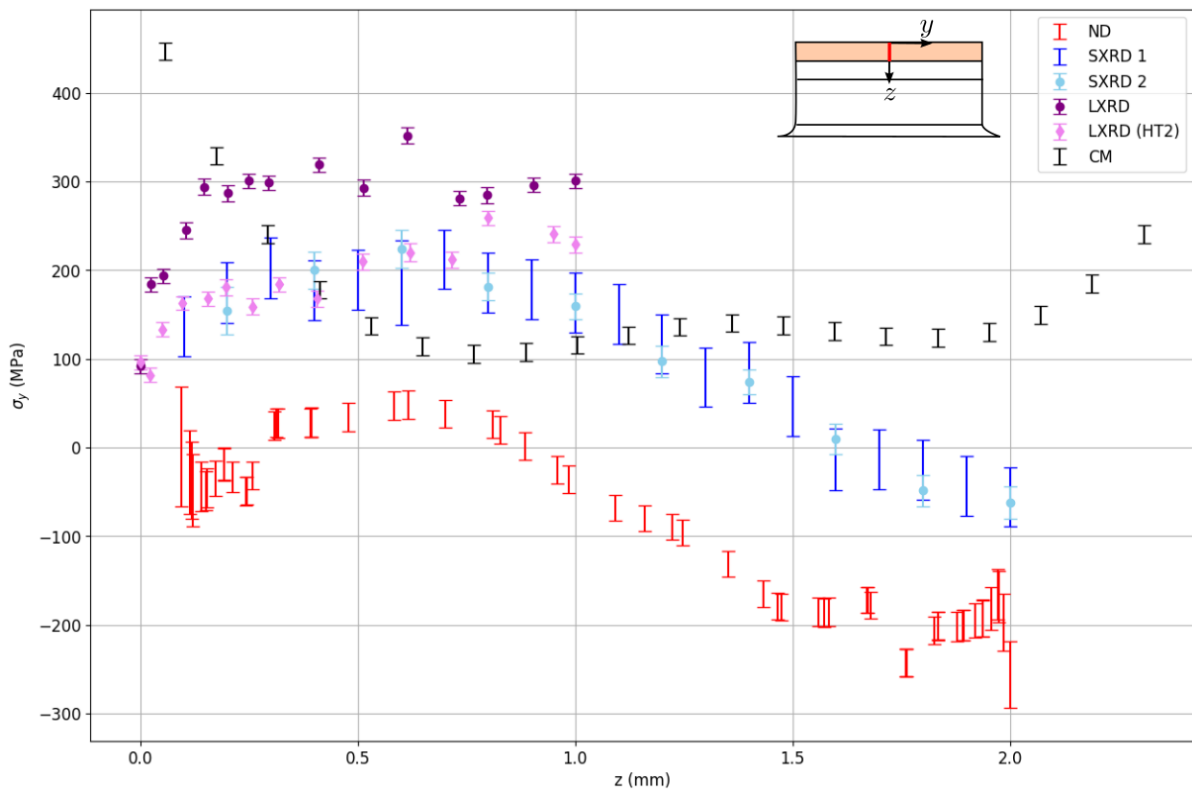


Figure 17 - Heat treated results for ArcelorMittal's component for stresses acting in the y direction. Layer removal LXR results for the component from Volum-e (HT2) in the same condition also shown along the line shown inset.

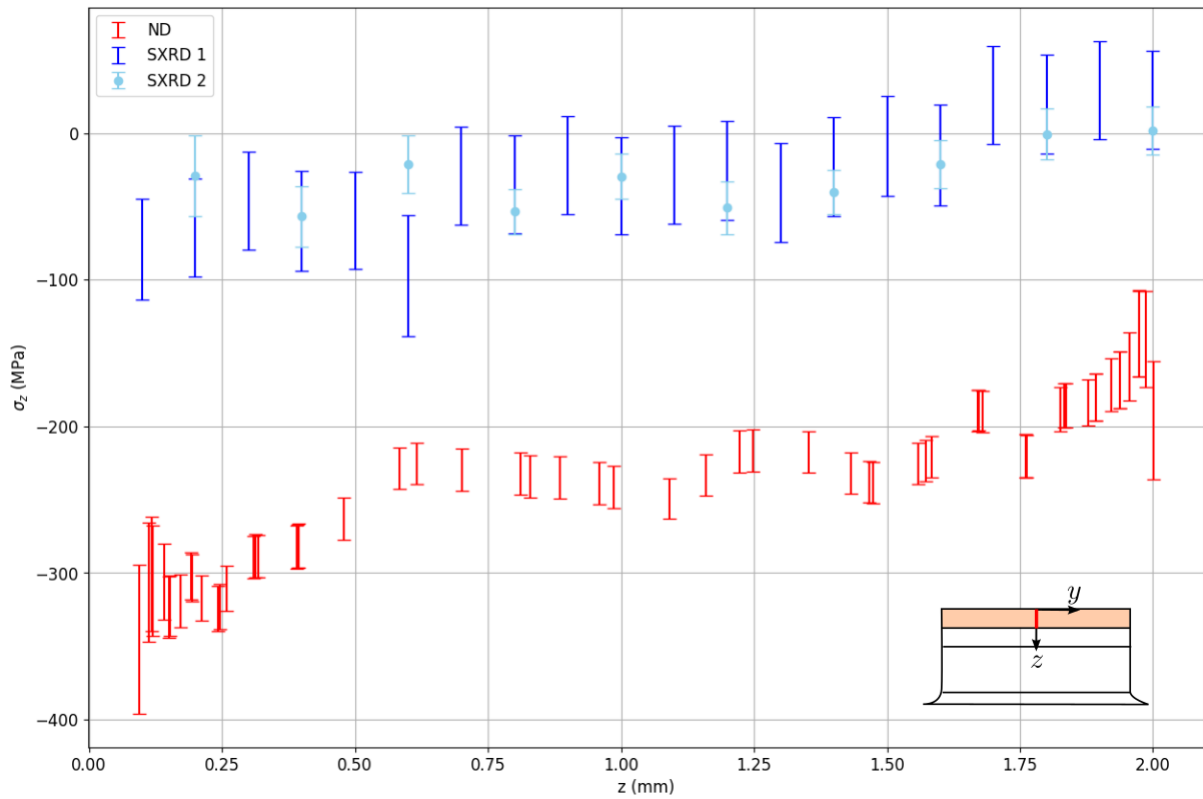


Figure 18 - Heat treated results for ArcelorMittal's component for stresses acting in the z direction along the line shown inset.

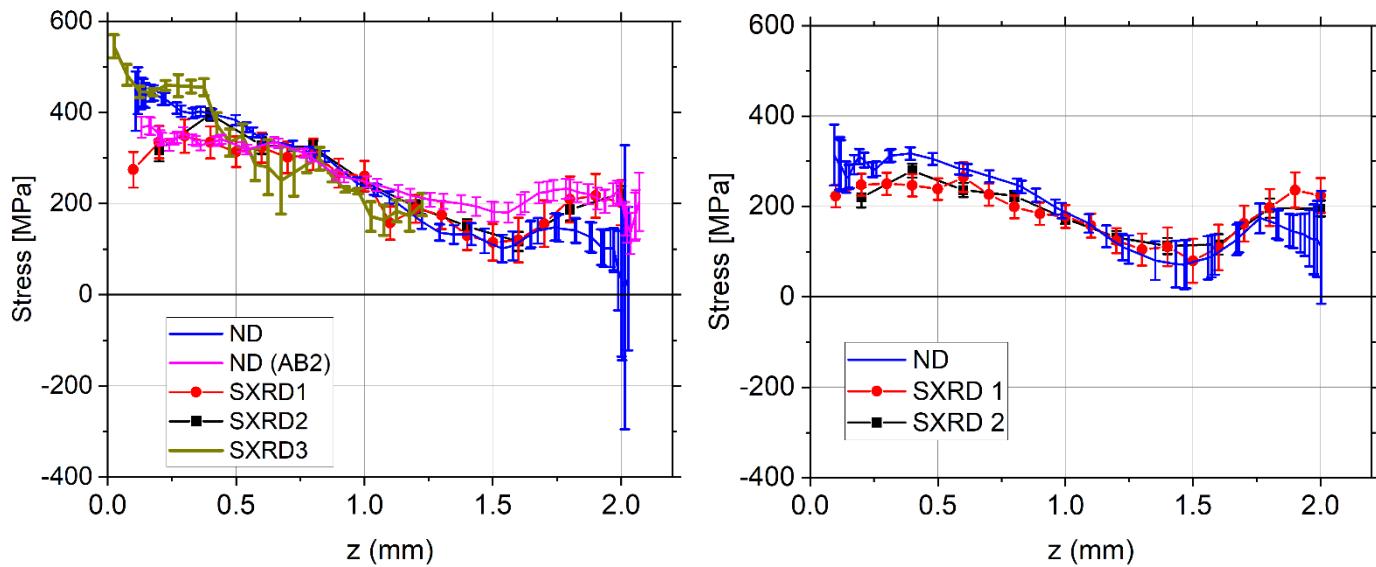


Figure 19 – Stresses calculated with the VM formula from ArcelorMittal and Volum-e samples in as-built (left) and HT (right) conditions for LRIs techniques.

CM results for both as-built and heat-treated samples return broadly the same stress magnitudes as the LRI techniques. For the as-built components, the stresses acting in the y direction measured by CM are in good agreement between components and practitioners. ArcelorMittal's as-built part measured by UoM and CETIM (Figure 20: CM, CM2) as well as the CETIM measurement on Volum-e's part (Figure 21: CM2 (AB)) are within 50 MPa of each other for $0.2 < z < 1.8$ mm. The CM results are in reasonable agreement with LRI measurements in the lower half of the ligament, where the stress tends towards compression for the as-built stresses acting in the y direction. Elsewhere the CM results do not necessarily reflect those obtained by LRI measurements, with magnitudes fluctuating between those found for ND and SXR. The regions with the greatest discrepancy between CM results and LRI are mostly near surface; both at the top of the specimen and proximate to the apex of the arch.

The reason for this discrepancy of CM results versus LRI measurements lies in the challenges that this specific component poses to the CM technique. The CM is best suited to regular, rectangular low ductility components with residual stresses much lower than the yield point in magnitude, with a long wavelength variation. Departures from these ideal circumstances will affect the practice and applicability. This can be seen in the subsequent contour plots. Figure 20 shows the application of CM by CETIM to ArcelorMittal's as-built part, as well as that for Volum-e in the same condition. The ND results shown in Figure 14 demonstrate that the stress profiles in the ligament should be near identical, tending from tension at the top of the component to compression at the apex of the arch. The CM results return roughly the same 250 MPa tensile stress everywhere in this region, which is at odds with ND.

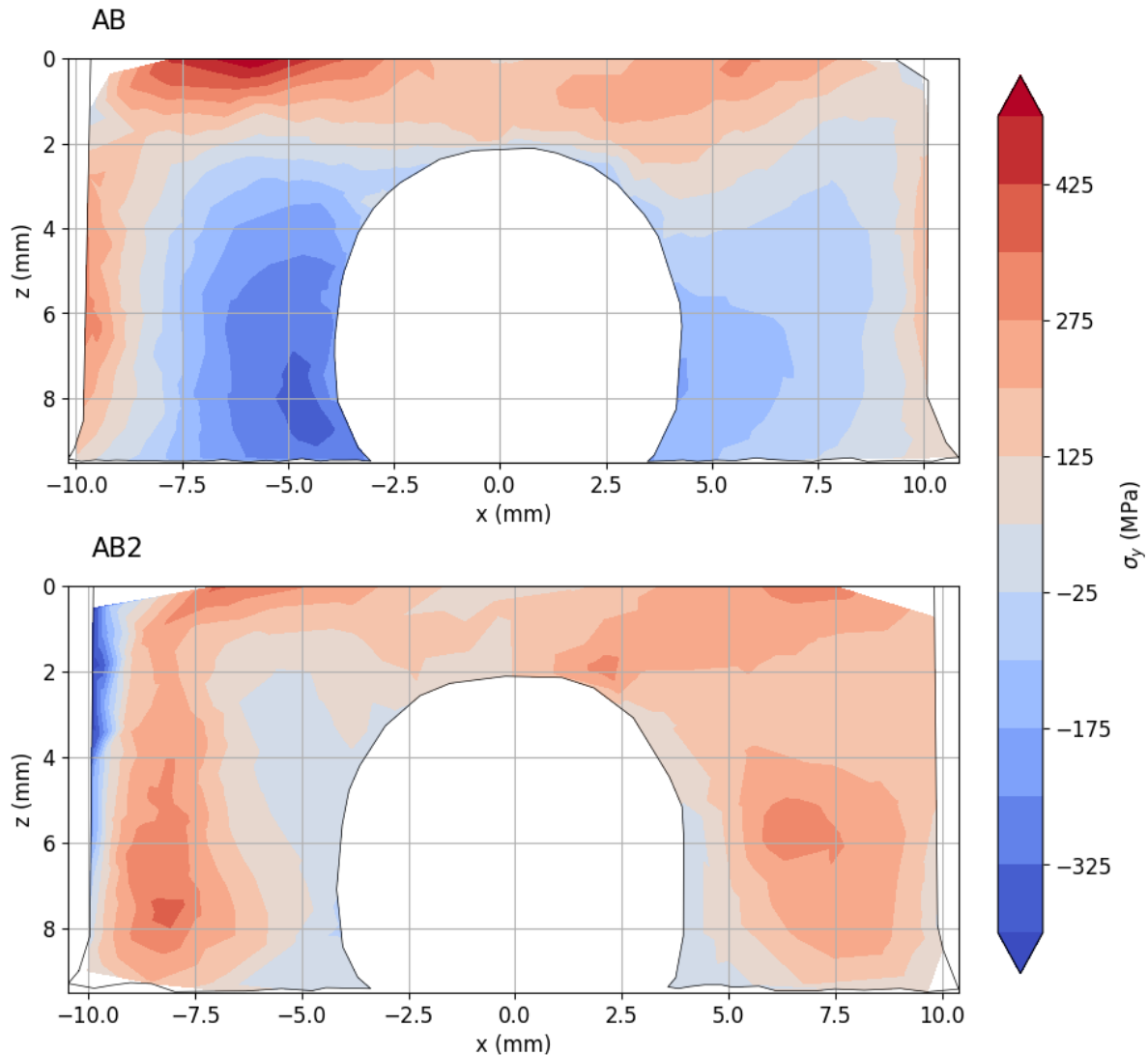


Figure 20 - CM results comparing Arcelor Mittal's as-built component (AB - top) to that produced by Volum-e (AB2 - bottom) for stresses acting in the y direction.

The root cause for this discrepancy lies in the very high residual stresses imparted during manufacturing, which in turn affect the cutting step. During cutting, residual stress redistributes ahead of the EDM wire, causing work hardening which resolves as an inelastic stress relief (Prime, 2013). This is why the left-hand side of the contour plots of stress in Figure 20 show higher magnitudes than the right, even though it would be expected to be symmetric in accordance with the sample shape and processing history. The two results shown in Figure 20 were obtained under varying degrees of restraint during cutting, giving rise to i) the lack of symmetry shown in the results and ii) differences in localised compression and tension in each leg.

This effect of cutting induced plasticity was also found in the x direction as well. Figure 21 shows the distribution of stress acting in the x direction along the ligament for both the as-built and heat treated parts supplied by ArcelorMittal. It can be clearly seen that at $y = -5$ mm in the AB (-7 mm for HT), cutting induced plasticity became important, leading to inelastic strain relief. Up to that point, the trend is roughly in agreement with the results obtained by LRIs (tensile at the surface, compressive at the apex). However, due to the nature of the CM, a singular surface needs to be

fitted to the entire region. Because of the requirement to balance stress over the whole surface, surface artefacts from cutting induced plasticity will still effect regions to be assessed elsewhere.

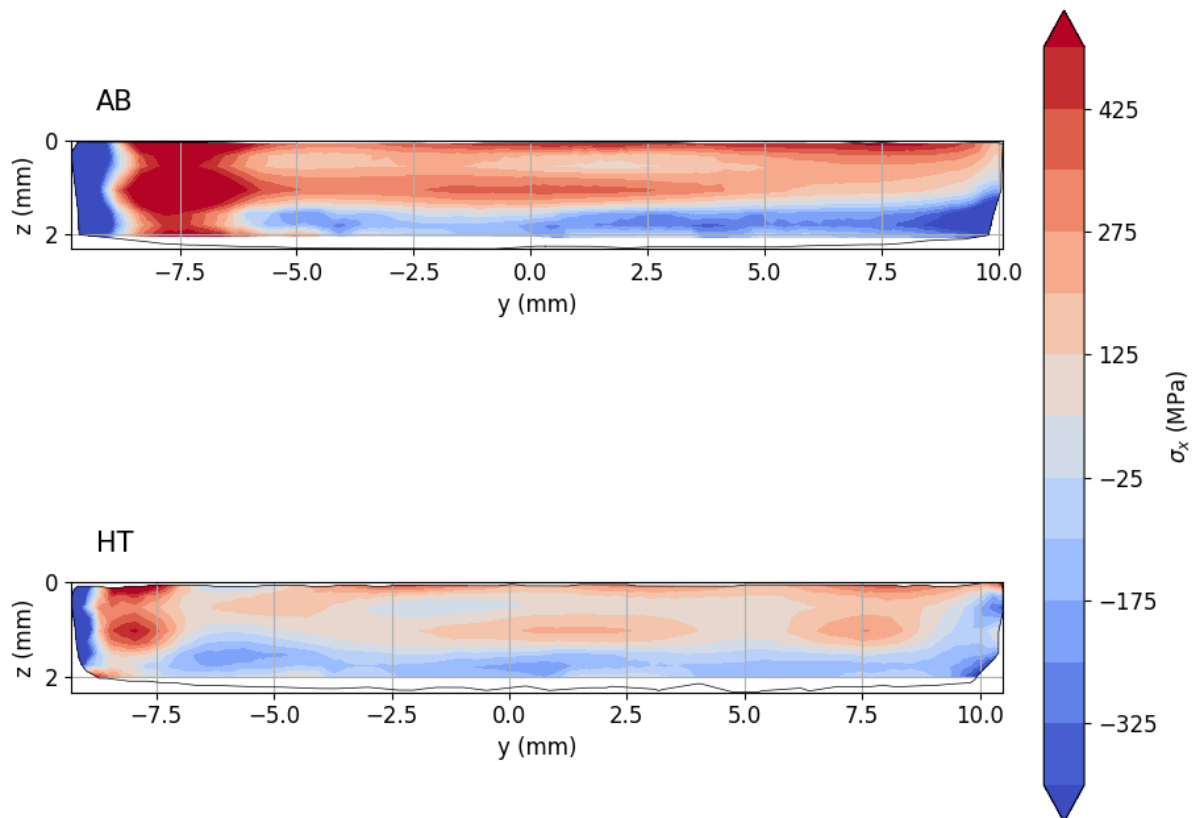


Figure 21 - CM results comparing the residual stresses in the x direction for ArcelorMittal's as-built (AB) and heat-treated (HT) AM arches.

The effects of heat treatment can clearly be observed in terms of the stress magnitudes being decreased – both in absolute terms (*i.e.* peak stresses returned by CM) as well as the location and magnitude of cutting induced plasticity. While the heat treated part still contained enough residual stress to induce plasticity during cutting, it was significantly diminished as compared to the as-built. This is also apparent for CM results for stresses acting in the y direction for both AB and HT, as shown in Figure 22. While cutting-induced plasticity is apparent on the left leg, results returned for the right leg show a decrease overall in peak stresses, as well as a redistribution.

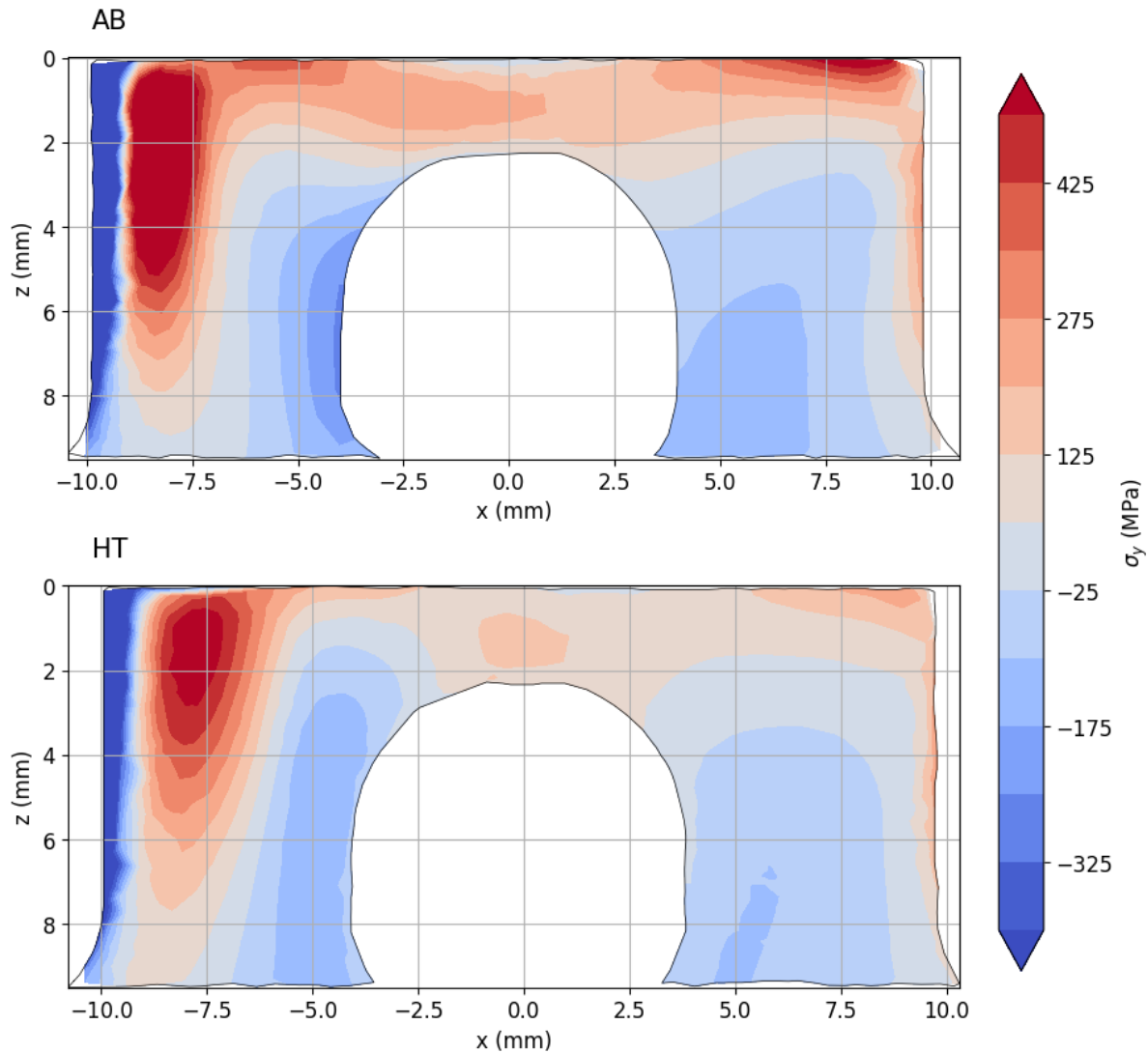


Figure 22 - CM results comparing ArcelorMittal's as-built (AB) component versus the same after heat treatment (HT) for stresses acting in the x direction.

c) Summary

Two different variants of LPBF 316L stainless steel benchmark arch samples were measured with ND, SXRD, layer-wise LXR, and CM. These were the as-built variant arches as well as heat-treated from two suppliers. It was found that there was little difference in distribution and magnitude of residual stress between the arches provided by different suppliers. Differences in stress magnitude between LRI diffraction techniques can be attributed to differences in stress-free reference, as the trends observed for all normal stresses, both as-built and heat-treated were very similar. For the lab based techniques, complications arose due to the high level of residual stress that remained in the part even after heat treatment. This level of residual stress along with the ductile nature of stainless steel led to issues both with the LXR technique reporting erroneous stresses farther away from the outside surface, while the CM did not identify the same distribution as seen with the diffraction techniques. All techniques confirmed that the peak tensile residual orthogonal stresses (σ_x and σ_y) were decreased by heat treatment by approximately 200 MPa for the region under consideration.

4.3 Inconel GTAW three pass welded plates

The Network on Neutron Techniques Standardization for Structural Integrity Task Group 6 (TG6) sample comprises a nickel-based alloy plate (Alloy 600) with a 3-pass slot weld made using an automated gas tungsten inert gas weld (GTAW/TIG) with a compatible, nickel-based Alloy 82 filler material [Akrivos et al, 2020]. Several plates from the same batch were used for destructive and non-destructive testing. Due to grain size and texture, no LXRD measurement have been made. The Network also attempted to perform CM measurements prior to EASI-STRESS and found that the stress levels immediate to the weld location resulted in inelastic strain relief, leading to intractable results. Therefore, only LRI procedures were used for determining residual stresses proximate to the weld location. While there have been ND measurements carried out, SXR measurements have not. The EASI-STRESS consortium therefore has included the A5 plate used previously for ND measurements with SXR. The component and coordinate system is shown in Figure 23.

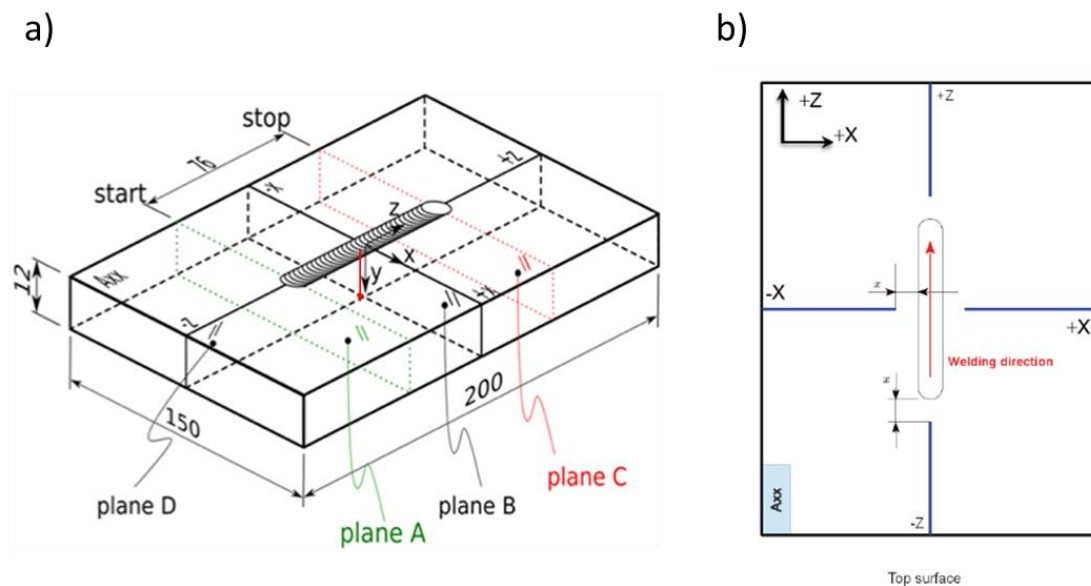


Figure 23 - a) TG6 schematic showing relevant planes and lines relative to manufacturing inputs. b) top view of component showing welding direction and coordinate system.

A measurement campaign at the ESRF has concluded, resulting in diffraction measurements made on the component itself, and relevant stress-free samples. A total of 121 points have been measured in three directions. This total comprises 30 discrete locations corresponding to where heterogeneity of microstructure is highest (pins extracted from different weld passes), which will be correlated against the remaining measurement positions within the plate. This analysis work is currently ongoing. The results obtained from this measurement campaign will be validated against both process model predictions as well as the existing ND measurements previously conducted. Effort continues as a modified version of this benchmark sample is currently being investigated within WP5.

4.4 Cast and quenched aluminium wedges

Three variants of these components were provided for measurement. The first of which was of the as-cast (AC) form, whereby the component was cast and left to cool to room temperature. The second was in the T4 condition, whereby the component was cast, solutionised (i.e. brought to an

elevated temperature and then water quenched) and left to naturally age (i.e. a process by which precipitates evolve under ambient conditions). The third variant was supplied in the T6 condition, which was identical to T4 in processing, however after solutionising it was artificially aged, causing the precipitates to grow and coarsen at an elevated temperature. The nominal geometry of the component is provided in Figure 24.

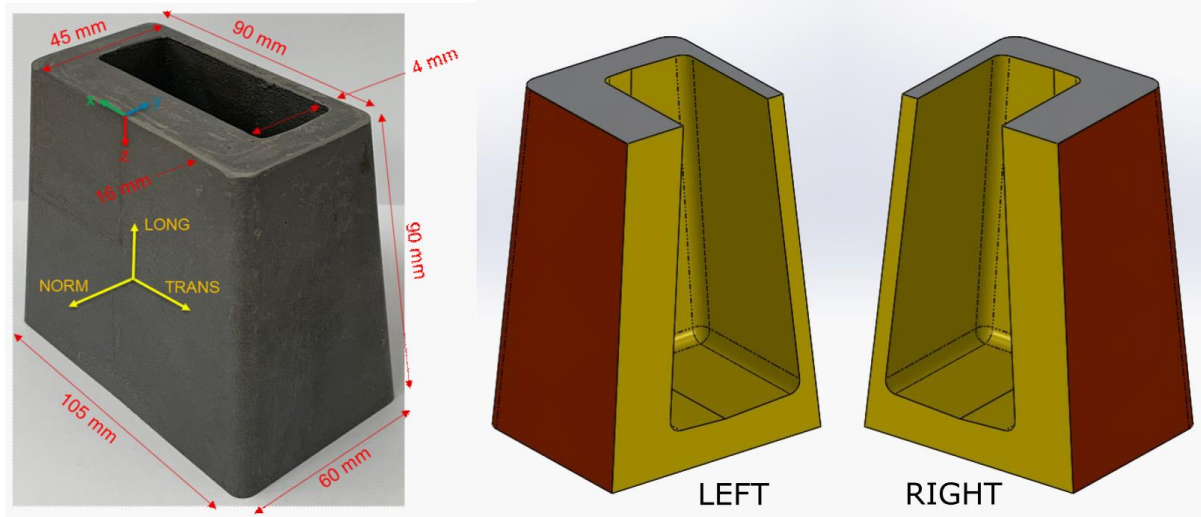


Figure 24 - Cast and water quenched wedges. Three tempers conforming to the geometry described were considered: as-cast (AC), solutionised and naturally aged (T4) and solutionised and artificially aged (T6).

Due to the microstructural inhomogeneity and dendritic microstructure, X-ray diffraction techniques (SXRD, LXRD) were deemed to not be suitable. Therefore, the techniques applied were ND, CM and HD. Combinations of CM and HD were also applied to provide a direct comparison with ND in select locations. Due to the limitations of the techniques themselves, a direct comparison of the results for all components in all directions could not be undertaken, but comparisons between the results obtained for each of the measurements by participants has been produced. Where necessary, manipulation of local measurement datums to match those in Figure 24 were performed according to the methods described in Section 2. A summary of the measurements carried out and the respective partners involved is provided in Table 6.

Table 6 - Techniques applied by participants to the round robin in order to assess residual stresses in the cast and quenched aluminium wedges

Component	Technique/application	Participant
AC	Contour method, midplane (σ_x , partial σ_y and σ_z)	UoM
	Hole drilling on contour cut surfaces (partial σ_y and σ_z)	UoM/UBC*
	Hole drilling, surface location (σ_x)	CETIM
T4	Contour method, midplane (σ_x , partial σ_y and σ_z)	UoM
	Hole drilling on contour cut surfaces (partial σ_y and σ_z)	UoM/UBC*
	Hole drilling, surface location (σ_x)	CETIM
T6	Contour method, midplane (σ_x , partial σ_y and σ_z)	UoM
	Hole drilling on contour cut surfaces (partial σ_y and σ_z)	UoM/UBC*
	Hole drilling, surface location (partial σ_y and σ_z)	CETIM
	Neutron diffraction, 2 off line scans midplane (σ_x , σ_y and σ_z)	ILL/PSI**

*Carried out by Gary Schajer and Luc To at the University of British Columbia under the remit of UoM. **Performed at POLDI at PSI under the remit of ILL

a) Measurement overview

Common to all components, the complete σ_x stress component was captured at the midplane of all samples by the contour method (CM). As detailed in deliverable 2.2, the contour method provides a complete component orthogonal to a cutting plane, and those normal stresses relieved by the cut. Another lab-based technique that operates near-surface can then be applied to either of the resultant cut surfaces to obtain the remaining quantity of normal stresses acting in-plane. This approach was taken such that lab techniques could be employed to directly compare all normal stresses to ND, whereby an electronic speckle pattern interferometry (ESPI) hole drilling technique was employed directly on the contour cut surfaces to a depth of 1 mm, with analysis/results obtained every 0.1 mm (see details in Appendix 11). An ESPI technique is necessary in order to increase the number of measurement locations as possible for comparison to ND (more details in Appendix 12). The stress values at a depth of 0.3 mm were added to the contour method result (CM+HD), as this was the point where the recast layer from cutting no longer affected the stress value(s).

While hole drilling can provide three in-plane stress components simultaneously near surface, the hole drilling results returned only one component that could be directly compared to any other of the techniques applied, which was the CM. The depth resolved stresses obtained with a strain-gauge based technique near the surface were directly compared to the appropriate component/location ascertained by the contour method.

Only one specimen was measured via a diffraction technique. Two discrete lines through the component were measured, with line 1 able to be directly compared to CM (σ_x), and CM+HD (σ_y and σ_z). Line 2 only had comparable results for CM (σ_x) due to the point resolution possible with HD.

b) Results and cross-comparison of techniques

The following figures contain all results from the campaign described above, in the order of AC, T4 and finally T6 parts, shown how stresses appear on the left side of the component (Figure 25).

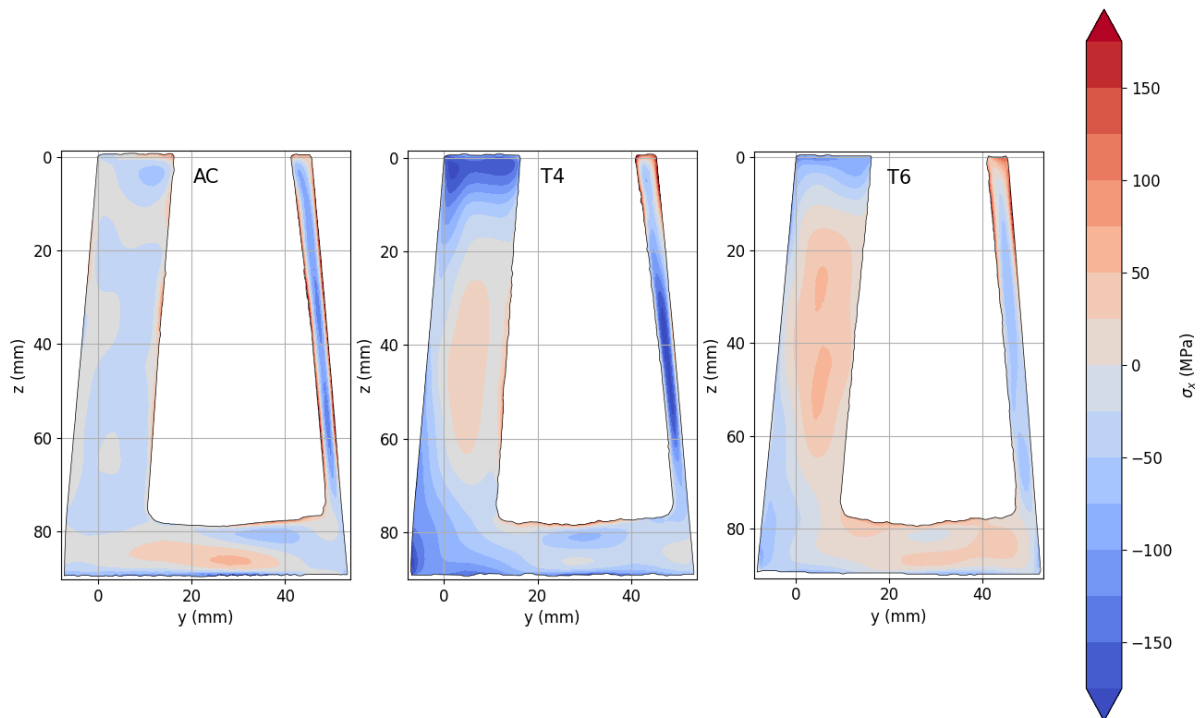


Figure 25 - Contour method (CM) results for σ_x for all three tempers AC, T4 and T6 cast wedges. These results have been employed subsequently for direct CM comparisons for σ_x .

The contour method results for σ_x on all tempers indicate that significant residual stresses only truly arise during the tempering process. The AC wedge shows that there are near-zero residual stresses throughout, with the thick wall demonstrating slightly compressive stress. For the tempered wedges, the stress distribution changes to being tensile at the centre, balanced by compressive stresses at the surface. This is typical of a component that has been quenched, where the thermal expansion and difference in temperature between inner and outer regions creates a stress gradient. The distribution between T4 and T6 is notably different, with T4 showing a more sharply defined gradient between tension and compression. This is due to a combination of stress relaxation and precipitation effects during ageing.

The other orthogonal stresses in the AC sample at locations which were subjected to ESPI hole drilling (Figure 26) are consistent with the results shown for σ_x . At the locations selected, these results indicate that the centre of the thick wall is in low level hydrostatic compression. For the standard hole drilling measurement on the surface of the component providing depth-resolved stresses for σ_x do not coincide with contour method results for approximately the first 0.25 mm (Figure 27). This is not unexpected; the contour method is recognised as being unreliable 1 mm from a free surface. The nature of near-edge fitting in the contour method, particularly for essentially a stress free sample, is what is attributed to the difference observed. However, beyond this, there is an excellent match between both methods.

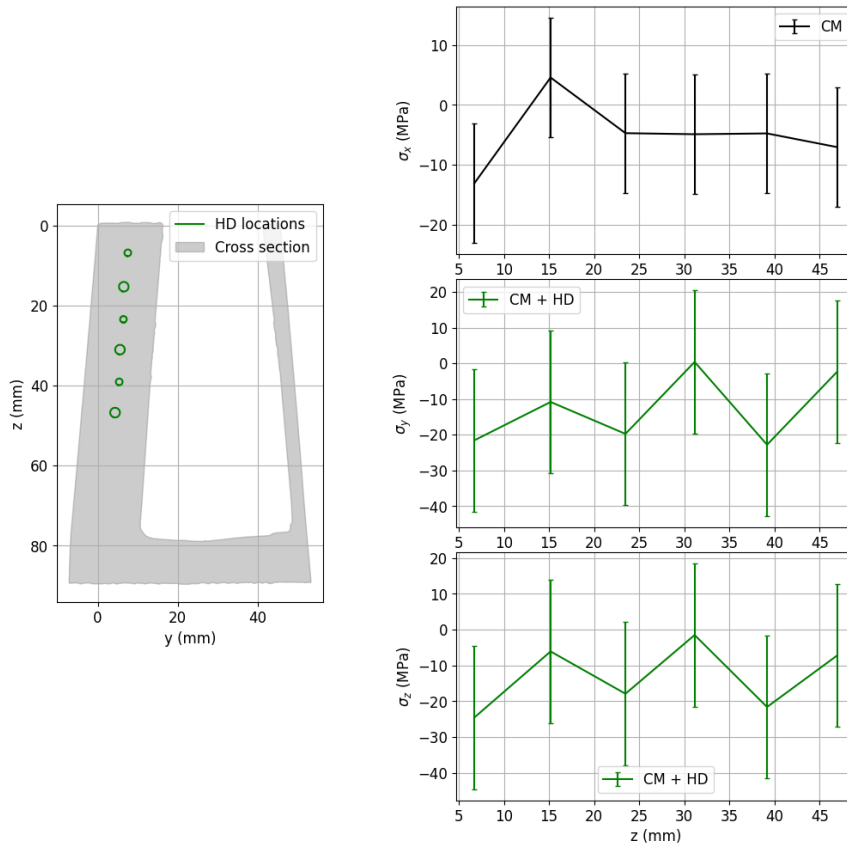


Figure 26 - As cast (AC) wedge results for three orthogonal stress components.

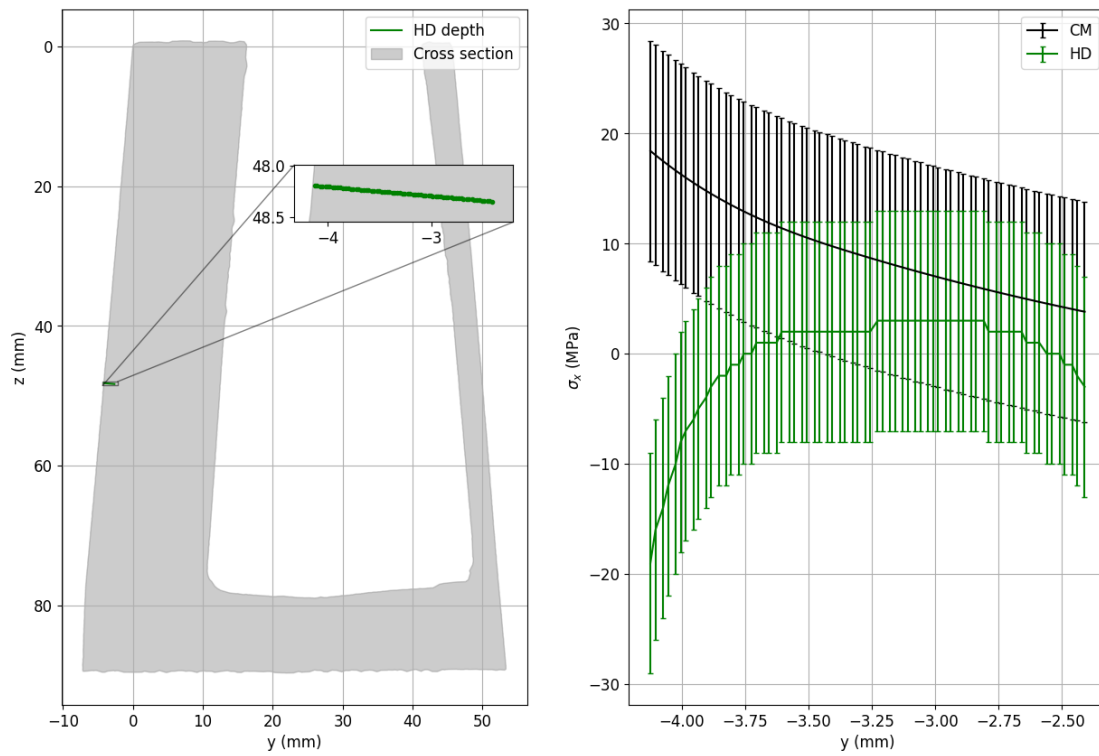


Figure 27 - Comparison between σ_x results obtained via hole drilling and contour method for the AC wedge

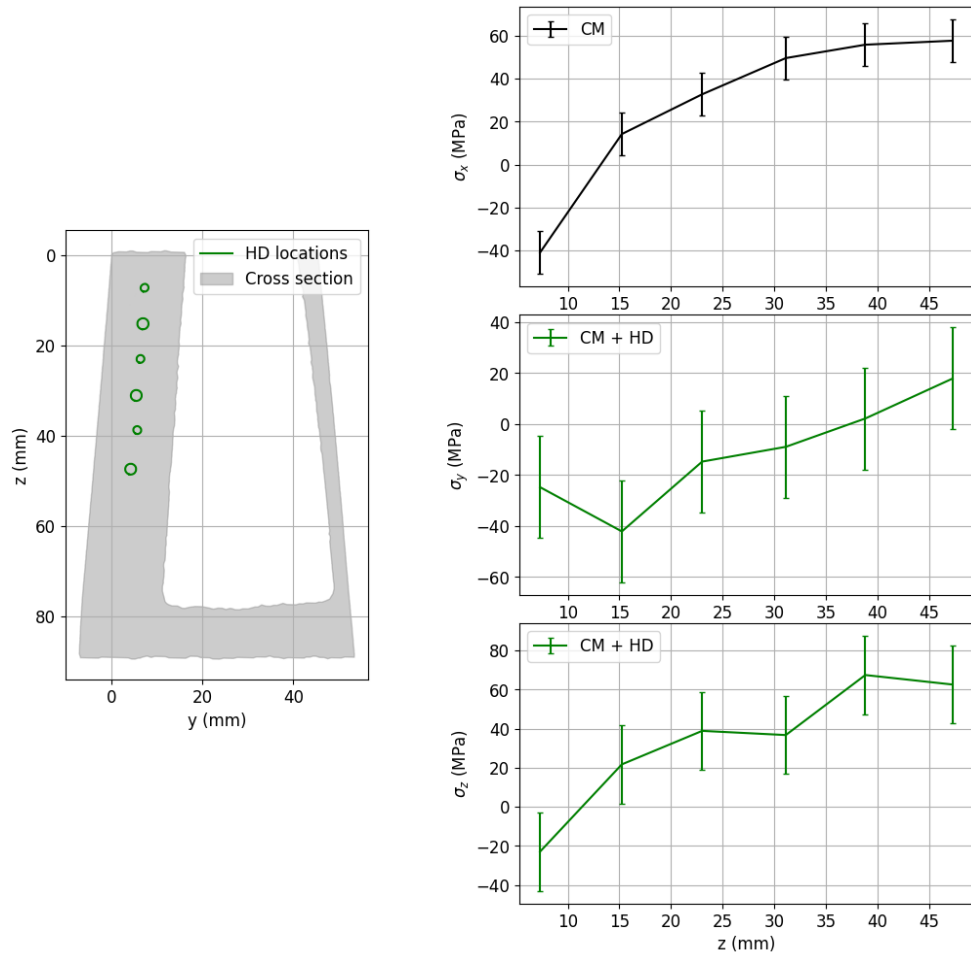


Figure 28 - T4 temper results for three main orthogonal stress components.

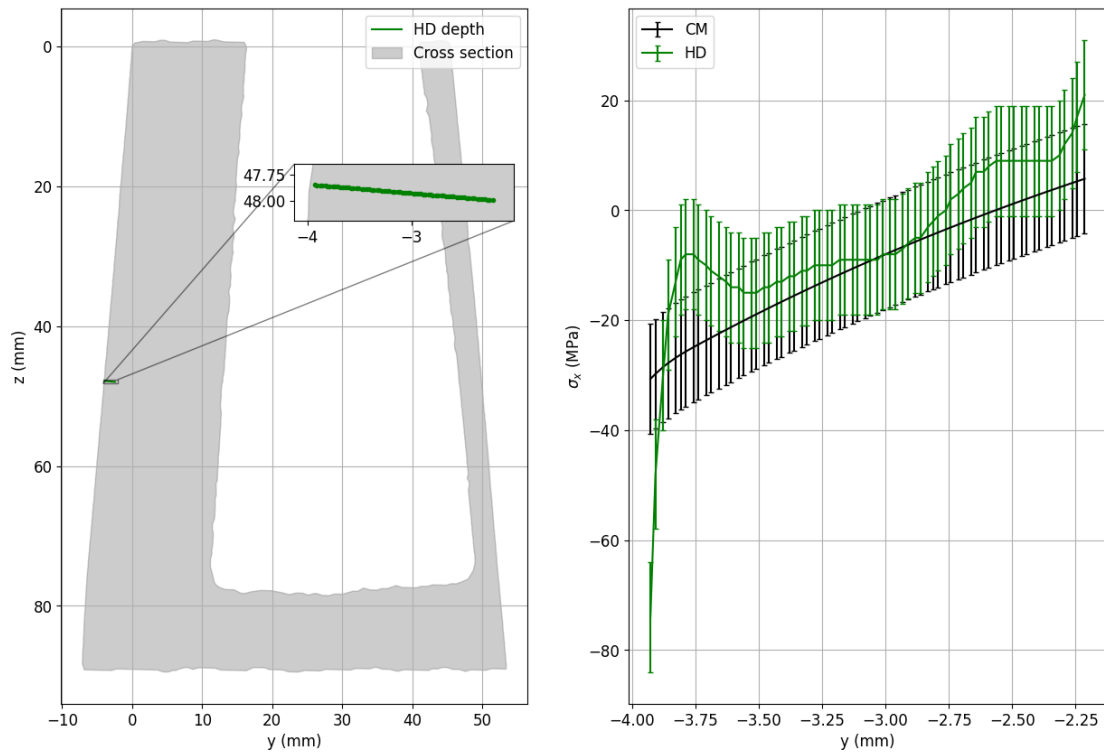


Figure 29 - Comparison between σ_x results obtained via hole drilling and contour method for the T4 wedge

Figure 28 shows the same results as those obtained for the AC wedge for the T4 temper. Here, similar trends are observed as for the overall CM results: moving along the thick wall from the top to bottom along the z axis, the stresses run from approximately 30 MPa in compression to 60 MPa in tension for both the σ_x and σ_z components, while σ_y is approximately half this range. This is also unsurprising, as during quenching the x and z directions are those that have the highest degree of constraint, which leads to a low level deviatoric stress state at the centre of the wall.

Figure 29 shows the results of standard hole drilling versus CM for σ_x in the T4 wedge; again, there is a disparity between techniques for the first 0.25 mm, however with better agreement deeper into the part. This reinforces the validity of both techniques.

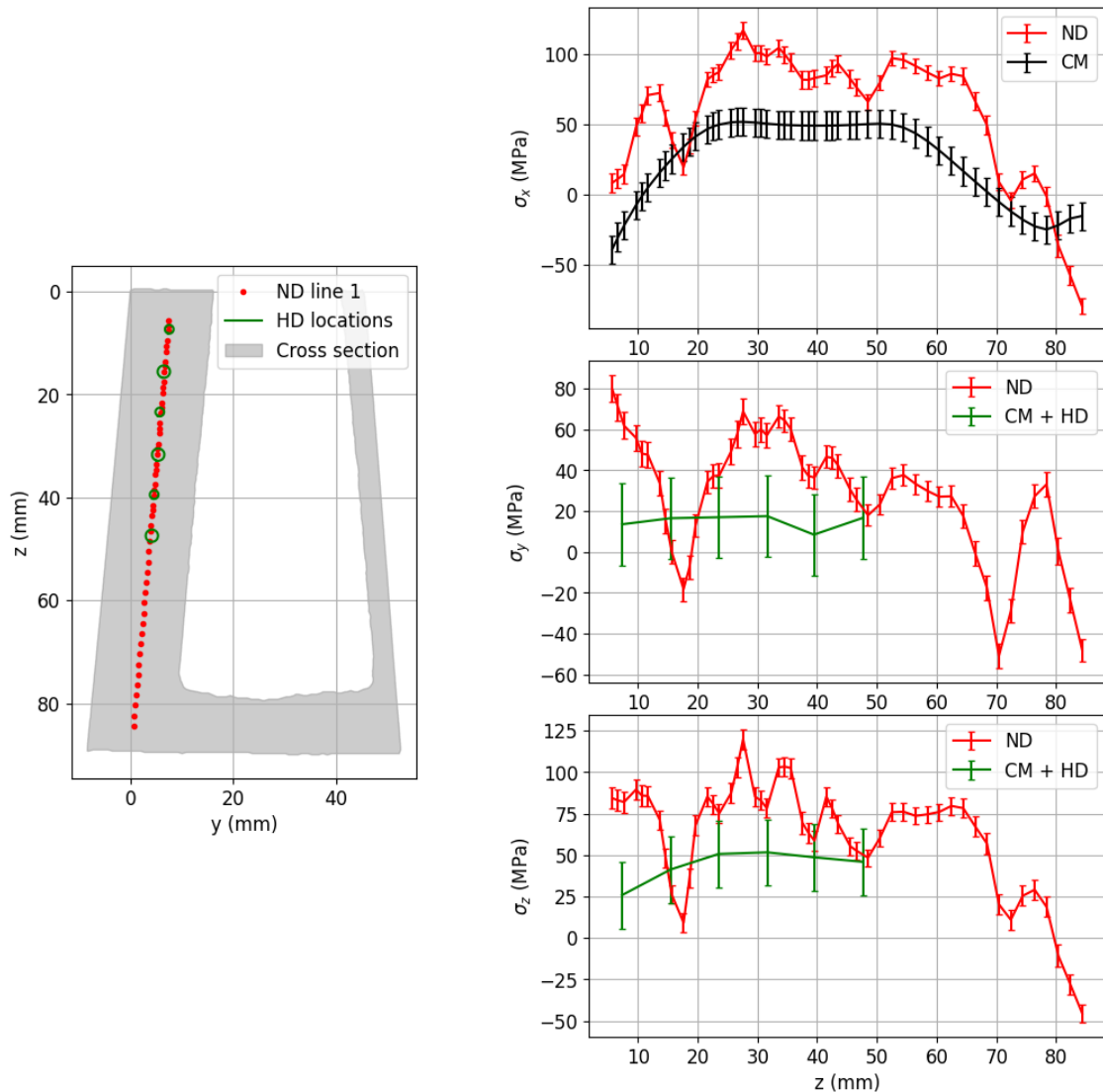


Figure 30 - T6 temper results for three main orthogonal stress components comparing the results obtained via ND as well as the CM + HD technique.

Figure 30 shows the results obtained from CM, CM and ESPI hole drilling combined (CM+HD) as well as ND for the T6 component. The biggest difference observed in comparing the normal stresses for CM+HD as to those obtained for T4 is that σ_x is the highest component of all three, as compared to T4 where σ_x and σ_z were approximately balanced. Between ND and CM+HD, the stresses obtained by ND are systematically higher than those found by the mechanical relief techniques, with sharp changes in distribution at 20 and 70 mm along the z axis for all three normal stresses. There is no

processing-related rationale for these sudden changes, and the reason for the differences is ascribed to the choice of a static d_0 value obtained from potentially heavily deformed chips/swarf. There is likely a change in microstructure at those locations which is probably the reason for the sudden changes, i.e. a dendritic structure changing from columnar to equiaxed, or a difference in phase distribution. The heavily deformed material used as a d_0 reference could also be the reason why the ND results show significantly higher stresses overall. Alternatively, cutting induced plasticity encountered during the CM cuts could be why stresses are less than those found by ND; however, this would only be expected if any of the RS components was closer to the yield point of the material.

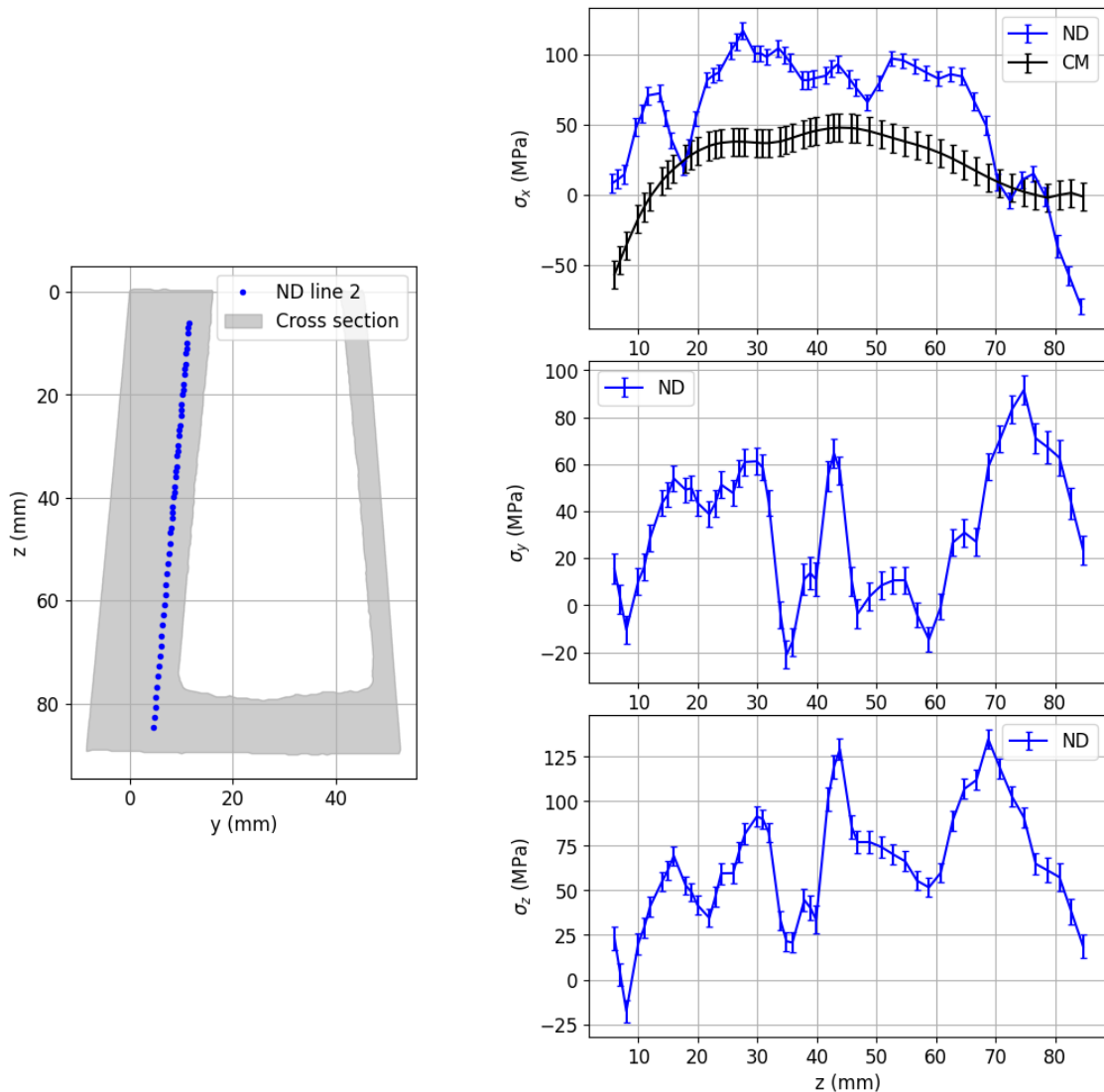


Figure 31 - T6 temper results for three main normal stress components comparing the results obtained via ND at a second location as well as the result of the single directly comparable stress component obtained by CM.

ND was also applied to another location immediately beside the location indicated in Figure 31. As ESPI hole drilling could not be carried out at this location, only the σ_x component obtained by CM can be directly compared. Again, there are large jumps in stress which cannot be immediately rationalised by processing induced effects.

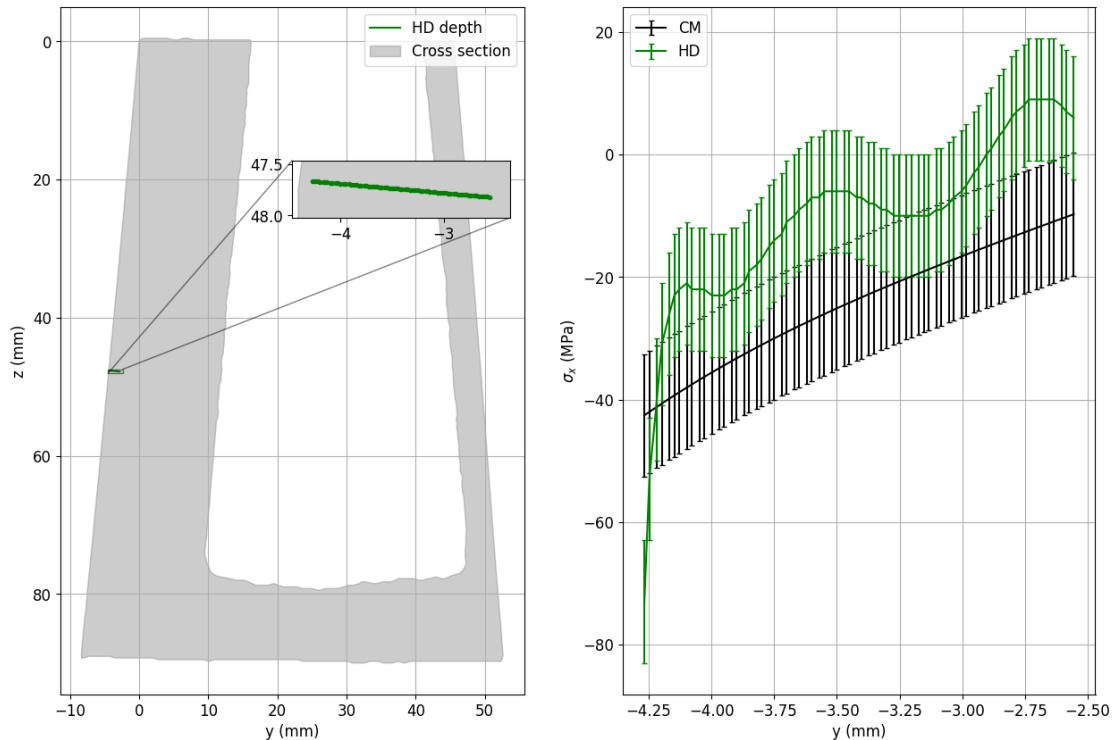


Figure 32 - Comparison between σ_x results obtained via hole drilling and contour method for the T6 component

Figure 32 shows the results of standard hole drilling versus CM for σ_x , on the T6 component. While agreement between these measurements 0.25 mm into the surface is not nearly as good as that obtained for T4, the trend is similar and is within a conservative range of error between the methods; this independent measurement also serves to validate the CM results over ND.

c) Summary

This component type has demonstrated the challenges associated with diffraction-based techniques as applied to coarse microstructures. While all mechanical techniques (CM, CM+HD, HD) applied report a consistent set of results: stress magnitudes are similar for both T4 and T6 components, whilst the distribution of these stresses is different. Neutron diffraction results indicate significantly higher residual stress than those obtained by mechanical techniques, but exhibit point to point variations that are unlikely in view of the processing history. Departures of the ND results from mechanical relief methods could be attributed to the lack of spatially distributed d_0 values, which is currently under investigation.

5. Summary and conclusions

This document reports the results of an inter-laboratory comparison of residual stress analysis using different samples and different techniques. Five different sample geometries and microstructures made out of four different materials using five different production techniques were selected for spanning a representative portion of the wide range of different cases that appear in industrial residual stress analysis. To this end, the aim was not involving as many labs as possible on a single sample type, but rather covering a typical range of cases.

From the work carried out in conducting this round-robin exercise, the following specific conclusions that can be drawn.

- Each of the techniques used (ND, SXR, LXR, HD, and CM) work well in specific and appropriate domains. The techniques can be regarded as complementary in terms of spatial resolution, penetration depth or absolute calibration capability.
- It immediately follows that the lab-based techniques may not be sufficient for solving a stress problem completely. LSI techniques should be used in addition.
- The capability of the diffraction techniques is limited in samples having large grain sizes as they e.g. in foundry metallic systems.
- While the CM can deliver stress maps of a single stress component over a complete cross section, caveats remain in terms of its applicability for all component types. CM remains best applied to regular, rectangular cross-sections, on materials with stresses significantly lower than the yield point. Like all strain-relief techniques, any inelastic residual stress relief that takes place during measurement can affect the final stress results.
- It was demonstrated that the proper selection of a stress-free reference for the diffraction techniques is of utmost importance. The ultimate solution for this is cutting a small piece or 'comb' out of the investigated material, close to the location investigated, in which macro-stresses can largely relax. This was done in the case of the additively manufactured arch and yielded the most reliable results. The raw metal powder is rarely a proper reference as its microstructure is normally completely different from that of the finished product.
- The other challenges connected with the diffraction techniques are connected to reporting all relevant metadata, positioning of the sample with respect to the gauge volume, and finding the proper diffraction elastic constants for the calculation of stresses from strains.

With the results presented, WP2 has shown that there is good agreement between the results of all techniques when defined quality standards are applied, e.g. in sample positioning. Thus, the efforts towards standardisation should be pursued and they will lead to further improvement of the reliability of the results.

6. References

Ahmad B., van der Veen, S.O., Fitzpatrick, M.E., Guo H. Residual stress evaluation in selective-laser-melting additively manufactured titanium (Ti-6Al-4V) and inconel 718 using the contour method and numerical simulation, Additive Manufacturing 2019. <https://doi.org/10.1016/j.addma.2018.06.002>

Akrivos V., Wimpory R.C., Hofmann M., Stewart B., Muransky O., Smith M.C., Bouchard J., Neutron diffraction measurements of weld residual stresses in three-pass slot weld (Alloy 600/82) and assessment of the measurement uncertainty, Journal of applied crystallography 53, pp 1181-1194 (2020)

Brightness, <https://brightness.esss.se/>

Hutchings et al., 2005, <https://doi.org/10.1201/9780203402818>

D'Elia, C.R. et al., 2022, <https://link.springer.com/article/10.1007/s11340-022-00849-3>

NF, NF EN 15305: 2009 Non-destructive testing – Test method for residual stress analysis by X-ray diffraction



NPL 2020, “Determination of residual stresses by X-ray diffraction”,
<https://www.npl.co.uk/gpgs/residual-stresses-xray-diffraction>

Phan, T.Q.; Strantz, M.; Hill, M.R.; Gnaupel-Herold, T.H.; Helgel, J.; D’Elia, C.R.; DeWald, A.T.; Clausen, B.; Pagan, C.P.; Ko, J.Y.P.; Brown, D.W.; Levine, L.E. Elastic Residual Strain and Stress Measurements and Corresponding Part Deflections of 3D Additive Manufacturing Builds of IN625 AM-Bench Artifacts Using Neutron Diffraction, Synchrotron X-Ray Diffraction, and Contour Method. Integrating Materials and Manufacturing Innovation, 2019. <https://doi.org/10.1007/s40192-019-00149-0>

Prime and DeWald, 2013, “The Contour Method” in Practical residual stress measurement methods; John Wiley & Sons, 2013.

Rickert, T., 2016, <https://www.sciencedirect.com/science/article/pii/S2212827116005400>

Schajer, G. S. Practical residual stress measurement methods; John Wiley & Sons, 2013.

Schajer and Whitehead, 2013, “Hole Drilling and Ring Coring” in Practical residual stress measurement methods; John Wiley & Sons, 2013.

Staron, P.; Fischer, T.; Eims, E.H.; Frömbgen, S.; Schell, N.; Daneshpour, S.; Martins, R. V.; Müller, M; Schreyer, A., 2013 “Depth-Resolved Residual Stress Analysis with Conical Slits for High-Energy X-Rays”, Materials Science Forum vol. 772 <https://doi.org/10.4028/www.scientific.net/MSF.772.3>

Stefanescu, D., et al. 2006, <https://link.springer.com/article/10.1007/s11340-006-7686-8>

Ramadhan, R. S.; Cabeza, S.; Pirling, T.; Kabra, S.; Hofmann, M.; Rebelo Kornmeier, J.; Venter, A. M.; Marais, D. Quantitative analysis and benchmarking of positional accuracies of neutron strain scanners. Nuclear Instruments and Methods in Physics Research Section A: Accelerators, Spectrometers, Detectors and Associated Equipment 2021

ISO, ISO 21432:2019 Non-destructive testing — Standard test method for determining residual stresses by neutron diffraction

Withers, P.J.; Preuss, M.; Steuwer, A.; Pang, J.W.L. Methods for obtaining the strain-free lattice parameter when using diffraction to determine residual stress. Journal of Applied Crystallography 2007. <https://doi.org/10.1107/S0021889807030269>

Withers, 2013, “Synchrotron X-ray Diffraction” in Practical residual stress measurement methods; John Wiley & Sons, 2013.



Appendices

Appendix 1 – Application of neutron diffraction to ferritic steel U-forms	44
Appendix 2 – Application of synchrotron diffraction to ferritic steel U-shapes	46
Appendix 3 – Application of contour method to U-bend ferritic shapes and preparation for LXRD	47
Appendix 4 – Application of contour method to U-bend ferritic shapes	49
Appendix 5 – Application of LXRD to cut U-bend ferritic shapes	52
Appendix 6 – Application of neutron diffraction to austenitic steel AM Arches	54
Appendix 7 – Application of synchrotron diffraction to the powder-derived stainless steel additively manufactured arches	56
Appendix 8 – Comparison of additional results	59
Appendix 9 – Application of contour method Arcelor Mittal additively manufactured LPBF 316L components	64
Appendix 10 – Application of contour method to LPB-F 316L Arches samples (CETIM)	66
Appendix 11 – Application of LXRD measurements on LPB-F 316L Arches samples (CETIM)	68
Appendix 12 – Application of contour method to cast and quenched wedges and subsequent hole drilling	72
Appendix 13 – Application of neutron diffraction to the cast, quenched and T6 tempered aluminium wedge	76
Appendix 14 – Application of hole drilling measurements with strain gauges to cast and quenched wedges, L-PBF 316L Arches samples and ferritic U-bend shapes	77



Appendix 1 – Application of neutron diffraction to ferritic steel U-forms

The ferritic steel U-forms were measured with the monochromatic thermal neutron diffractometer called SALSA (Stress Analyser for Large – Scale engineering Applications) at the Institut Laue Langevin (ILL) in France. The instrument description and data analysis workflow is described in detail in the EASI-STRESS deliverable 4.2, but is briefly summarized below. As a sample stage, a hexapod or Stewart platform, a parallel kinematics robotic device with 6 degrees of freedom for translation (T_x , T_y , T_z) and rotation (R_x , R_y , R_z) movements, was used. Since the neutron diffraction method for residual stress determination is in principle non-destructive, the U-forms could be directly mounted onto the sample stage without prior sample preparation with a specialized support system. The sample positioning was done with a camera system. For the measurement of the radial component, the U-shapes were placed with the long side parallel to the hexapod table with an ω -rotation axis position of 45.5° (Figure 1 a). The radial collimators were chosen to obtain a gauge volume (GV) of $0.6 \times 0.6 \times 2$ mm. For the normal and transversal measurement direction, the orientation of the samples on the hexapod table had to be changed (Figure 1 b) and the GV was also changed to $2 \times 2 \times 0.6$ mm.

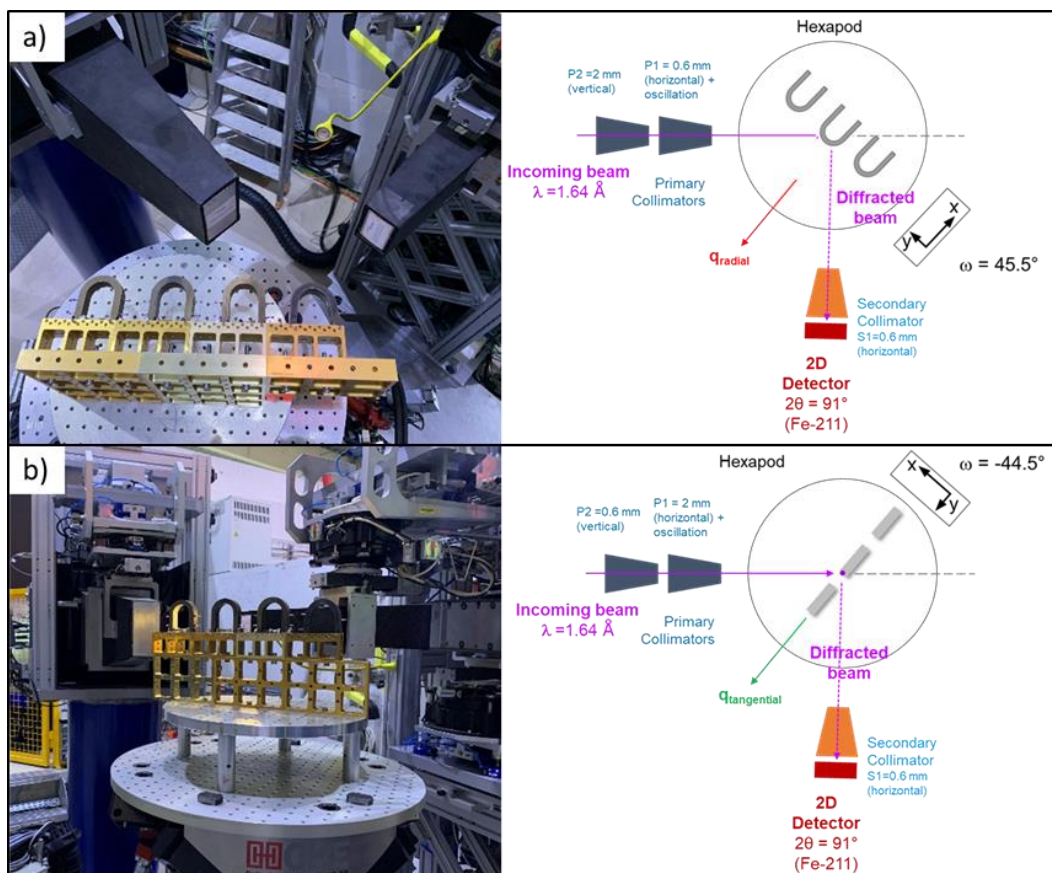


Figure 1 - Hexapod table (gray) with special support system (yellow) positioning the ferritic steel U-forms between the incoming beam path and the detector for the measurement of a) the radial component and b) for the tangential component.

To switch between the two configurations, only the ω -rotation axis position had to be changed from 45.5° to -45.5° . The 3.5 mm pin to be employed as a stress free reference sample (d_0) was measured in the same way. The raw data including metadata were saved in the NeXus format, and the raw data reduction (calibration, integration, peak fitting etcetera) was performed using an in-house data

analysis routine called LAMP (Large Array Manipulation Program) providing the reduced output data in an ASCII format. For each measurement point, one diffraction peak was obtained and fitted allowing to obtain single a lattice spacing value for each measurement point. The residual strain and stress values were then calculated using an in-house written script in Mathcad following the equations highlighted in the EASI-STRESS deliverable 4.2.



Appendix 2 – Application of synchrotron diffraction to ferritic steel U-shapes

The U-shape samples were measured at P61A White Beam Engineering Materials Science beamline at PETRA III (DESY-Hereon) in transmission geometry. A picture of the U-bend sample on the Eulerian cradle is shown below (Figure 1). The beam dimension was shaped with incident and diffracted slit apertures of $150 \times 150 \mu\text{m}^2$ and a 2θ angle of $\sim 5.02^\circ$, providing a diamond-like shape gauge volume with its long diagonal of $\sim 3.4 \text{ mm}$. The patterns were collected in a point high purity Ge-detector and the samples were aligned, similarly to the bridge samples, via the beam stop photodiode current. A normal pattern usually covers a range between 0 – 200 keV, including first and second order reflection peaks. All the scanned lines were measured with the sample positioned at different phi angles (0° , 90° , 180° , and 270°) aiming at performing a double immersion of the sample for the pseudo-strain correction. A ψ scan between 0° and 90° (with steps of 4.5°) was also performed at each phi angle to apply the $\sin^2\psi$ method. The strong texture of the specimens and the small size of the GV requires the application of this method to obtain reliable stresses. The studied plane was the α -211 and the d_0 was calculated by assuming that normal stresses in the scanned lines are self-equilibrated, i.e. their sum equals to zero. An in-house software, P61A::Viewer, was used for the data reduction and peak position determination and a pseudo Voigt function for the peak fitting.

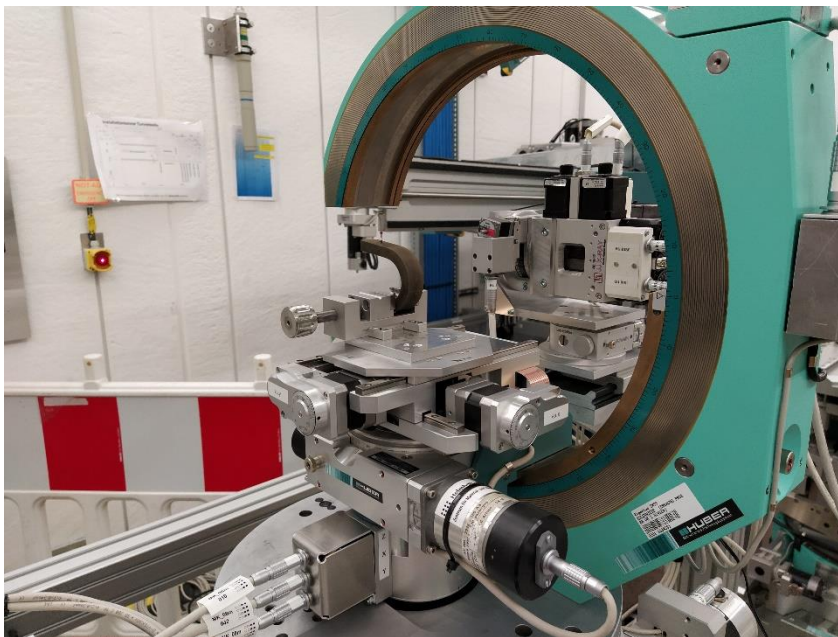
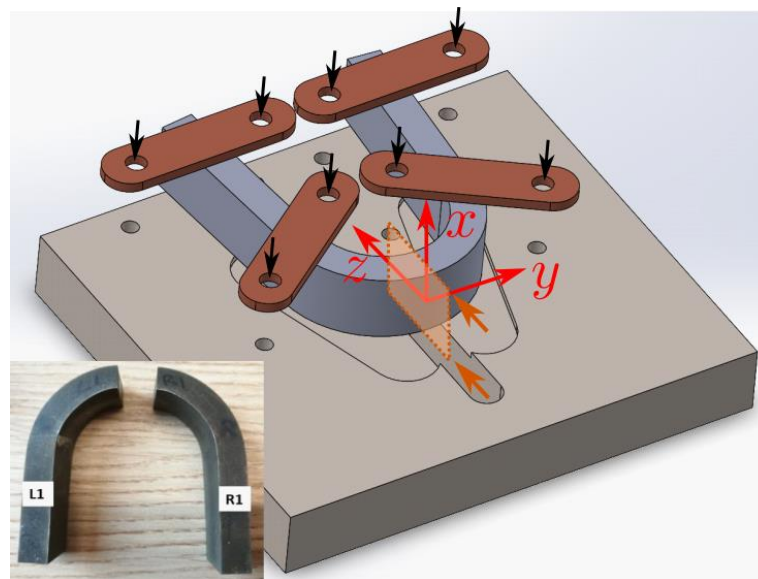


Figure 1 - View of the U-bend sample on the Eulerian cradle at P61A beamline.

Appendix 3 – Application of contour method to U-bend ferritic shapes and preparation for LXRD

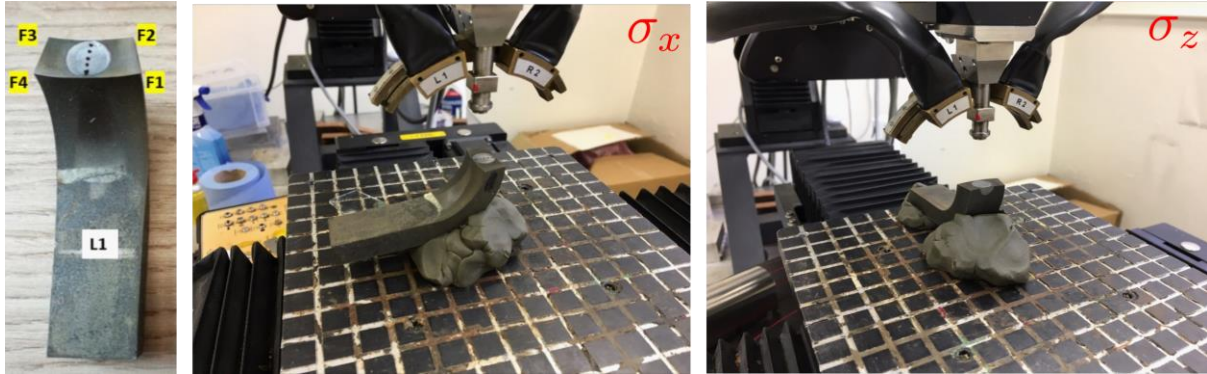
Two ferritic shapes were first subjected to a contour method measurement in an identical manner. A tooling plate was machined with relief cuts to allow clearance for the flanks of the bend, such that the part was located on the undeformed legs. A further relief cut through the plate allowed clearance for the electrodischarge machining wire. The component was fixed with aluminium crush plates at four locations with M6 fasteners, torqued equally to 14 Nm. A cut was then performed running from the extrados to the intrados with a modified 'E2' settings on an Agie-Charmilles FI440CCS CNC WEDM and a 250 μm hard brass wire. The following figure shows the cutting arrangement, with the M6 fastening points shown with black arrows, the cutting plane and direction in orange, and the component coordinate system employed. This resulted in two sides of the cut, left and right which were further tracked as L1 and R1 for B1 and L2 and R2 for B2. L1 and R1 are shown below.



After contour cutting, each cut face was measured with a Nanofocus μScan laser profilometer with a 30 x 30 μm resolution across the plane of measurement, and $\pm 0.2 \mu\text{m}$ out of plane. The resulting point clouds obtained were then processed with pyCM v2.0.0 in order to obtain the stress acting normal to the cutting plane (σ_y) and the normal residual stresses relieved by the cut acting in-plane. Outliers appearing on each surface were manually eliminated, which is surmised to have been generated from plasticity occurring in the last 2 mm or so of cutting length, as the wire exited the intrados. The remaining data from each face was aligned and averaged to a common grid having an equidistant spacing of 200 μm , and fit with a bivariate spline having an equidistant knot spacing of 3 mm. This spacing was chosen on the basis of minimizing error in fitting as assessed by the root mean square error (RSME) while avoiding over-fitting. The peak error in fitting occurred at wire entry and exit artefacts, rising to $\sim 7 \mu\text{m}$, however the majority of the surface was fit within 2 μm . The obtained spline was then applied as a boundary condition to a linear elastic finite element analysis, with a mesh generated from the measured outline, extruded 5 mm out of plane comprising $\sim 13,000$ nodes and $\sim 11,000$ elements. Elastic properties employed was an elastic modulus of 205 GPa and Poisson's ratio of 0.3. The die-off length (i.e. the out of plane distance that the resolved stress state returned to zero) was approximately 2 mm; this validates the choice of domain selected.

After the cuts were performed, each cut face was prepared for LXRD measurement. The contour cut surface was electropolished to a depth of $\sim 150 \mu\text{m}$ with a Proto Model 8818-V3 electrolytic polisher. Each cut half was measured with a Proto-XRD diffractometer with a Cu-K α source, employing the

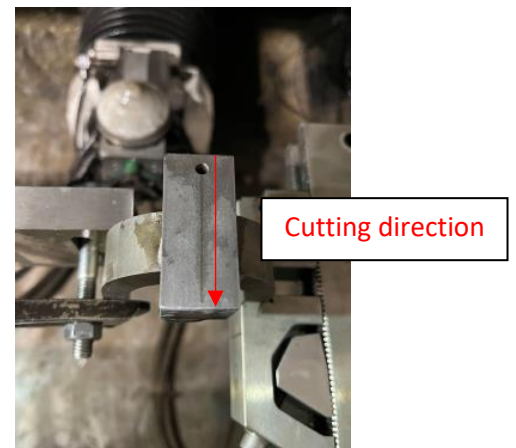
$\sin^2\psi$ method with rotations in Ψ and β with a spot size of 1 mm in diameter. Background values were subtracted on a linear basis. The sample was moved between each stress measurement orientation as shown in the figure below. Values of fiducial points as well as the center of each spot were reported on the same coordinate system for each sample measured: L1, R1, L2 and R2. After measurement on the Proto system, the components were packaged and relayed to other practitioners of LXR D with no further modifications.



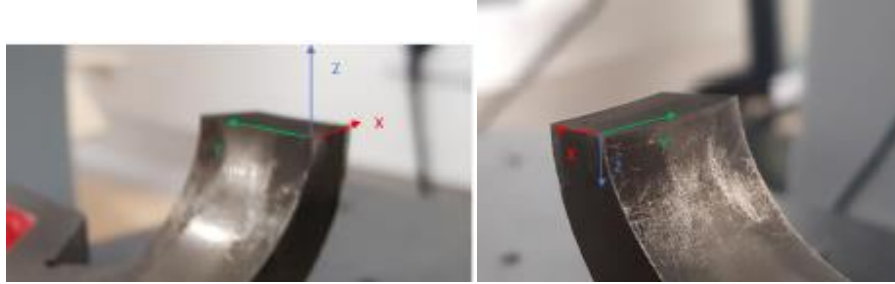
Appendix 4 – Application of contour method to U-bend ferritic shapes

Only one ferritic shape has been subjected to a contour method measurement. The cutting of the part is realized by wire electro-discharge machining (Fanuc Robocut a-C600iB) to relax the stresses in the material. An uncoated brass wire is used with a 0.15 mm diameter. Stress relaxation is then expressed into deformation through the cutting plan. After that, both of the two deformed surface of the cutting plan are measured using a 3-dimensional measuring machine (MMT). A finite element simulation is finally performed by imposing displacements measured by CMM to calculate the stress state before relaxation.

The two resulting cutting halves of the sample will be used after that for XRD measurements. The fixing system and the parts themselves have been prepared for the cut as shown below. A cut was then performed running through the red arrow. The objective was to obtain the residual stresses in the longitudinal direction on the section of interest indicated by the blue arrow.

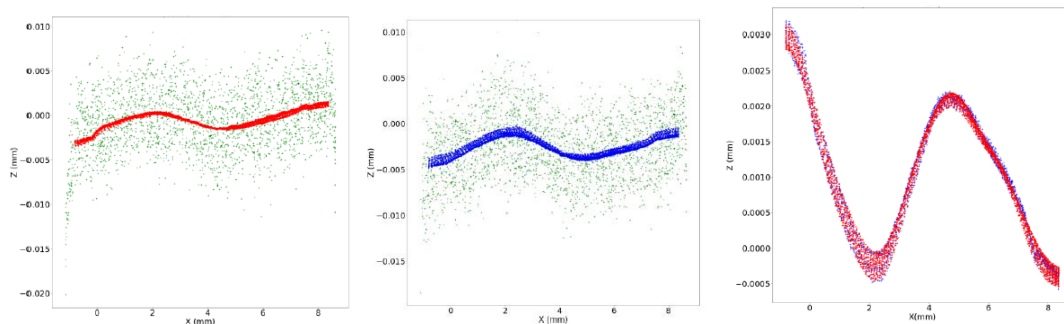


The cut surfaces of the half-shape were then measured by this control configuration.



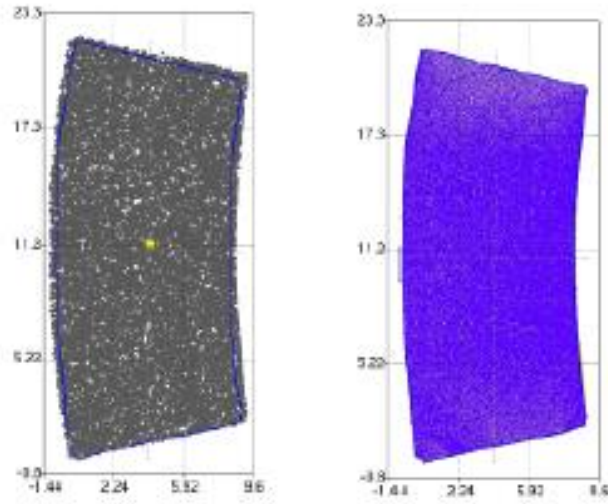
Cartography data have been extracted using a classical ± 0.1 mm extremum filter. The recovery has been done using medium filter with 0.005 mm tolerance and 0.1 mm radius. Another filter (as called MOG filter) with 1 mm parameter is used as a moving average type on the 1 mm dimension area.

The interpolation parameter (density of nodes of the spline) was chosen according to the Mat-In-Meca measurement protocol. The files contain approximatively 30 000 data points after filtering to characterize the section deformations. Sequential filtering of cutting defects and smoothing of the profile obtained is shown below from left to right:



The first graph on the right is the raw profile after the first filter for the “right” surface. The second one is the raw profile after the first filter for the “left” side. These filters are applied for cleaning the point clouds and for noise reduction. On the last one the points after the first filter are inverted and merged on the same graph and then interpolated by bivariate spline.

The half-shape of the studied section has also been modelled with *Gmsh* to describe a mesh suitable for calculating the stress profile from displacement boundary conditions and elastic properties. A mesh consisting of a 4-node tetrahedral mesh, setting in data with imposed displacements, linear solver and finally post-treatment. The material parameters used were $E = 210$ GPa; $\nu = 0.3$. Here is the extraction of the modelled section with the associated mesh:

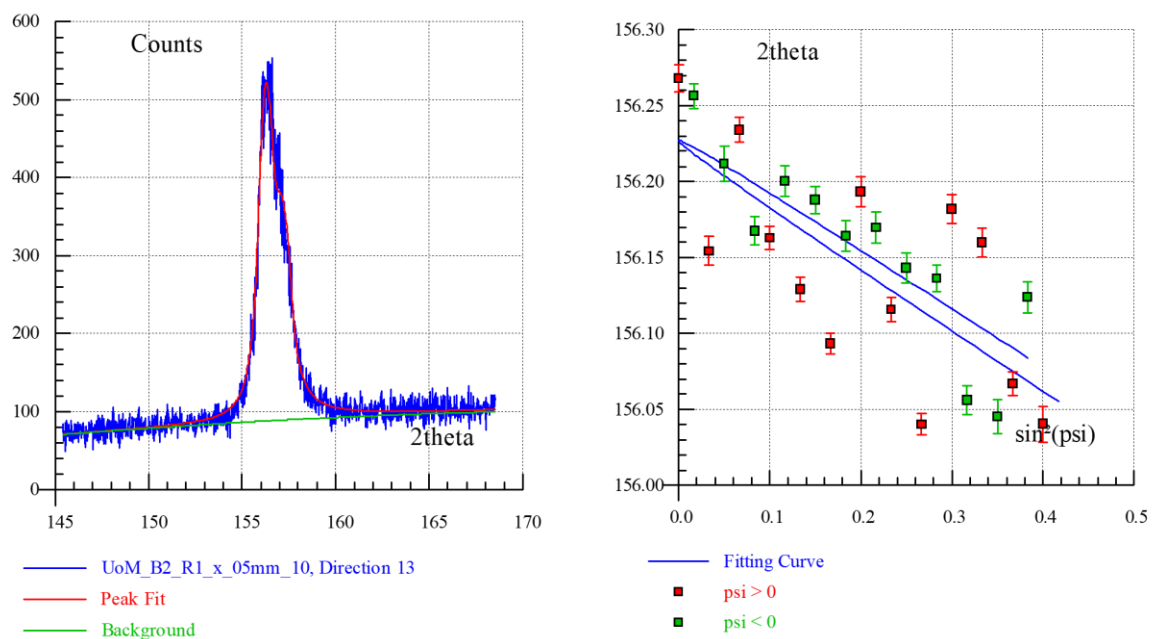


Appendix 5 – Application of LXRD to cut U-bend ferritic shapes

Residual stresses were measured on the surface of the contour cut U-bend ferritic shapes (see Appendix 3 – Application of contour method to U-bend ferritic shapes and preparation for LXRD). No additional sample preparation was conducted after receiving the cut and electropolished specimens L2 and R2.



The measurements were done using an Xraybot from MRXrays using the $\sin^2\Psi$ method. The measurements were done on the ferrite $\{211\}$ peak using a Cr $K\alpha$ source with V filter at 20 kV and 1 mA. A 0.5 mm collimator was used, but due to the divergence of the beam, the beam size on the sample is expected to be up to 1.5 mm in diameter. The sample was positioned by eye using a pointer, so some uncertainty in the positioning of app. 1 mm must be expected. 25 Ψ directions were measured for each point and stress direction using $\Psi = \pm 40^\circ$ with 240 s exposure for each angle ensuring a signal above background of 200 counts. The diffraction peaks were fitted using a pseudo-Voigt peak and linear background, while the $\sin^2\Psi$ curve was fitted with an ellipsoidal line fit (see example below). The materials parameters used for inferring the stress were $E = 205$ GPa, $\nu = 0.29$ and $Ar_x = 1.39$.



Due to an observed systematic offset/error in the stress results when measuring the x- and z- directions simultaneously (by getting the robot to make Ψ -tilts in the two directions), the two

directions were measured by rotating and re-aligning the sample. There can, hence, be a small offset between the points measured in the two directions.



Appendix 6 – Application of neutron diffraction to austenitic steel AM Arches

The austenitic additive manufacturing arches were measured with the monochromatic thermal neutron diffractometer SALSA at the ILL. As a sample stage, the hexapod was used. Since the neutron diffraction method for residual stress determination is in principle non-destructive, the three arches were mounted directly onto the sample stage with a specialized support system without prior sample preparation. The samples were mounted in the following order from left to right: BA-02, BA-01, and BV-01 (Figure 1 a). The corner highlighted in blue (Figure 1 a and b) was used for positioning the sample. This was done with a camera system. The 2θ angle used for all the measurement of all the strain components was 98.5° in order to observe the Fe (311) reflection. The radial collimators were chosen to have a gauge volume (GV) of $0.6 \times 0.6 \times 2$ mm for the normal, longitudinal, and transversal direction. The measured points are shown in Figure 2. For the measurement of the transversal component, the arches were placed with the opening in the x-direction on the hexapod table with an ω -rotation axis position of 49.25° (Figure 1 a). For the normal and transversal measurement direction, the orientation of the samples on the hexapod table had to be changed and the opening of the arches was facing upwards into the z-direction (Figure 1 b). To switch between the two configurations, only the ω -rotation axis position had to be changed from -40.75° to 49.25° . For obtaining d_0 values, powder samples were measured. The raw data including metadata were saved in the NeXus format, and the raw data reduction (calibration, integration...peak fitting) was performed using the in-house data analysis routine called LAMP providing the reduced output data in an ASCII format. For each measurement point, one diffraction peak was obtained and fitted allowing to obtain single a lattice spacing value for each measurement point. The residual strain and stress values were then calculated using an in-house written script in Mathcad following the equations highlighted in the EASI-STRESS deliverable 4.2.

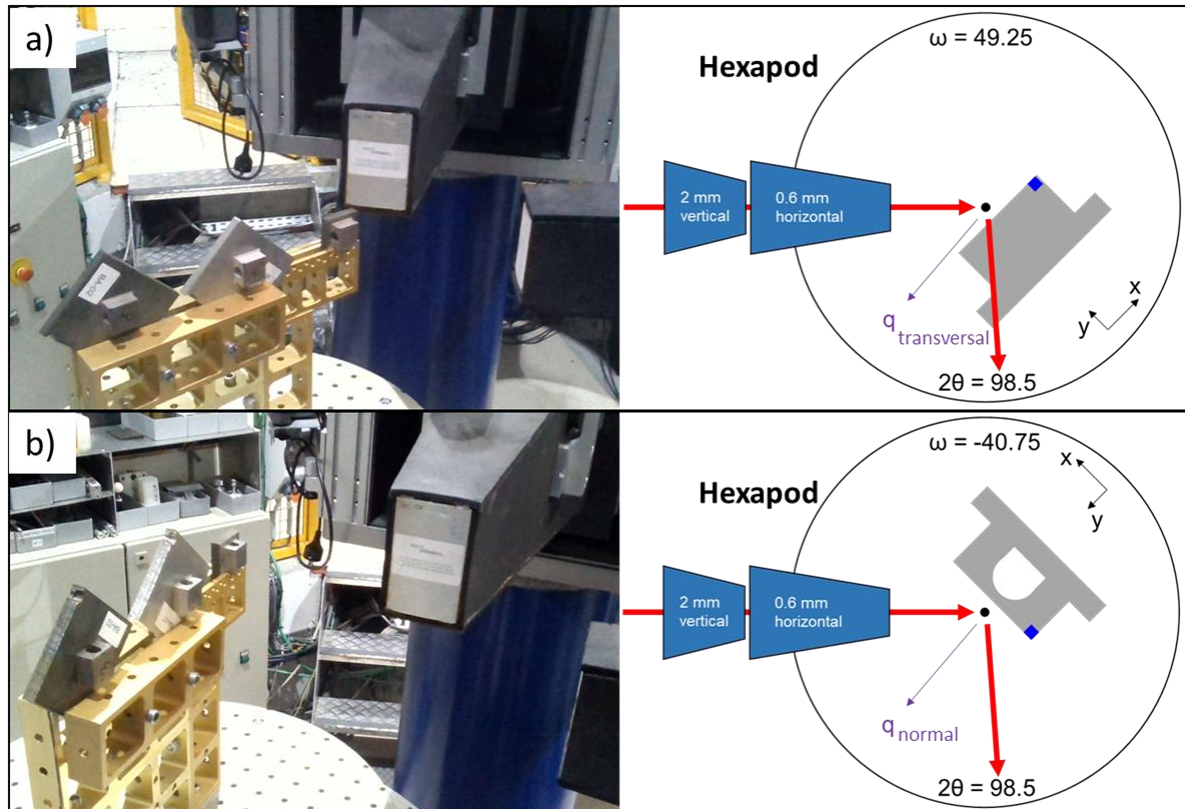


Figure 1 - Hexapod table (gray) with special support system (yellow) positioning the three austenitic AM arches between the incoming beam path and the detector for the measurement of a) the transversal component and b) of the normal component. Shown in picture (left) but not in graphic (right): 0.6 mm horizontal radial collimator in front of the detector.

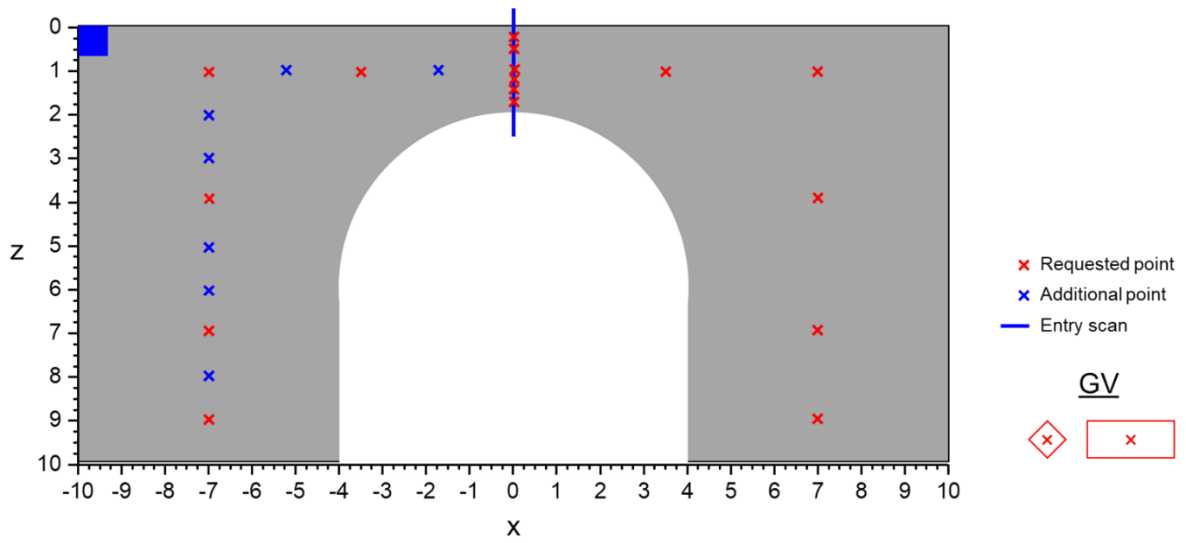


Figure 2 - Measurement points in the neutron diffraction experiment at SALSA as well as the dimensions of the gauge volume as a reference.

Appendix 7 – Application of synchrotron diffraction to the powder-derived stainless steel additively manufactured arches

The arches, supplied by ArcelorMittal in as-built and HT conditions, were measured at the High-Energy Materials Science Beamline (HEMS) P07 at PETRA III (DESY-Hereon) and at P61A White Beam Engineering Materials Science beamline at PETRA III (DESY-Hereon). The measurements are detailed following:

- a) P61A: A white beam in transmission geometry was used for the stress determination of the different scanned lines. A picture of the as-built sample on the Eulerian cradle is shown below (Figure 1). The beam dimensions were shaped with incident and diffracted slit apertures of $150 \times 150 \mu\text{m}^2$ and a 2θ angle of $\sim 5.97^\circ$, providing a diamond-like shape gauge volume with its long diagonal of $\sim 2.9 \text{ mm}$. The samples were aligned via the transmitted intensity collected by the beam stop photodiode current and the patterns were collected in a point high purity Ge-detector. All the scanned lines were measured with ψ scans (between 0° and 90° with 5° steps) at different phi angles (0° , 90° , 180° , and 270°) in order to apply the $\sin^2\psi$ method and increase the goodness of the calculations, i.e. only one detector was used during the measurements. Therefore, the gauge volume was elongated in different directions depending on the phi angle. The studied plane was the γ -311 (which is the peak analysed in the measurements with the CSC and neutron diffraction) and two combs (see Figure 2), machined out from duplicates of the samples, were used as stress-free references. Similarly to the U-shapes, the in-house software, P61A::Viewer, was used for the data reduction and peak position determination with a pseudo Voigt function.

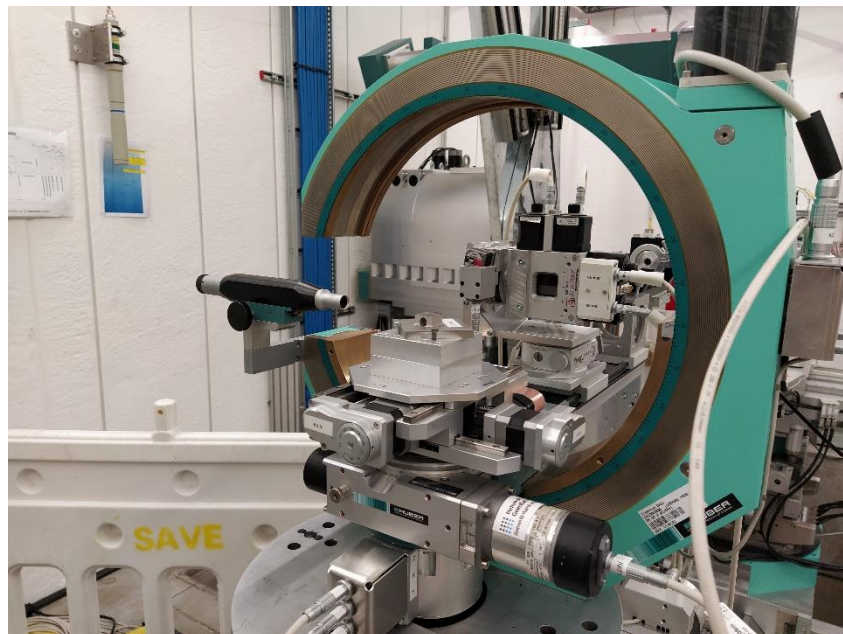


Figure 1 - View of the as-built sample, provided by ArcelorMittal, on the Eulerian cradle at the P61A beamline. The slits defining the size of the incident beam are shown behind the sample.

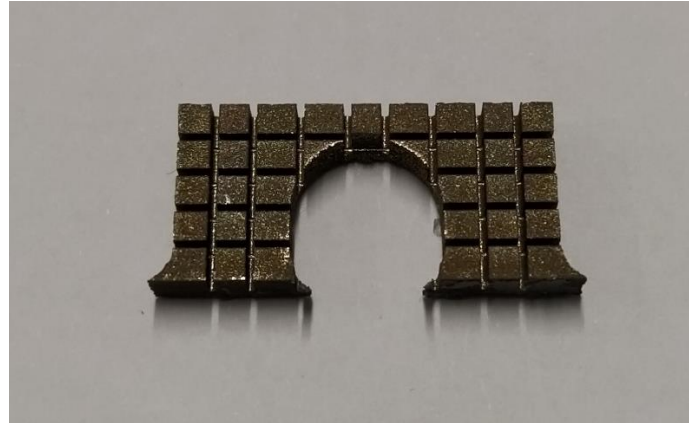


Figure 2 - 3D comb obtained from a duplicate of one of the AM samples (with identical thermal history condition) produced by electrodischarge machining.

- b) P07: A monochromatic beam coupled with a CSC allowed depth-resolved residual stress analysis of the selected regions. A picture of the sample mounted on the stage is shown in Figure 3. The incident beam supplied an energy of 112.67 keV ($\lambda=0.011004$ nm) with aperture slits of $200 \times 200 \mu\text{m}^2$. The images were collected using a 2-D (flat panel) Perkin-Elmer detector with an array of 2048×2048 pixel and a pixel size of $200 \times 200 \mu\text{m}^2$. The gauge volume resulted in an elongated length of ~ 1.9 mm. The samples were aligned with a photodiode placed in between the CSC and the sample. All the scanned lines were firstly measured with the y axis of the sample parallel to the beam direction (i.e. for strains in x and z direction) and subsequently rotated 90° for the measurement of the pending orthogonal direction with the x axis parallel to the beam (i.e. strains in y and again z direction). Therefore, and identically to the measurement at the P61A beamline, the gauge volume was elongated in different directions. The analysed crystallographic plane was the γ -311 and the same combs as for the P61A were used as stress-free references. The Fit2D software was used for the data reduction and peak position determination. A Voigt function was used for the peak fitting. The $\sin^2\psi$ method was applied to both measurements in order to improve the goodness of the calculations.

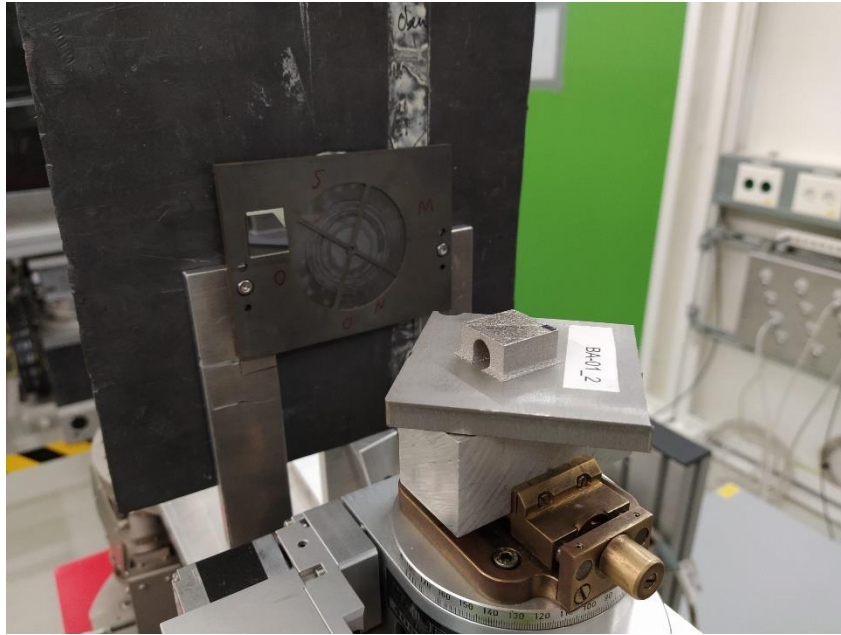


Figure 3 - View of the as-built sample provided by ArcelorMittal on the stage at P07. The CSC is behind the sample.

Appendix 8 – Comparison of additional results of LRI diffraction techniques on arches

The different scanned lines for the high energy diffraction experiments are indicated in Figure 1. The number of measured points varied depending of the facility and/or instrument and the available beamtime for the experiment. A cross-comparison between different samples and LRI techniques is enabled due to the refined microstructure of the samples in all conditions.

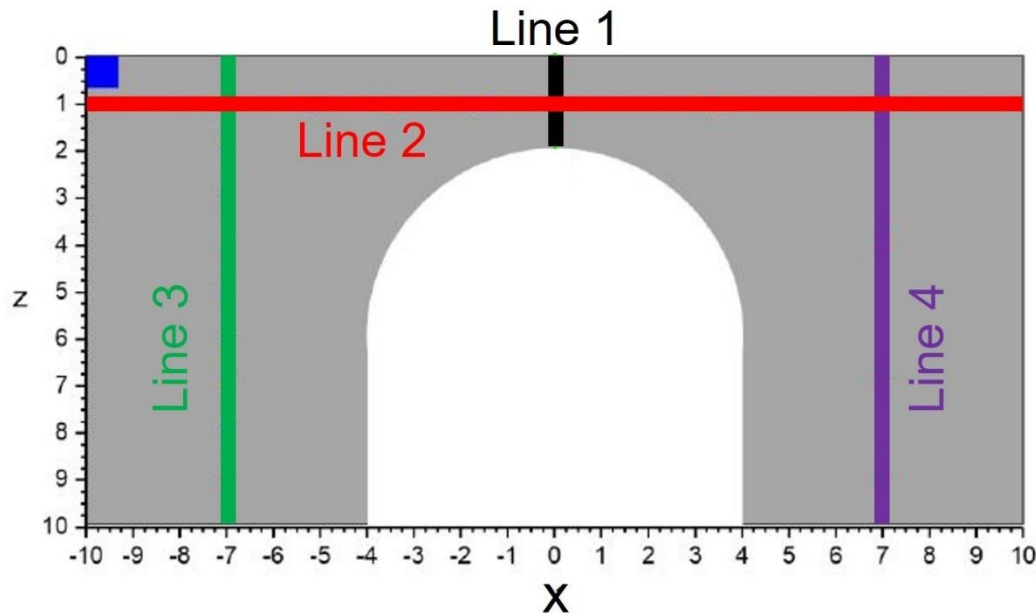


Figure 1 - Scan lines with the high energy diffraction experiments: Line 1 at the centre, Line 2 is 1 mm below the top surface, and Lines 3 and 4 are vertical scans top-down at $x=\pm 7$ mm.

The main issue when measuring AM samples with high energy diffraction techniques is the correct determination of a suitable stress-free reference, as d_0 tends to vary through the cross section. Thus, there is no constant stress-free reference value but a gradient (as opposed to many other metallic materials). A possible solution to overcome this issue is to machine out 3D combs which are supposed to release most of the macro-stresses, accounting for the different microstructure and chemical composition variation throughout the cross section of a sample. This method requires a) additional beamtime for a correct characterization of the reference sample (mainly for the SXRD technique) because single measurements at the required positions do not guarantee a reliable d_0 and it is always better to scan completely the teeth of the combs and average over them and b) high accuracy to position the gauge volume within the teetehes of the comb (which apply to both synchrotron X-Ray and neutron diffraction techniques). Only Hereon, among the LRIs, measured the combs while ILL and ESRF used the raw powders as stress-free references. This issue led to shifts in the stress curves which were overcome by using the VM equation, that is only a function of the stress differences (i.e. the stress-free reference does not play any role).

Unlike metallic materials produced by forging, the AM technology does not ensure that the principal directions coincide with any of the axes of the sample, i.e. they have to be determined and the $\sin^2\psi$ method is the appropriate technique for this purpose. It relies on the measurement of the interplanar variation in a plane orthogonal to the beam direction at different angles between the two orthogonal directions to be measured. SXRD facilitates the use of the $\sin^2\psi$ methodology either

with 2D detectors (monochromatic beam) or with the sample rotation with an Eulerian cradle (white beam). The advantage of this technique is that several peak positions are used for fitting a straight line with high fit confidence (in absence of shear stresses) and it was used by Hereon to 1) improve the goodness of the strains, and 2) discard the presence of shear stresses. The ESRF aimed at directly evaluating the shear stresses and could observe that shear stresses oscillated around zero MPa (with low absolute values), i.e. it was ruled out their presence that could have developed during the sample processing of the AM samples. Thus, the coordinate axes x, y, and z (Figure 12 of “4.2 Powder-derived stainless steel additively manufactured arches”) are assumed to be also the principal directions.

Figure 2 to figure 3 compare the absolute stresses on Line 3. It can be seen that the use of different stress-free references hinders a proper comparison between stresses measured at different LRIs. As a general trend, stresses in the as-built condition are higher than those in the HT condition (always comparing measurements performed at the same LRI), i.e. the HT at 700 °C provokes a stress relaxation in some regions of up to ~ 200 MPa (similarly to that observed for Line 1 and detailed in “4.2 Powder-derived stainless steel additively manufactured arches”) . RS on Line 3 in z direction decrease monotonically as a function of the height up to z ~ 6 - 8 mm, remaining constant onwards, while in x and y directions they are similar and decrease from the top surface up to a depth of ~ 3 – 4 mm, remaining constant after or undergoing small increments.

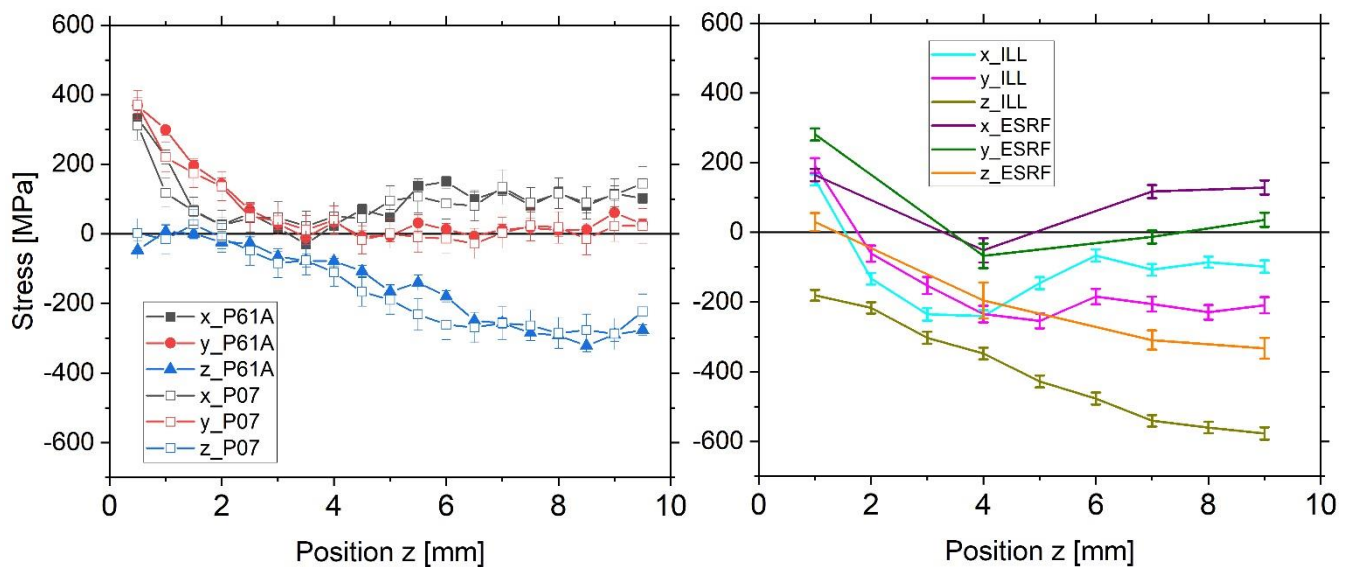


Figure 2 - Results from ArcelorMittal sample in As-built condition on Line 3 for Hereon (left) and ILL and ESRF (right).

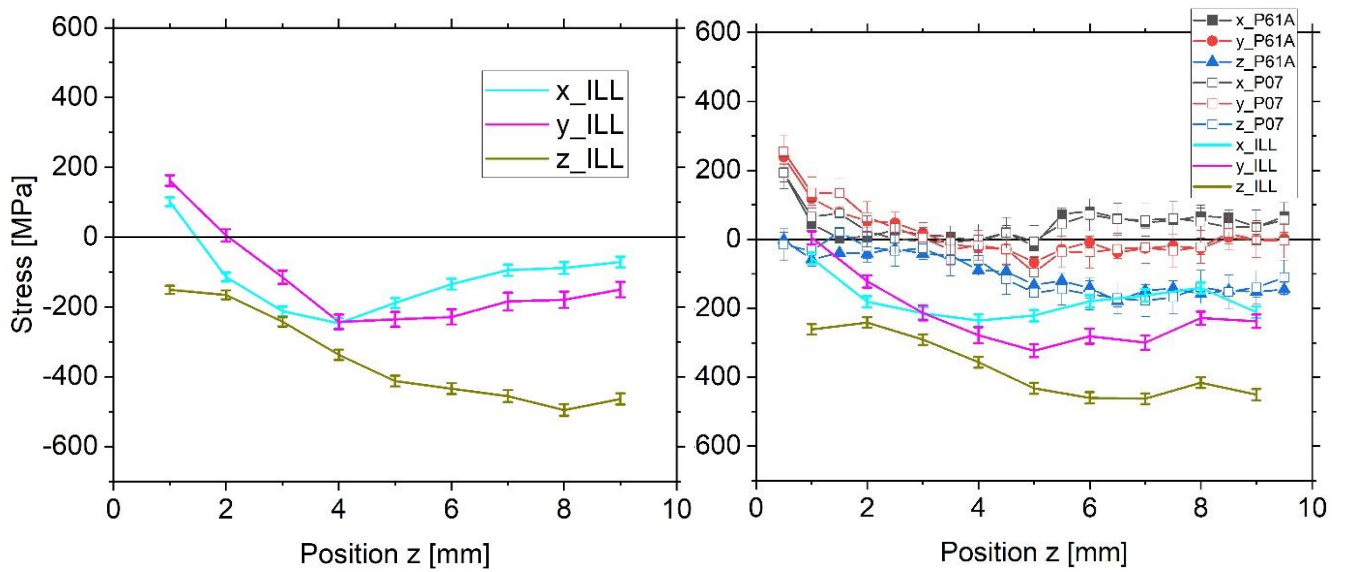


Figure 3 - Results from Volum-e sample in As-built condition on Line 3 for ILL (left) and from ArcelorMittal sample in HT condition on Line 3 for Hereon and ILL (right).

Figure 4 compares the VM stresses calculated on Line 3 from the results of the different labs. It should be noted that there is a remarkably good agreement between the results of different labs and techniques when VM stresses are compared. This means that a good portion of the reasons for differences in absolute results comes from an incorrect determination of the stress-free reference value. Thus, the present results confirm once more the importance of proper reference material and measurements.

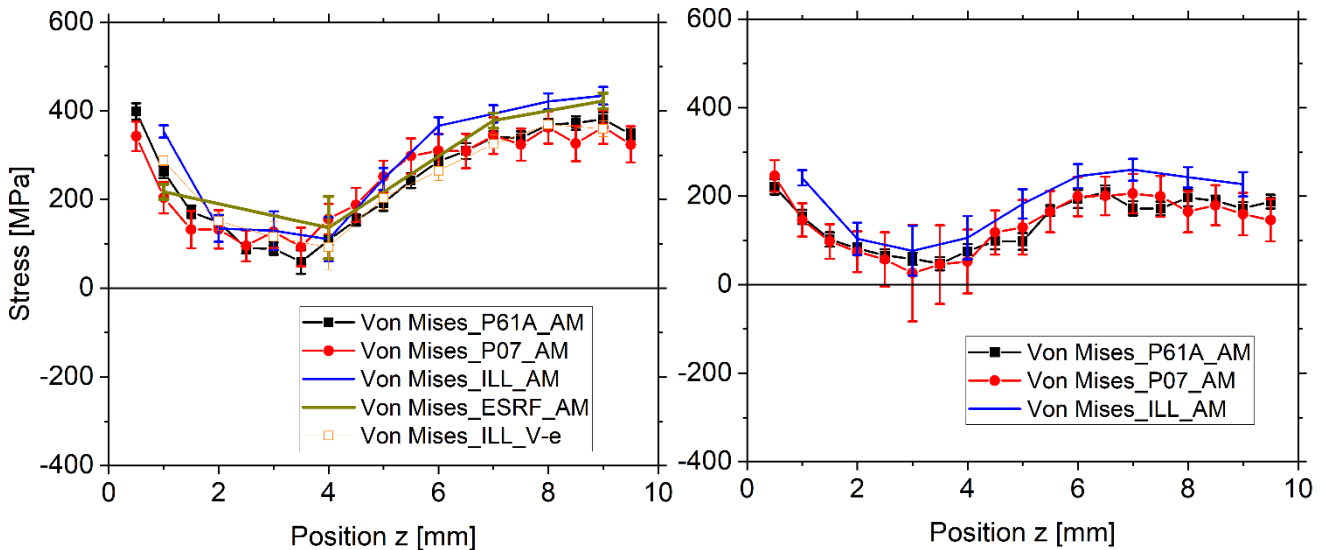


Figure 4 - Stresses calculated with the VM formula on Line 3 in As-built condition for Hereon, ILL, and ESRF (left) and in HT condition for Hereon and ILL (right). AM=ArcelorMittal sample, V-e=Volum-e sample.

The measurements on Lines 2 and 4 (figure 5 to figure 7) are detailed following. Identically to the already commented Line 3, stresses in as-built condition are higher than those in the HT condition (when compared measurements performed at the same LRI). Stresses on Line 2 are constant or undergo small variations in x and y directions (when away from the edges of the samples) while stresses in z direction (for Hereon) are roughly zero in as-built condition and slightly compressive in HT condition. On Line 4 (symmetric to Line 3 with respect to the z axis), same trends as for Line 3 are observed, i.e. the reproducibility of the L-PBF technology is optimal.

Figure 8 to figure 9 compare the VM stresses of the different LRIs. Line 2 exhibits, as it could be inferred from the total stresses, a constant behaviour with stress levels of ~ 300 MPa and ~ 200 MPa for the as-built and HT conditions, respectively. Line 4 follows the same trends as for Line 3. The good agreement between results from different labs when using the Von Mises formula confirms again the importance of confidence stress-free references.

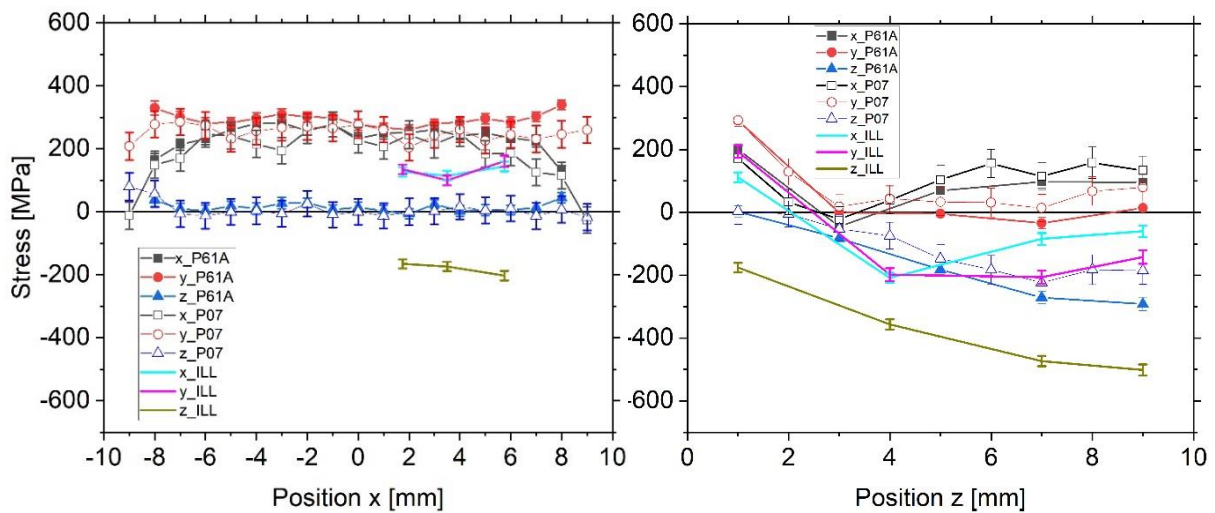


Figure 5 - Results from Arcelor Mittal sample in as-built condition on Line 2 (left) and Line 4 (right) for Hereon and ILL.

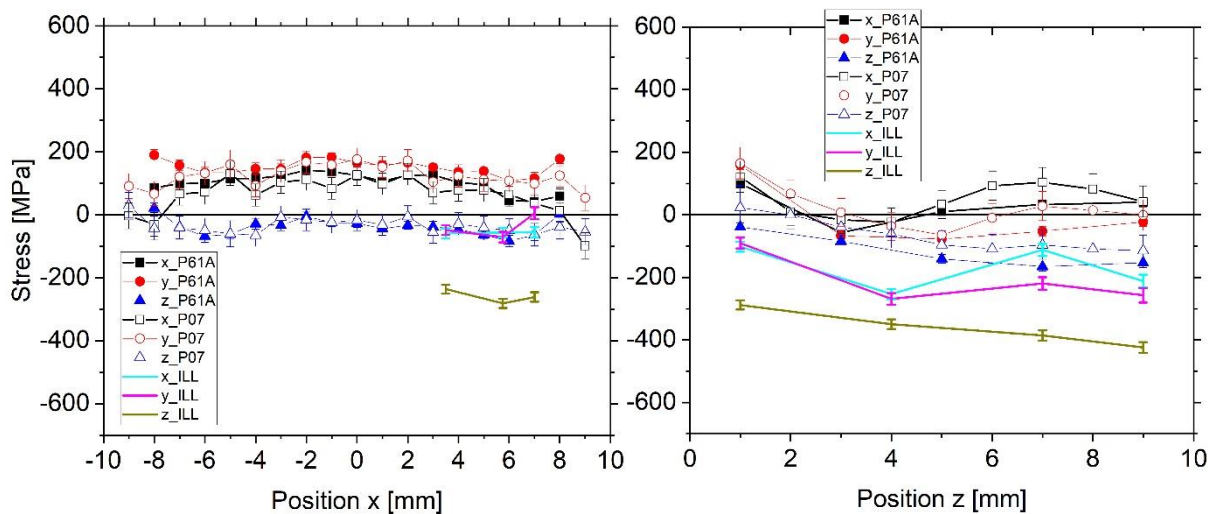


Figure 6 - Results from ArcelorMittal sample in HT condition on Lines 2 (left) and Line 4 (right) for Hereon and ILL.

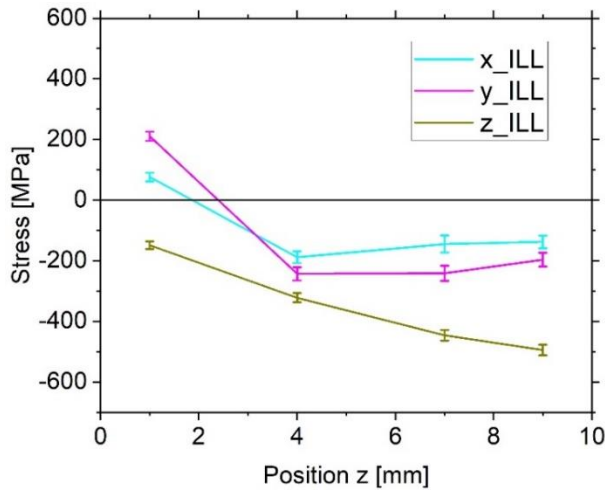


Figure 7 - Results from Volum-e sample in As-built condition on Line 4 for ILL.

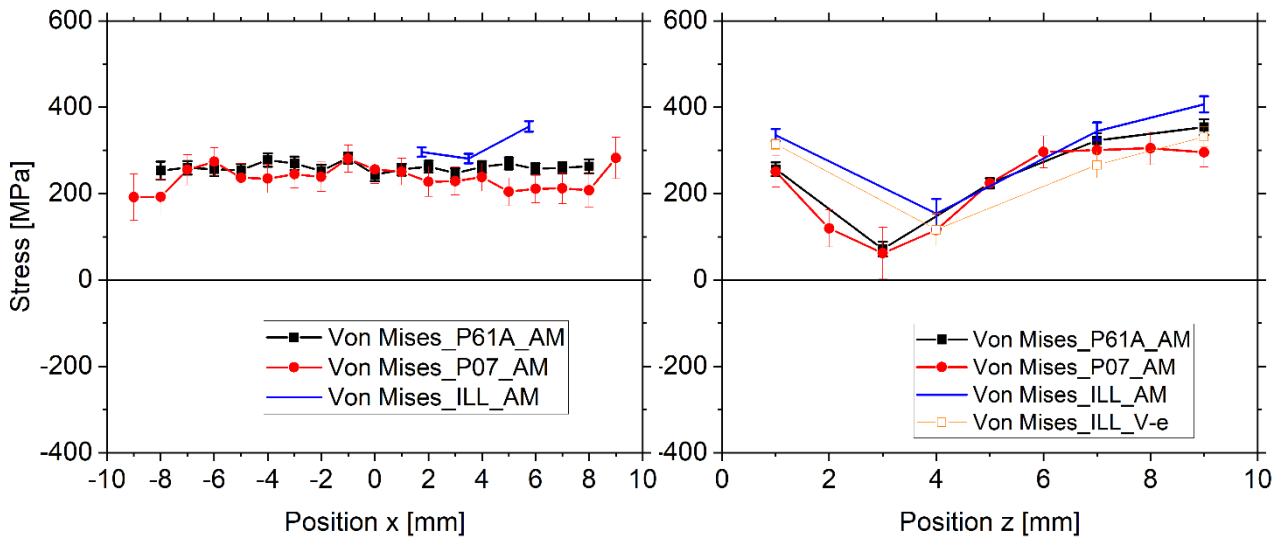


Figure 8 - Stresses calculated with the VM formula in As-built condition on Lines 2 (left) and 4 (right) for Hereon and ILL. AM_ArcelorMittal sample, V-e_Volum-e sample.

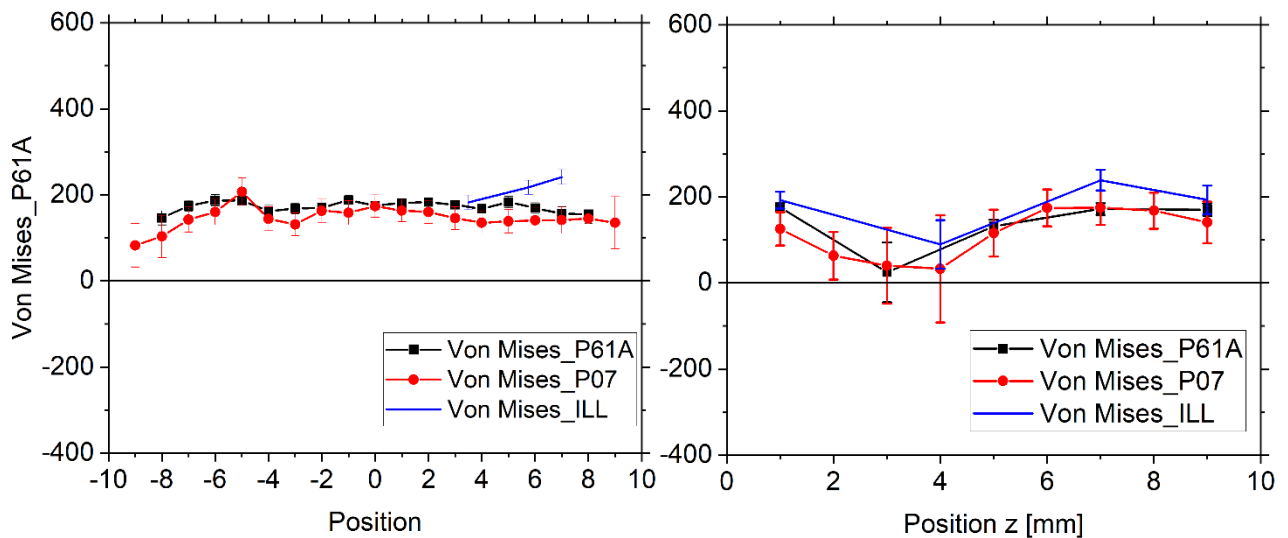
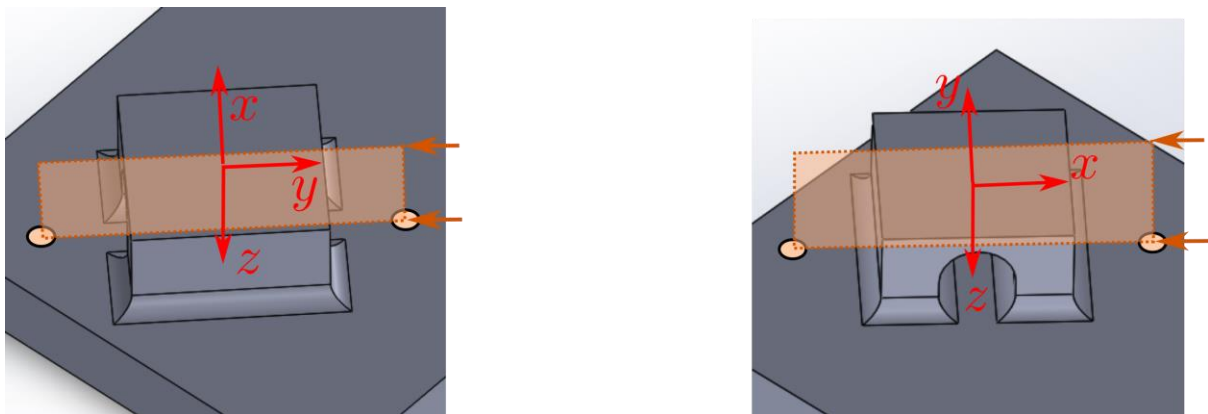


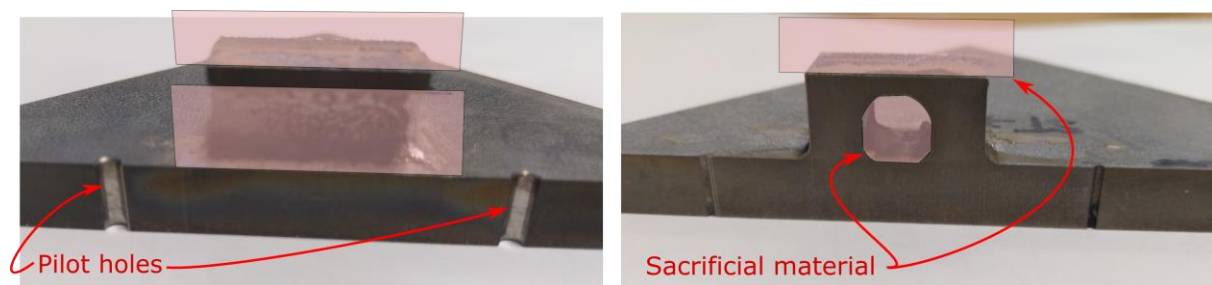
Figure 9 - Stresses calculated with the VM formula from ArcelorMittal sample in HT condition on Lines 2 (left) and 4 (right) for Hereon and ILL.

Appendix 9 – Application of contour method Arcelor Mittal additively manufactured LPBF 316L components

Four components were received on a baseplate in both the as-built and heat-treated condition. The contour cutting and analysis was identical between the as-built and heat treated conditions. Cuts were performed by the Open University (UK) incorporating the use of self-restraint. This was of the form of pilot holes either drilled or machined at least half of a component away from the part (>10 mm). Sacrificial material was affixed to the top of each component, along with a piece of filler rod through the annulus of the arch opening. These were affixed with Ag-doped conductive epoxy with the aim to avoid cutting artefacts. The figure below shows the arrangement employed for obtaining stresses in the x direction (left) and stresses acting in the y direction (right).



Cutting via WEDM was then conducted between each of the pilot holes, running through sacrificial material, the component, and baseplate all at once, with the wire running into the part along the z direction, and travelling in the negative y and x directions to obtain cuts pertaining to stress in the x and y directions respectively. Once the cut between the pilot holes was completed, then the cut was restarted in each of the pilot holes to cut through the remaining ligaments. The figure below shows an indicative result for both orientations, and the position of sacrificial material during the cut.

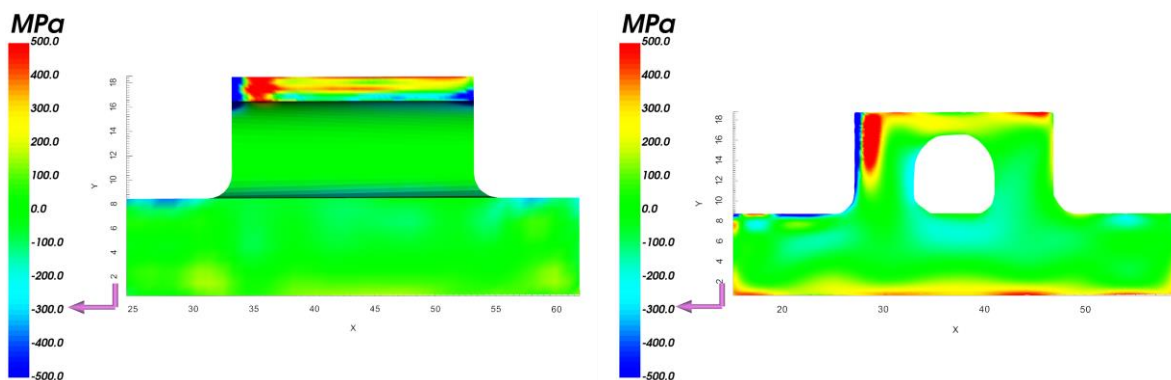


Both cut surfaces for each component considered was measured with a NanoFocus laser profilometer to obtain surface variation of the entire cut surface $30 \times 30 \mu\text{m}$ resolution across the plane of measurement, and $\pm 0.2 \mu\text{m}$ out of plane. The result was then analysed with pyCM v2.0.0, with registration and averaging taking place to create a uniform averaged surface with a point spacing of 0.06 mm for the domain lying between the pilot holes. A unique feature of pyCM was employed to fit different splines to each of the unique surfaces for the analysis considering stress in the x. Here, a bivariate spline with a knot spacing of 3 by 2.5 mm was employed for the baseplate, and 3 x 0.75 mm for the upper ligament of the deposition. A uniform 4 by 4 mm knot spacing was used for resolving stresses in the y direction. These values were found by iterating on values to

ensure that the resultant spline did not overfit the underlying data while minimising the root mean square error of the result.

The spline fitting step was followed by preprocessing a supporting finite element analysis. Meshing was carried out to generate a quadratic tetrahedral mesh of the entire half of the component for stress in the x direction, while the profile obtained by surface scanning was extruded to obtain a mesh to resolve stresses in the y. Approximately 150-200,000 nodes were used to generate approximately the same number of elements. The elastic properties employed were 195.6 GPa for the modulus, and 0.294 for Poisson's ratio.

Screen captures from pyCM's finite element analysis post processor are shown below, with stress acting in the x direction on the left, and in the y direction on the right. Cutting direction is shown with the purple arrow.



Appendix 10 – Application of contour method to LPB-F 316L Arches samples (CETIM)

Three different arches samples have been subjected to a contour method measurement. The cutting of the part is realized by wire electro-discharge machining (Fanuc Robocut a-C600iB) to relax the stresses in the material. An uncoated brass wire is used with a 0.15 mm diameter. Stress relaxation is then expressed into deformation through the cutting plan. After that, both of the two deformed surfaces of the cutting plan are measured using a 3-dimensional measuring machine (MMT). A finite element simulation is finally performed by imposing displacements measured by CMM to calculate the stress state before relaxation.

The two resulting cutting halves of the sample will be used after that for XRD measurements. A picture of the cut part is presented below, just to show the aspect of the different samples after cutting. The cut has been performed running through the red arrow. The objective was to obtain the residual stresses in the longitudinal direction on the section of interest indicated by the blue arrow.



The cut surfaces of the half-shape were then measured by this control configuration.

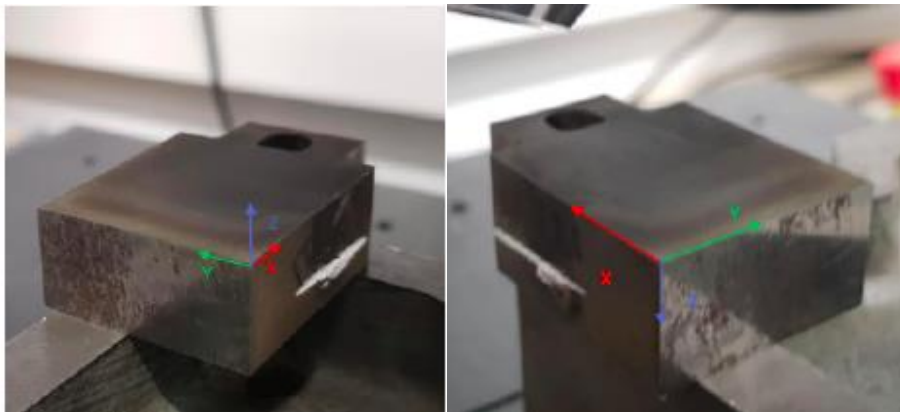


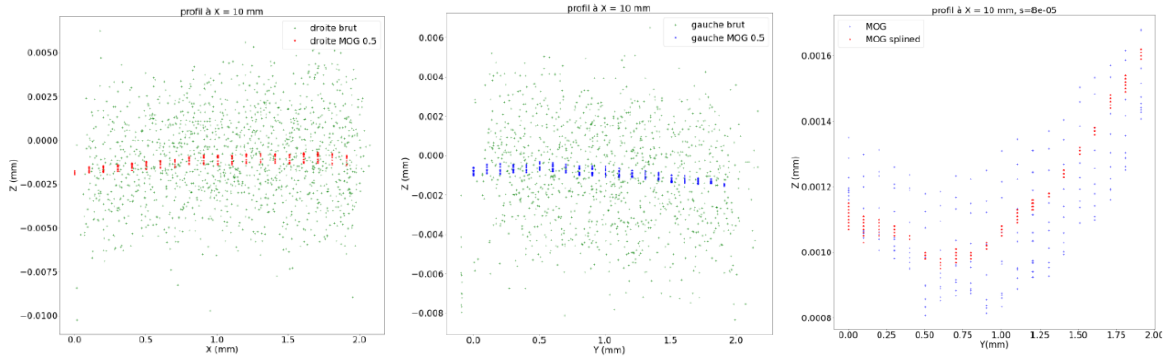
Figure 1: Right side

Figure 2: Left side

Cartography data have been extracted using a classical ± 0.1 mm extremum filter. The recovery has been done using medium filter with 0.005 mm tolerance and 0.1 mm radius. Another filter (as called MOG filter) with 0.5 mm parameter is used as a moving average type on the 1 mm thickness.

The interpolation parameter (density of nodes of the spline) was chosen according to the Mat-In-Meca measurement protocol. The files contain approximatively 30 000 data points after filtering to characterize the section deformations.

The eventual cutting defects and the smoothing of the data allowed by the interpolation are evaluated to embellish the final treatment. Here are the different figures obtained from the treatment after filter application and after interpolation:

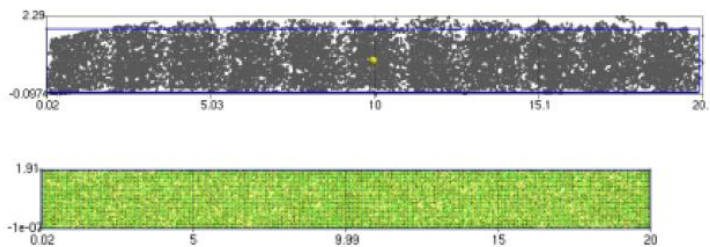


Starting from the left side to the right side:

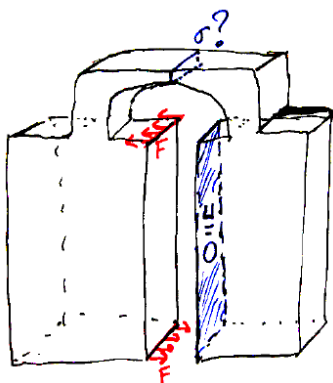
The first graph is the raw profile after the first filter for the “right” side. The second one is the raw profile after the first filter for the “left” side. These filters are applied for cleaning the point clouds and for noise reduction.

On the last one the points after the first filter are inverted and merged on the same graph and then interpolated by a python “bivariatespline” function.

The half-shape of the studied section has also been modelled with *Gmesh* to carry out the final simulation of the outline method. This data processing is combining 3D modelization of the half-shape, 4-node tetrahedron mesh, setting in data with imposed displacements, linear solver and finally post-treatment. The material parameters used are **E = 190 GPa**; **v = 0.3**. Here is the extraction of the modelled section with the associated mesh:



One particular thing to note, we tried to make contour on the secondary principal direction as described below:



The ring method had to be subjected on the very thin part on the upper sample area. Due to the important amount of plasticity induced by the cut, this contour direction has been abandoned.

Appendix 11 – Application of LXRDR measurements on LPB-F 316L Arches samples (CETIM)

Samples and device presentation:

Four different arches samples have been subjected to LXRDR measurements. These four samples have been manufactured by two different suppliers (Volum-e and Arcelor Mittal) into two different treatments (heat-treated and as-built). The aim was then to compare these four samples stress levels observed on a particular area. The stress level has been characterized in surface but also in depth illustrated by the blue line below, approximately 1 mm depth, basically localized in the center of the top side of the sample (see the X, Y and Z reference coordinates in the picture below):

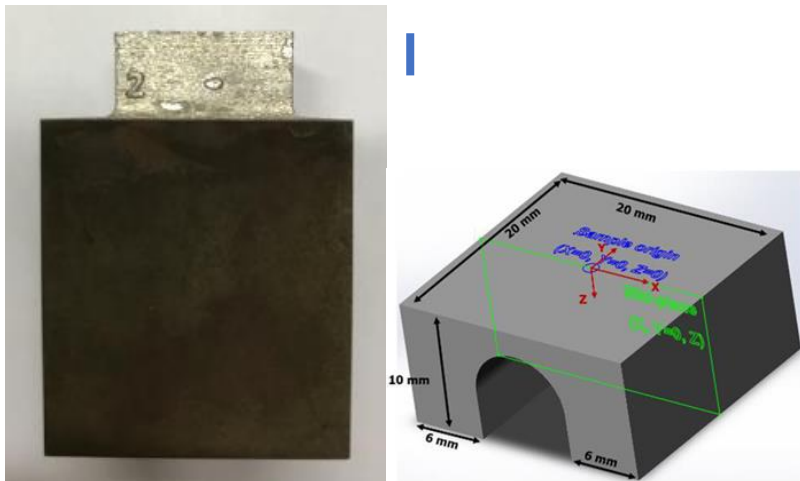
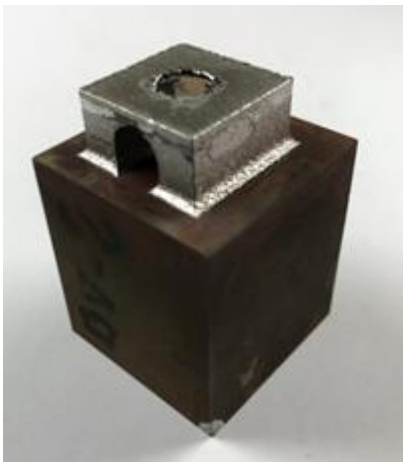


Figure 1 - Localization of the LXRDR measurements

As LXRDR is a surface measurement technique, the in-depth measurements needed the implementation of material removal. This has been done incrementally by electropolishing, using a LectroPol-5 device from Struers, through 20 – 50 – 100 – 150 – 200 – 250 – 300 – 400 – 500 – 600 – 700 – 800 – 900 and finally 1000 μm . Each depth was verified with a MITUTOYO profilometer and for each depth we analysed the complete 3-directions stress tensor.

We could finally obtain a stress profile focused on the first millimetre depth through a material removed circular area as illustrated below:



The analysis has been carried out following the EN 15305 (2009) standard: Test methods for residual stress analysis by X-ray diffraction. Here are the analysis parameters that we implemented in our device:

Table 1 - X-ray diffraction peak acquisition conditions

Device	X RAYBOT UR3
Detector	Linear
Set up	PSI
Radiance	K α of Manganese
K β filter	Chromium
Wavelength	2.1 Å
Counting time	90 s per ψ
Intensity / Voltage	25 kV / 1 mA
Theoretical peak position	152° in 2 θ
Collimator	2 mm
13 ψ angles	-37° to +39°
Oscillations	No
Using masks	Yes

If all the conditions are respected, which is the case right there, the results are given under COFRAC accreditation (COFRAC n°1-1014 available on www.cofrac.fr).

The facility we used (which design is presented at the end of the appendix) for the measurement was calibrated using a Copper powder reference sample coupled with an Inconel 690 reference.

The material parameters used for the stress calculation are **E = 193 GPa, ν = 0.3**.

Stress calculation process

By using the atomic planes as strain gauges, the residual stress calculations are then carried out from the StressDiff software by the $\sin^2\psi$ method with a centred barycentric peak localization method developed by the CETIM in biaxial computation.

The method used is the $\sin^2\psi$ method which consists in measuring the variation of the distance between the $d(\varphi, \psi)$ atomic planes of a single family (hkl) for several ψ incidences in a φ direction.

The φ angle defines the direction of measurement on the sample surface whereas the ψ angle defines the angle between the normal to the sample and the normal to the diffracting planes (Figure 1).

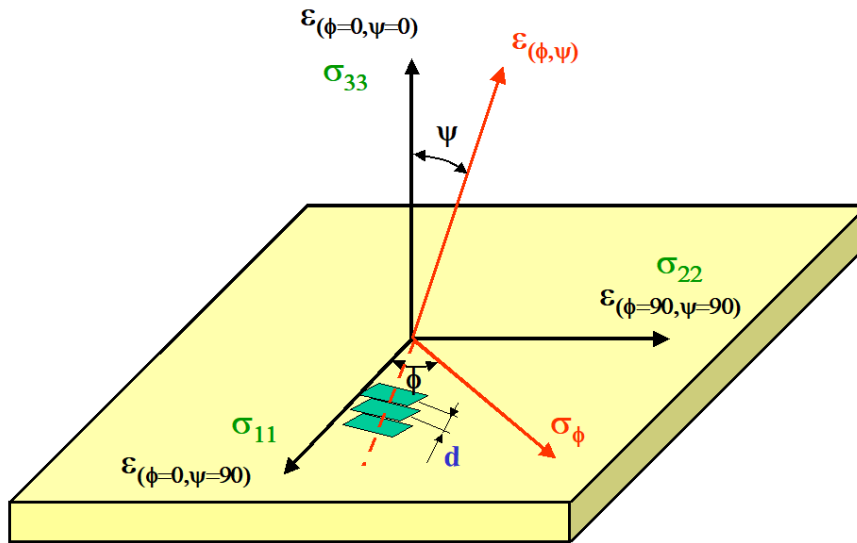


Figure 2 - Angular relations to determine the stress component in the ϕ direction.

The $\epsilon_{\phi\psi}$ strain in the ϕ direction, ψ is given by the relation

$$\epsilon_{\phi\psi} = \frac{d_{\phi, \psi} - d_{\perp}}{d_{\perp}} = \frac{\Delta d}{d} = \frac{1 + \nu}{E} \cdot \sin^2 \psi \cdot \sigma_{\phi} \quad (1)$$

where $d(\phi, \psi)$ is the distance between the atomic planes under a ψ incidence in the ϕ direction and d_{\perp} is the distance between the atomic planes of the same family for $\psi = 0$.

If we take the value of this strain $\frac{\Delta d}{d}$ as a function of the values of $\sin^2 \psi$, we generally obtain a linear relation whose slope $\frac{1}{2} S_2 \sigma_{\phi} = \frac{1 + \nu_{RX}}{E_{RX}} \cdot \sigma_{\phi}$ allows us, with the knowledge of the crystal elastic constant $\frac{1}{2} S_2$ of the material, to calculate the value of the stress σ_{ϕ} .

Sometimes, this relation (1) is not linear. As a matter of fact, for certain materials and in certain mechanical treatment or machining conditions (grinding, turning, etc.), two ellipse branches are observed for the values $\psi > 0$ and $\psi < 0$ which reflect the presence of a multiaxial stress state in the first surface layers and in particular the existence of σ_{23} and σ_{13} shear stresses.

We therefore obtain a relation of the type $\Delta d/d = A \sin^2 \psi + B \sin 2\psi$ characteristic of an ellipse, whose opening is proportional to the value of the shear stress.

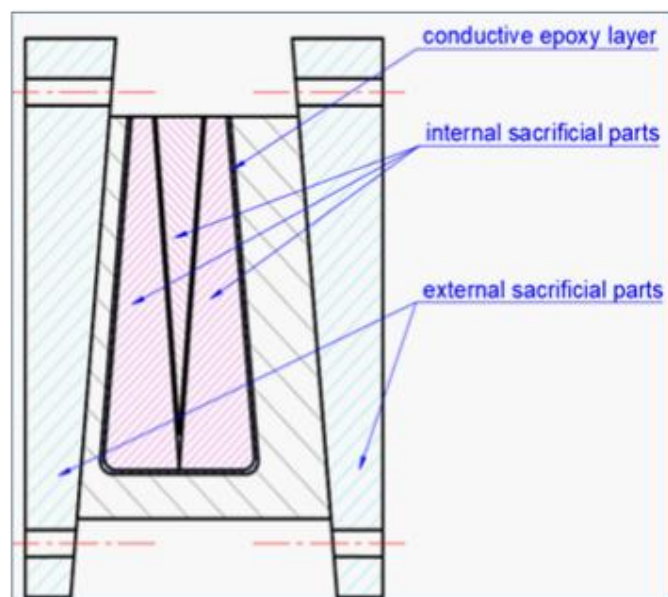


Figure 3 - Illustration of the device used for LXR measurement at CETIM.

Appendix 12 – Application of contour method to cast and quenched wedges and subsequent hole drilling

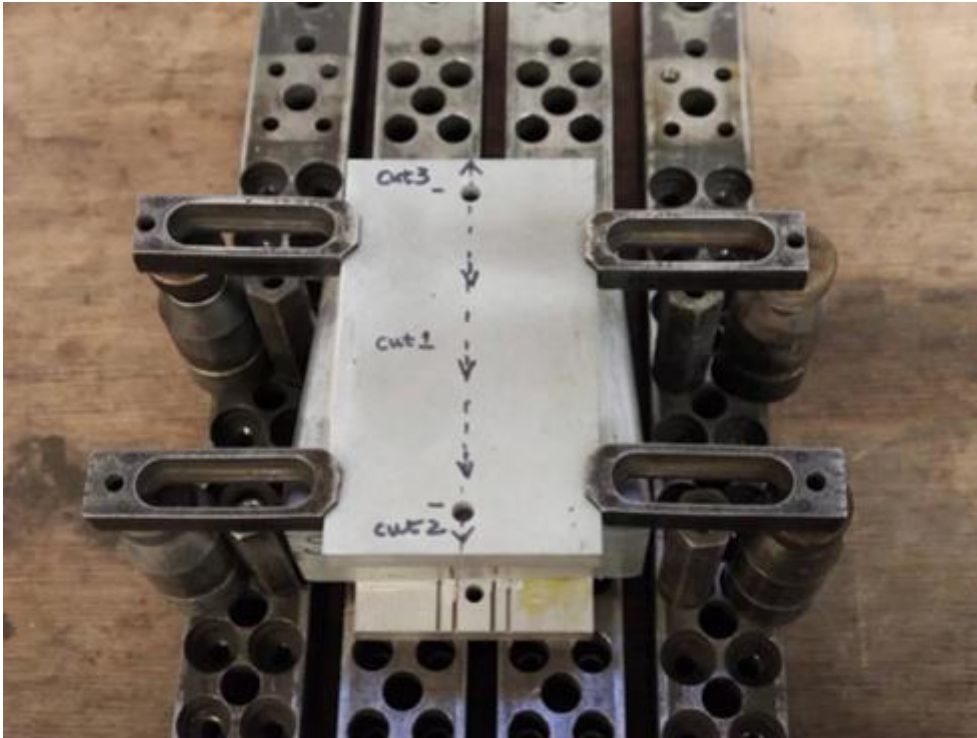
The wedges were prepared for cutting and measurement according to the following. The cross-sectional profile the target plane was first measured with a coordinate measurement machine, and sacrificial parts were then designed accordingly to fill up the inner cavity and render a rectangular outer geometry to avoid cutting artefacts. A set of pilot holes were arranged on outer sacrificial parts to minimize the relative movement of each side of the overall component during the cutting process. The assembled component prior to cutting is shown below.

The purpose of using conductive epoxy in the sacrificial material assembly is that it is practically impossible to achieve a perfectly mated surface between compensational parts and specimen. Therefore, conductive epoxy has to be applied to fill up the gaps and maintain an electrical connection between all components to be cut during the WEDM process. An ideal epoxy is that which has sufficient mechanical strength such that it can maintain restraint during cutting and conductivity which approaches that of the baseline material. Application of the epoxy should be minimal and sparing, with best results obtained when there is a near-perfect mate or a light interference fit between sacrificial and host material.

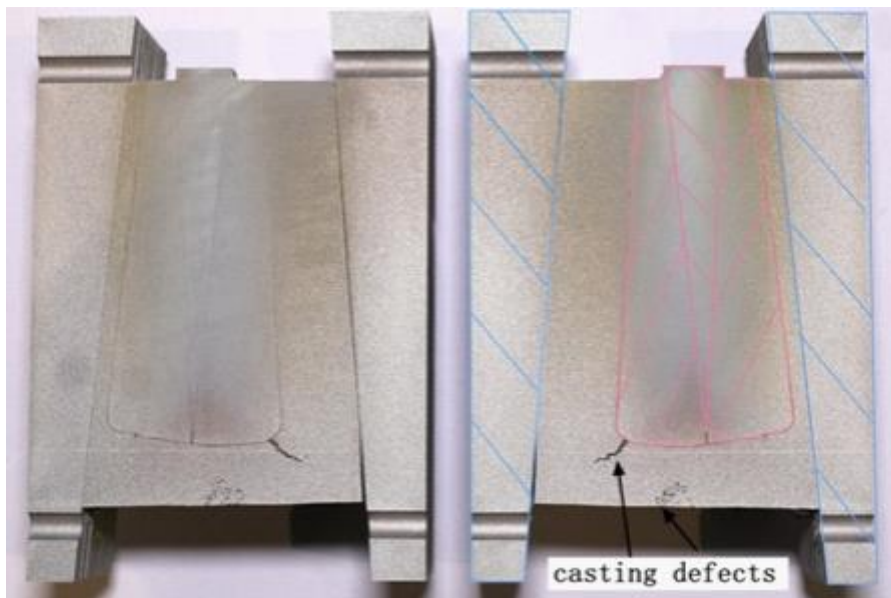


Contour cutting

Prepared specimens were cut with Wire Electro-Discharge Machining with a 250 μm diameter hard brass wire. An Agie-Charmilles FI440CCS CNC WEDM centre was employed. A modified 'E2' finish cut parameter for aluminium was used. Rigid clamping during cutting was applied at four corners of the outer sacrificial parts as shown below.



The region between two pilot holes was cut first, followed by another two cuts in the external sacrificial components to separate the specimen into two halves. The sacrificial parts were later disassembled with acetone and ultrasonic cleaning machine was used to accelerate the process. All cuts were completed without any wire breaks or rework required. A representative image of the cut surfaces obtained is shown below.



Contour method stress calculation

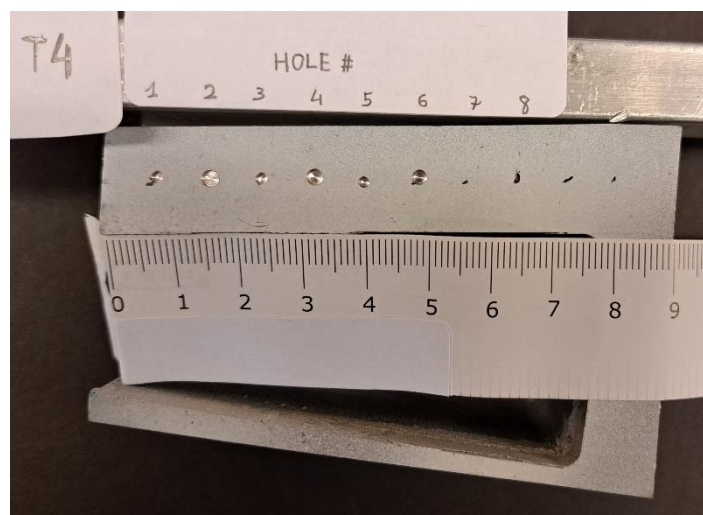
After the specimens had been cut, the displacement data normal to the cut plane (out of plane displacement) was measured with a Nanofocus μ Scan laser profilometer with a $30 \times 30 \mu\text{m}$ resolution across the plane of measurement, and $\pm 0.2 \mu\text{m}$ out of plane.

The measured data was processed with pyCM Ver 2.0, an open-source software for contour method data analysis. The point clouds of two halves of each specimen were processed in pairs, first by registering an outline. The registered datasets were then aligned and averaged to remove non-symmetrical errors and improve the resolution of the resolved surface. Surface data pertaining to pores and cracking were replaced with nearest neighbour values from both cut surfaces. A third order bivariate spline surface was fitted to the averaged point cloud to provide nodal boundary condition for subsequent FE analysis for stress calculation. To mitigate the effect of casting defects, most of the points at those regions were deleted as they introduced a significant disruption to the surface fitting process. A uniform knot spacing of 10 mm in both x and y directions was used to smooth out the missing data and alleviate artificial stress concentrations near the free surfaces of the wedge. It was found that this 10 mm value coincided with a balance between capturing a coherent distribution of stress, versus more highly localised fitting of data at the periphery of the cross-section.

After spline fitting, a uniform finite element analysis preprocessing step was undertaken for all samples. Approximately 600 nodes were applied equally along the outline of spline surface, and then a 3D mesh was extruded 50 mm from the 2D profile with a geometric distribution of elements along the extrusion direction, this generated approximately 60,000 C3D8 elements for each analysis. This 50 mm dimension matches the internal void length of the component such that the mesh replicates the actual component geometry. Elastic material properties imposed throughout the FE calculation were a modulus of elasticity of 74.7 GPa and Poisson's ratio of 0.33 as dictated by the supplier.

Subsequent hole drilling measurements by ESPI

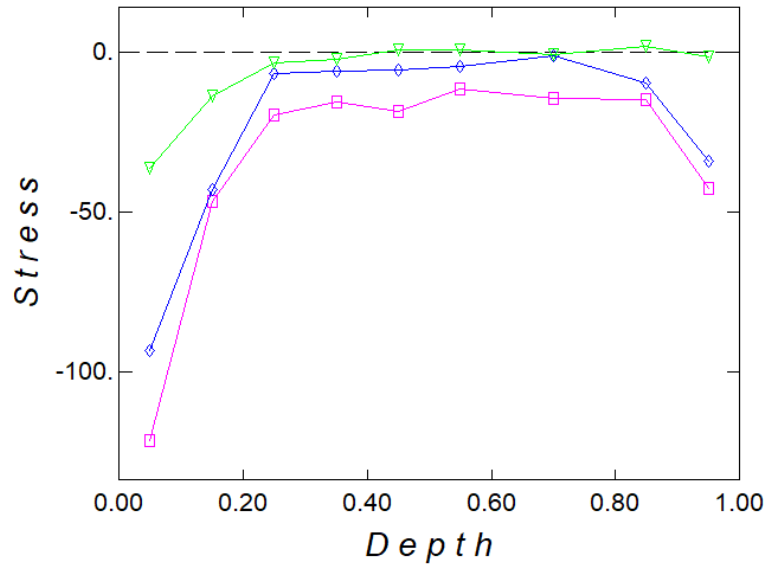
Samples from each temper were obtained corresponding to the 'right' hand side of the wedge after contour cutting. The WEDM surface was then lightly decorated in order to improve optical interference patterns, with a total of 6 holes drilled and measured at 100 μm intervals, as shown below for the T4 temper. Note that the results obtained were reported with 'x' aligned along the line of holes, and 'y' aligned orthogonal to this.



Two interferometers were employed, with odd numbered holes given to a custom in-plane interferometer, and the even numbered holes for a commercial in-plane system (Prism).

All holes for all tempers identified near equi-biaxial stresses, -30 to -100 MPa near the surface, reducing to small values in the interior. A typical result for hole 6 in the T4 sample is shown below, with pink and blue lines showing normal components, and green the shear component. The interior

stresses were deemed close to the measurement threshold of the technique, with the results also consistent across interferometers. The elevated compressive stresses found for all holes is due to the presence of the EDM recast layer, which is why for superposition values at a depth of 300 μm was employed for combining with contour method results.



All results were obtained in tabular form, and were manipulated such that the measurement coordinate system was aligned to that of the contour method coordinate system prior to combining results. This was achieved by scanning each drilled component to obtain outlines of both holes and periphery of component, and applying the necessary transformations of both coordinates and stress tensors to render the results in the appropriate orientation for comparison to other techniques.

Appendix 13 – Application of neutron diffraction to the cast, quenched and T6 tempered aluminium wedge

The wedge samples were measured with the time-of-flight thermal neutron diffractometer called POLDI (Pulse OverLap Diffractometer) at the Swiss Spallation Neutron Source which is part of the Paul Scherrer Institute in Switzerland. This instrument is specifically dedicated to spatially resolved measurements of residual stresses in engineering components. Since the neutron diffraction method for residual stress determination is in principle non-destructive, the wedges could be directly mounted onto the sample stage without prior sample preparation. Figure 1 (a) shows the sample stage with an additional support system where the wedge samples were mounted. The sample is located at the intersection of the primary (source) and the secondary beam (detector) path which are oriented in a 90° angle to each other. The sample table is mounted on a rotation table which allows to drive the sample $\pm 180^\circ$ with a resolution of 0.002° . The sample was aligned using a camera system. The schematics in Figure 1 b)-d) show the sample orientation for the three different measurement directions which had all the same gauge volume of $3.8 \times 3.8 \times 3.8$ mm. The measurement of the normal and transversal direction was done with the sample being mounted in the same position on the table but with a change in the ω -rotation from 45° to -45° . For measuring the longitudinal direction, the sample had to be removed from the table, flipped 90° , and repositioned. Swarf or discontinuous/segmental chips were employed as a stress-free reference, and was measured in a Vanadium container. The data collected on POLDI comes as a 2D time-angle spectra which is stored in an HDF-format. This data needs to be first reduced before it can be analysed with standard powder diffraction programs. This was done with a program called Mantid in which a Pawley-fitting routine was used to fit multiple peaks in the diffractograms of each measurement point in order to obtain the lattice parameters. The residual strain and stress values were then calculated using an in-house written script in Mathcad following the equations highlighted in the EASI-STRESS deliverable 4.2.

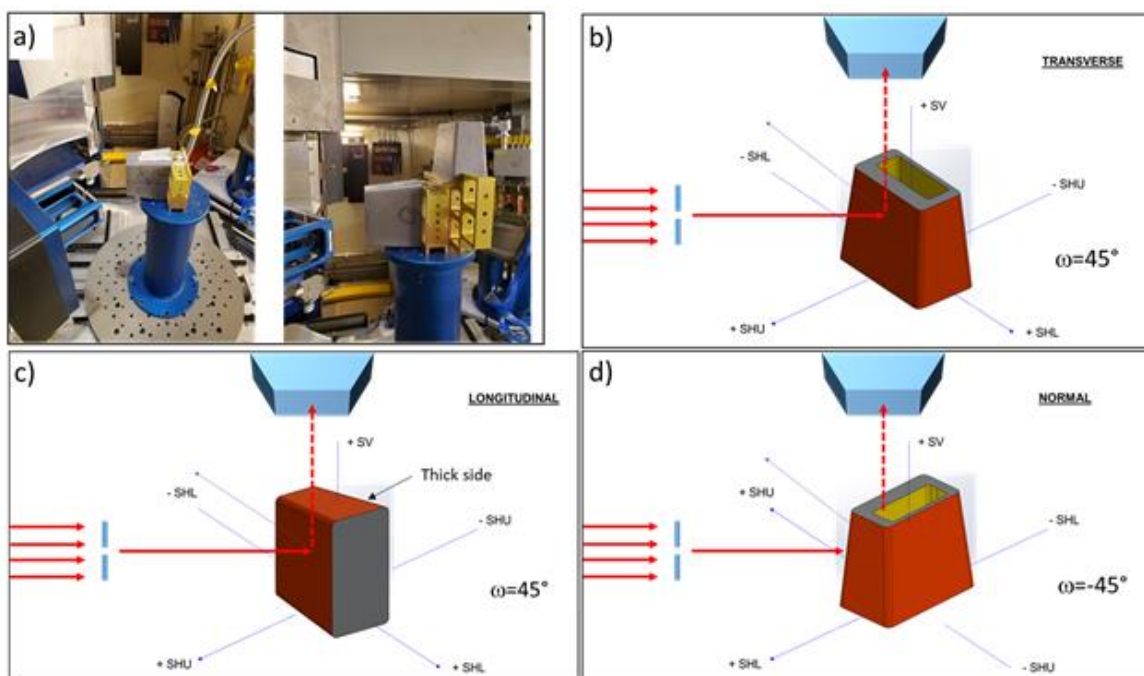


Figure 1 - a) Standard sample table (blue) with special support system (yellow) positioning the wedge samples between the incoming beam path and the detector. Schematic of the sample positioning for the measurement of the b) transverse, c) longitudinal, and d) normal direction.

Appendix 14 – Application of hole drilling measurements with strain gauges to cast and quenched wedges, L-PBF 316L Arches samples and ferritic U-bend shapes

The hole drilling method is one of the stress relief methods. These methods consist in analysing the stress relief which occur in a metal part when metal removal is carried out on that part. The measurement of the distortions generated by such stress relief makes it possible, through analysis of the successive equilibrium states, to go back to the values of the residual stresses that existed in the part before material removal. The hole drilling method has been used for a long time to measure residual stresses. But until the last few years, the experimental procedure used and the theoretical formulation of the method only allowed it to be used in the case of homogenous residual stresses in the material thickness.

The recent developments made it possible to improve this method so that it can be used to determine, from step by step drilling, the distribution of the residual stresses in the material thickness whether a stress gradient is present or not.

The principle of the hole drilling method is simple: it consists in drilling a hole in the middle of a three-direction strain gauge rosette, the centre of the hole being located at the place whose residual stresses must be analysed (Figure 1). The removal of material from the studied part (and, therefore, the removal of residual stresses) generates a new mechanical equilibrium which is expressed by equations derived from the laws of elasticity relating the residual stresses present at the place of drilling to the distortions measured in the strain gauge rosette.

In the case of the traditional method, drilling is carried out with a drill bit down to a depth of approximately 1.5 times the diameter of the hole. After drilling, distortions are obtained in the three strain gauges. These distortions make it possible to calculate, over the drilled material thickness, an average value for the two main stresses σ_1 and σ_2 and the angles of their directions with respect to the reference index.

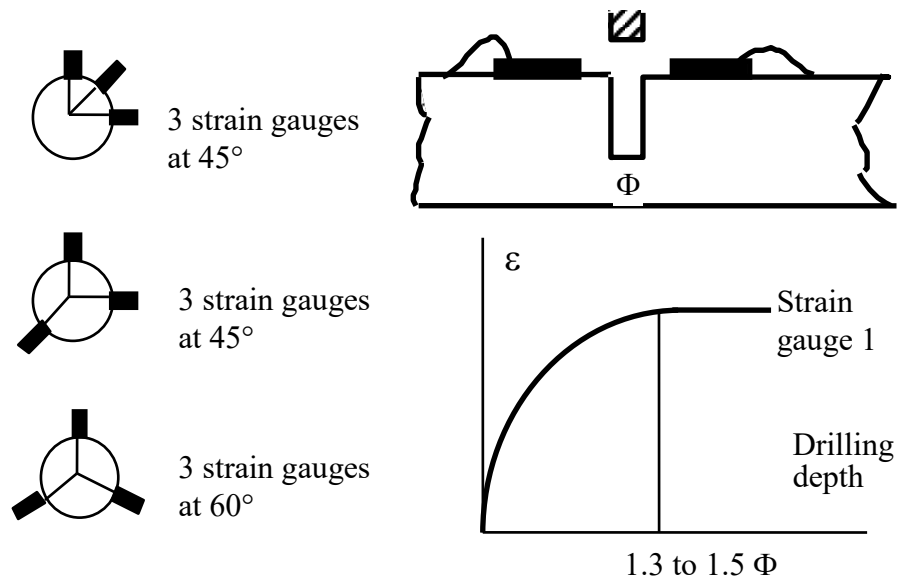


Figure 1 - Principle of the traditional hole drilling method with different types of strain gauges

In the case of the incremental hole drilling method, a flat-bottomed hole is drilled, and drilling is performed step by step. During the drilling operation, at increasing Z depth, the distortion values in the strain gauges are recorded. When drilling is complete, it is possible to calculate the main stresses σ_1 (Z) and σ_2 (Z) and also

the angle $\theta(Z)$ formed by the direction $\sigma_1(Z)$ with respect to a reference direction. The calculation is performed from the distortions $\varepsilon_l(Z)$ measured at each depth increment and from influence coefficients.

$$\sigma_{1hn} = \frac{\varepsilon_n^1(A_{nn} + B_{nn} \sin 2\theta_n) - \varepsilon_n^2(A_{nn} - B_{nn} \cos 2\theta_n)}{2A_{nn}B_{nn}(\sin 2\theta_n + \cos 2\theta_n)}$$

$$\sigma_{2hn} = \frac{\varepsilon_n^2(A_{nn} + B_{nn} \cos 2\theta_n) - \varepsilon_n^1(A_{nn} - B_{nn} \sin 2\theta_n)}{2A_{nn}B_{nn}(\sin 2\theta_n + \cos 2\theta_n)}$$

$$\theta_n = \frac{1}{2} \tan^{-1} \left[\frac{\varepsilon_n^3 - \varepsilon_n^2}{2\varepsilon_n^1 - \varepsilon_n^2 - \varepsilon_n^3} \right]$$

In these relations, ε_{n1} , ε_{n2} and ε_{n3} are the distortions corresponding to the stresses which exist in the same increment before drilling the n th increment; and A_{nn} and B_{nn} are influence coefficients which relate the stresses present at the depth h_n and the distortions measured during the drilling of the n th increment. These coefficients are calculated by finite elements by means of a program derived from the CASTOR structure computation code developed by CETIM. These coefficients are function only of the geometry of the strain gauge rosette, the geometry of the hole, the geometry of the part and the elastic stresses of the material (E , ν).

3 Aluminium samples have been analysed in CETIM by incremental hole drilling (as-cast, T4 and T6), using both $\varnothing 3.5$ mm gauges and solid 2 flutes carbide end mill with cylindrical shank. The deformations were measured using TML strain gauge rosettes (part No. FRS 3-11 F) connected to an MGC+ data acquisition unit.

The hole drilling has been done approximatively centred in the thicker part of the defined area and perpendicular to the surface, through the option A in the picture below.



Figure 2 - Localisation of the drilled area

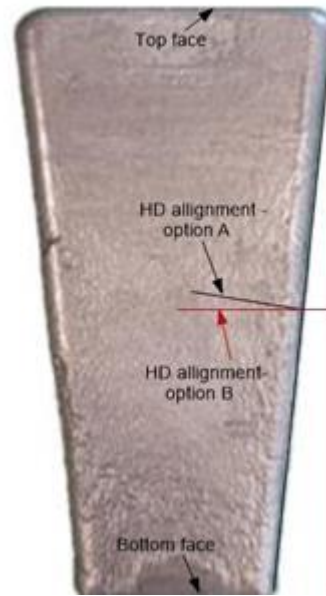


Figure 3 - Illustration of the HD direction



Figure 4 - Localisation of the drilled area on U-bend and on Arches

For the ferritic U-bend shapes and the L-PBF 316L Arches samples, we used $\varnothing 2$ mm gauges instead of the $\varnothing 3.5$ mm ones. Those ones were measured using TML strain gauge rosettes (part No. FRS 2-11 F) connected to an MGC+ data acquisition unit.

The elastic constants we used for each material are given in the table below:

Reference sample	Poisson's ratio	Modulus of elasticity
L-PBF 316L Arches	0.3	193 GPa
U-bend ferritic shape	0.3	210 GPa
Aluminium Wedges	0.3	70 GPa